Volume: 5 Issue: 1 2024

Eurasian Journal of Science Engineering & Technology

Eurasian Journal of Science Engineering and Technology

Editors

Editorial Board

Eurasian Journal of Science Engineering and Technology

Scientific Board

Eurasian Journal of Science Engineering and Technology

Correspondence Address

Niğde Ömer Halisdemir University
Eurasian Journal of Science Engineering and Technology Publishing Coordinatorship, 51240
Niğde/Türkiye

***E-mail*:** recep.zan@ohu.edu.tr
mbarut@ohu.edu.tr

***Web page*:** https://dergipark.org.tr/tr/pub/ejset

Publication information

The objective of Eurasian Journal of Science Engineering and Technology (EJSET) is to provide an academic environment for researchers in various fields of science and engineering and for the publication and dissemination of high-quality research results in the fields of science, applied science, engineering, architecture, agricultural science and technology.

Eurasian Journal of Science Engineering and Technology

CONTENTS/*İÇİNDEKİLER*

Eurasian Journal of Science Engineering and Technology

Research Article

THE INFLUENCE OF THE CARBURIZING PROCESS ON THE IMPACT-SLIDING WEAR BEHAVIOR OF 14NiCr14 STEEL

Ömer Faruk ÇOŞKUN [1], Ayşenur EĞERCİOĞLU [2], Gökhan ÖZDEMİR [3], Harun MİNDİVAN [4,*],

[1,2,4] *Bilecik Şeyh Edebali University, Faculty of Engineering, Department of Mechanical Engineering, 11230, Bilecik, Türkiye*
[3] *Bilecik Şeyh Edebali University, Vocational School, Hybrid and Electric Vehicles Technology, 11230, Bilecik, Türkiye*
[1] *Ata Silah San. A.Ş., İstanbul, Türkiye*

ABSTRACT

Weapons depend largely on the barrel. Gunpowder combustion converts chemical energy into thermal and mechanical energy. Barrels give projectiles initial speed and flight direction, and helical grooves require fast spinning for stability while moving toward the target. Due of barrel exposure to heat, high pressures, gunpowder vapors, and external impacts, this weapon element needs extensive investigation. The study discusses carburizing for surface modification in high-pressure circumstances to improve gun barrel interior line tribology. Carburizing has been detected at a depth of 960 μm from the surface, as revealed by light-optical microscope images. The microhardness test has been performed on the sample's cross section, which has a maximal hardness of 650 ± 10 $HV_{0.05}$ close to the surface and 250 ± 5 $HV_{0.05}$ close to the interface. At room temperature (RT), this study looked at how the carburizing process affects the impact-sliding wear performance of 14NiCr14 steel, which is widely used in the barrel extensions of guns under complex loading conditions. A series of impact-sliding wear experiments were conducted on 10 mm-diameter bearing steel balls made of 52100-grade steel, for a total of 4297 loading cycles. A 2-D contact profilometer and a light optical microscope (LOM) then examined the wear tracks that had formed on the samples. The carburized steel caused a decrease in the wear rate at the impact and sliding zones of the wear track.

Keywords: Barrel extension, Depth of diffusion layer, Surface damage, Surface hardening, Steel.

1. INTRODUCTION

Gun barrels, breech mechanisms, and other sliding mechanisms experience severe wear during shooting and operations. The primary cause of barrel failure is the bore's expansion due to wear. As a result of wear damage, the tactical and technical characteristics of the weapon system, such as shot accuracy, firing range, and muzzle velocity, are diminished, thereby shortening the weapon's lifespan [1]. Some techniques for increasing material wear resistance are supported, such as using wear-resistant materials at the expense of product price, using surface technology, or using lubricants. However, in intense battle conditions, weapons' lubricating ability is restricted. Then, to increase the tribological properties of barrel material, surface technology is mentioned [2]. Barényi and Šandora [3] discuss recent trends in improving the mechanical properties of steels used for sport or army gun barrels, focusing on special conditions like high tensile strength, surface hardness, yield point, and impact value. It also discusses howitzer or cannon barrel production, heat treatment, and the electroslug remelting process for barrel quality improvement.

Since World War II, diffusion surface hardening (DSH) processes have been used to preserve barrels, but there has been renewed, active research in this area over the past decade [4]. The DSH has a hard surface on the outside and a soft, tough core. The enhancement in surface hardness directly contributes to the enhancement of wear resistance, hence leading to an improvement in the longevity of the component. Gas carburizing is a popular surface hardening method with low thermal distortion to enrich the surface layers of steel or other alloys with carbon [5, 6]. According to Arulbrittoraj et al. [7], gas-carburizing surface hardening significantly improves wear resistance at moderate temperatures with a small effect on visibility, indicating its potential for light-duty applications. Recent research has focused primarily on understanding the mechanisms of wear failure and evaluating the performance of known potential carburized steel, as opposed to the development of new coating materials. The ball-on-disc test, the impact test, the fretting wear test, and the abrasive wear test are all well-known ways to study surface failures on different substrates [1, 4, 8]. Li et al. [9] proposed a computational model for surface damage in artillery barrel chambers caused by thermochemical erosion and mechanical wear. It includes three sub-models: collision wear, melting exfoliation, and high-speed jet wear. The model predicts mechanical structures' surface damage based on contact force, temperature distribution, and the effect of melting exfoliation and collision wear on high-speed jet attack angles. But there is no

* Corresponding author, e-mail: harun.mindivan@bilecik.edu.tr (H. Mindivan)
Recieved: 18.10.2023 Accepted: 24.05.2024
doi: 10.55696/ejset.1375016

good way to test the wear properties of carburized steel when it is subjected to a combination of impact and sliding movements at very high contact stress. Still, there needs to be a way to test the wear caused by repeated impact-sliding movements.

The utilization of carburized 14NiCr14 steel, characterized by a high level of toughness in its core, is deemed appropriate for components subjected to dynamic loading conditions [10]. Industrial materials having high resistance to impact-sliding wear have been studied increasingly. The objective of this study was to find out how long carburized 14NiCr14 steel would last under complex wear conditions. This was done by using an impact-sliding wear tester and increasing the contact loads up to 240 N in one loading cycle. For the barrel extensions of guns made of 14NiCr14 steel, it would be useful to know how well carburized 14NiCr14 steel works under dynamic loading conditions.

2. MATERIAL AND METHOD

20 mm in diameter and 10 mm in height disc samples were cut from commercially available 14NiCr14 steel. The discs were gas-carburized at 900 °C for 5 h, quenched, and then tempered at 300 °C for 1 h. The microstructure of the carburized 14NiCr14 steel was observed with a Nikon Eclipse LV150 Light Optic Microscope (LOM). The hardness measurements were performed on the cross-sections of the untreated and carburized 14NiCr14 steels with a Vickers pyramid indenter using a conventional microhardness tester (Shimadzu HVM) with a load of 50 g and a dwell time of 15 s per the ASTM E384-11 guidelines.

Researchers at Bilecik Seyh Edebali University designed a home-made impact sliding tester, shown in Fig. 1, to evaluate the impact-sliding wear performance of untreated and carburized 14NiCr14 steels. The design of the tester was patented by Chen and Nie [11]. During the experimental procedure, the application of loads onto the surfaces of both untreated and carburized 14NiCr14 steels was regulated by the utilization of a spring and a pneumatic cylinder. Prior to testing, a load cell set the maximum loads that the spring and pneumatic cylinder could provide at 40 N and 240 N, respectively. At ambient temperature (20±5 °C and 40±5% RH), impact-sliding wear tests of untreated and carburized 14NiCr14 steels were conducted against commercially available 10 mm SAE 52100 grade bearing steel balls. Two distinct regions of wear scar (impact and sliding) were examined by a 2-D surface profilometer following the impact-sliding wear test in order to calculate the quantity of wear loss. The wear rates were then calculated by dividing the volumetric wear loss by the number of loading cycles in mm^3/cycle. To ascertain the wear mechanism, LOM examinations were also performed on the worn surfaces of untreated and carburized 14NiCr14 steels. To better understand the wear mechanism in the impact-sliding tests, it was necessary to evaluate the friction coefficient of the sample-counterface system under a sliding motion. In this case, reciprocal sliding tests were carried out under an ambient condition (20±5 °C and 40±5% RH) according to the ASTM G133-05 standard using a 10 mm SAE 52100 steel ball, a sliding speed of 1.9 cm s^{-1}, a sliding distance of 60 m, a track length of 11.5 mm, and a normal load of 30 N.

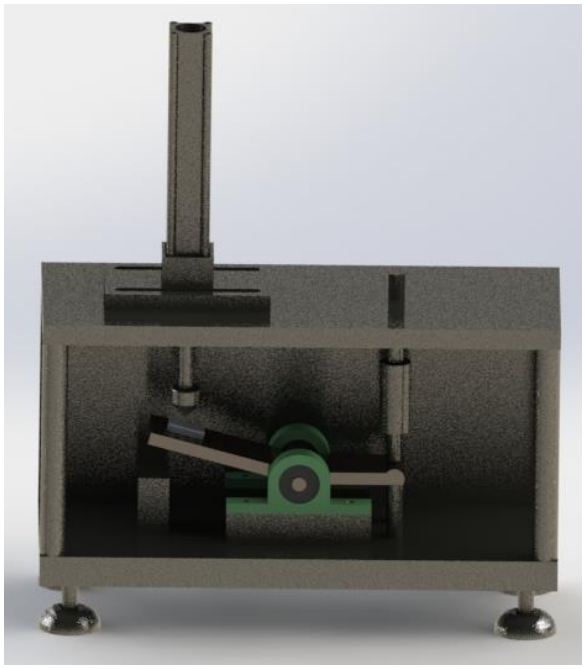

Figure 1. Schematic view of impact-sliding wear tester.

3. RESULTS AND DISCUSSION

Figure 2 exhibits the LOM microstructures of a cross-sectioned gas-carburized sample for different magnifications. After the gas carburization process, tempered martensite and sorbite primarily composed the structure of the steel (Fig. 2). The presence of eutectoid and under-eutectoid compositions in the carburized layer of 14NiCr14 steel is evident.

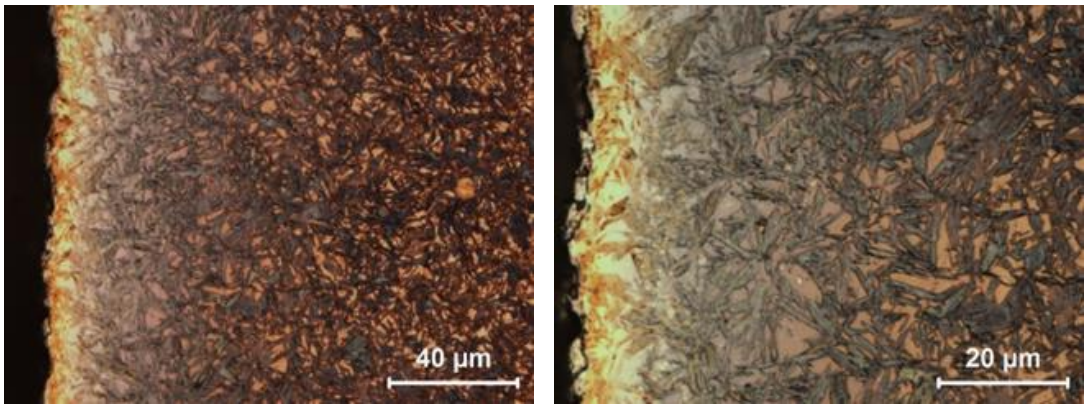

Figure 2. Cross-section LOM microstructures of the carburized 14NiCr14 steel (low and high magnifications).

The hardness values of untreated and carburized 14NiCr14 steels are plotted from the surface to the core in Figure 3. These values are shown in ascending order. The surface of the untreated 14NiCr14 steel has an average hardness of 250 ± 5 $HV_{0.05}$. The carburized 14NiCr14 steel has a maximum surface hardness value of 650 ± 10 $HV_{0.05}$. The carburizing process resulted in a hardness profile that gradually decreased. This drop in hardness demonstrates that the diffusivity of carbon is higher on the surface and gradually decreases toward the core. The surface has a higher concentration of carbon than the core does. Because the value of hardness stays the same after 960 µm have been removed from the surface of carburized steel, this demonstrates that the maximum depth at which carbon diffusion takes place is 960 µm.

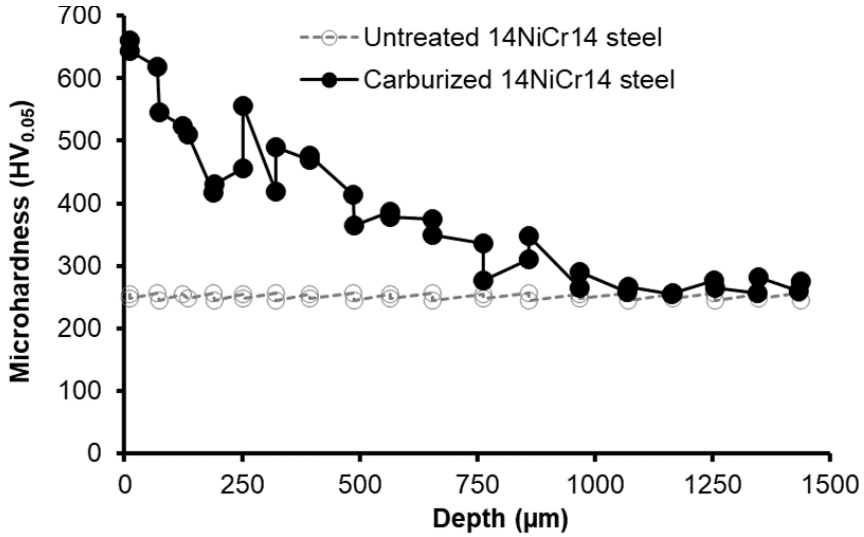

Figure 3. Microhardness values of gas-carburized 14NiCr14 steel from the surface to the core.

Figure 4a illustrates the schematic representation of a wear track, whereas Figs. 4b and c illustrate the 2-D profiles of the impact and sliding zones of the wear tracks for both untreated and carburized 14NiCr14 steels following impact-sliding wear tests. For untreated 14NiCr14 steel, the impact zone has greater depth and width than the sliding zone. However, the gas carburization process imposed shallower and narrower wear tracks in both impact and sliding zones. In the case of carburized 14NiCr14 steel, the depth of the wear track formed by the steel ball in both impact and sliding zones is less than the depth of the carburized layer (960 µm). High-case depth and surface hardness steels are more wear-resistant [12]. The relatively soft,

untreated 14NiCr14 steel was more likely to yield under high cyclic loading conditions. The system's pile-up zones [13] indicated material transfer rather than wear loss. Additionally, pile-up formations were observed in the edges of the impact and sliding zones, indicating that plastic deformation played a role in the progression of wear for untreated 14NiCr14 steel, whereas the carburized layer had a much higher hardness and provided better load support; thus, very limited damage could be observed on carburized 14NiCr14 steel, and pile-up zones were not obvious after the test.

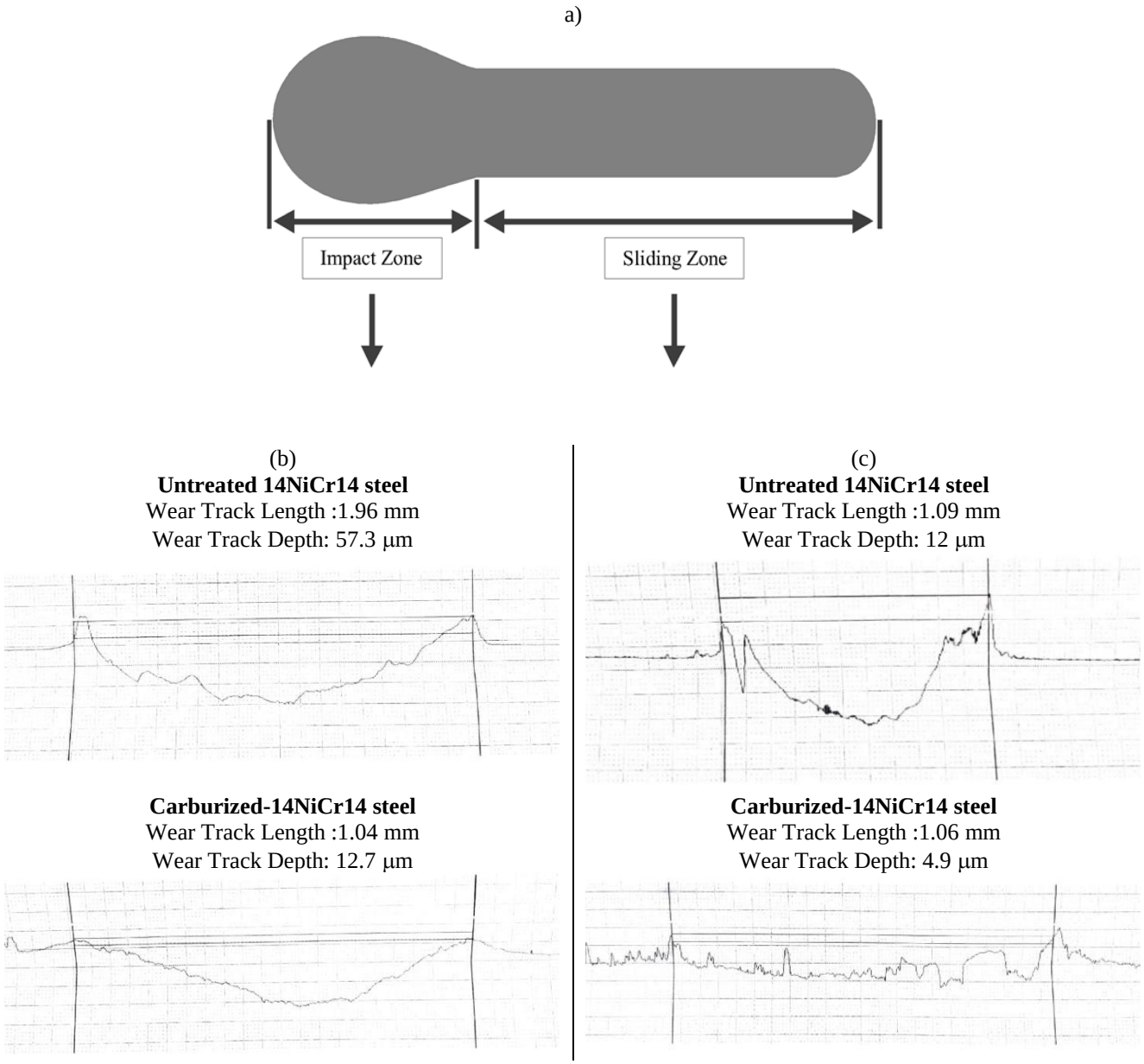

Figure 4. (a) A schematic drawing of the wear track that was made on the samples' surfaces. After impact-sliding wear tests, 2-D profiles of the untreated and carburized 14NiCr14 steels' impact (b) and sliding (c) zones.

Figure 5 depicts the wear rates of the samples' impact and sliding zones. It should be noted that gas carburization reduced the wear rate of the impact zone by 87%, while only 37% of the wear rate of the sliding zone was reduced. Gas carburization, on the other hand, reduced the total wear rate by 81%.

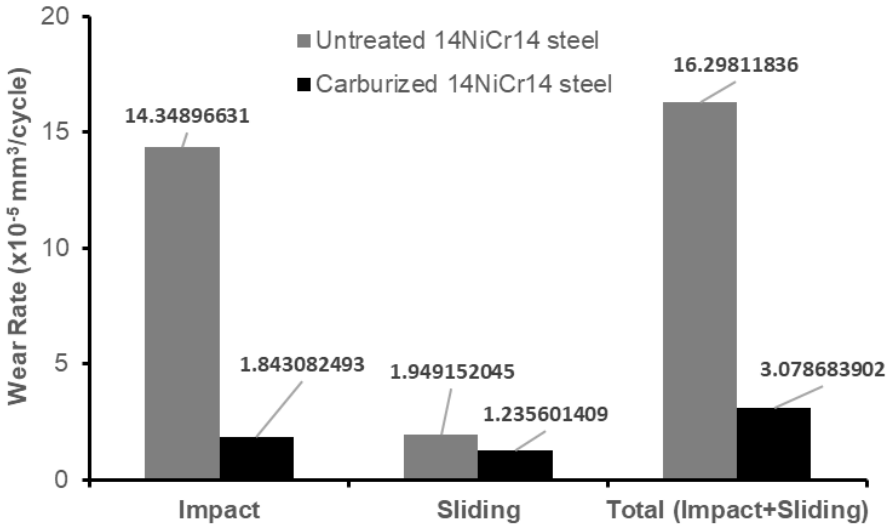

Figure 5. Wear rates of the wear tracks formed on the surfaces of the untreated and carburized 14NiCr14 steels.

The coefficient of friction (CoF) plot under reciprocal sliding tests is shown in Fig. 6. The initial phase, referred to as the running-in stage, exhibited a notable rise in CoF, whereas the subsequent phase, referred to as the steady-state stage, demonstrated a plateau after varying sliding distances of the two steels. The plateau values of untreated and carburized 14NiCr14 steels were approximately 0.63 and 0.96, respectively. The results of Fig. 6 show an increase in the CoF of the carburized 14NiCr14 steel as reported by Dobrocky et al. [14].

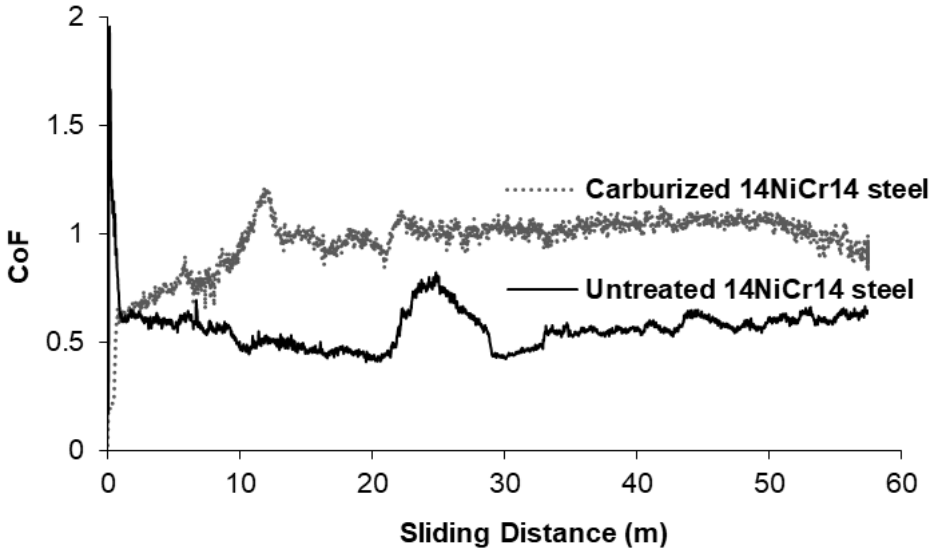

Figure 6. Trend of the CoF under reciprocal sliding tests.

LOM images of the wear tracks formed during the tests are shown in Figs. 7 and 8. The worn surfaces of the untreated 14NiCr14 steel showed severe plastic deformation, with pile-up zones at the edges of the impact and sliding zones (Fig. 2), which were larger in the impact zone than in the sliding zone. High contact pressure causes extreme wear and deep plowing and scratching of the worn surface, resulting in direct metal-to-metal contact [15]. The sliding zone of the untreated 14NiCr14 steel displayed microscale cutting and plowing processes, which were caused by abrasive wear (Figs. 7 and 8). A decrease in the CoF for untreated 14NiCr14 steel will result in an increase in the sliding amplitude, hence causing a greater extent of abrasion wear during the reciprocal sliding test. This observation aligns with the findings depicted in Fig. 6. As carburized 14NiCr14 steel was composed of a hard surface layer on a relatively soft matrix, plastic deformation occurring in the 14NiCr14 steel with high toughness in the core under an impact load could induce surface layer brittle fracture. However, the carburized layer did not detach (Figs. 7 and 8), and the rubbing of the steel ball in the sliding zone caused a combination of adhesive and oxidative

damage to the carburized 14NiCr14 steel (Figs. 7 and 8). The production of the hard layer, which consisted of the carburized layer and the carbon diffusion zone beneath it, as a result of gas carburization had a significant hardening impact, as was anticipated by this formation. The carburized layer exhibited hardness values of 650 ± 10 $HV_{0.05}$, whereas untreated 14NiCr14 steel exhibited softer hardness values of 250 ± 5 $HV_{0.05}$. During impact-sliding wear tests, it was observed that the steel balls also experienced wear, as depicted in Figs. 7 and 8. The wear scars observed on the contact surfaces of balls have a direct relationship with the size of the wear tracks observed on both untreated and carburized 14NiCr14 steels. This correlation suggests that the wear of the ball is influenced by the dimensions of the contact regions. It is important to acknowledge that the quantity of wear debris that adheres to the surface of the steel ball in contact with untreated 14NiCr14 steel is significantly higher compared to the surface of the steel ball in contact with carburized 14NiCr14 steel during impact-sliding wear tests.

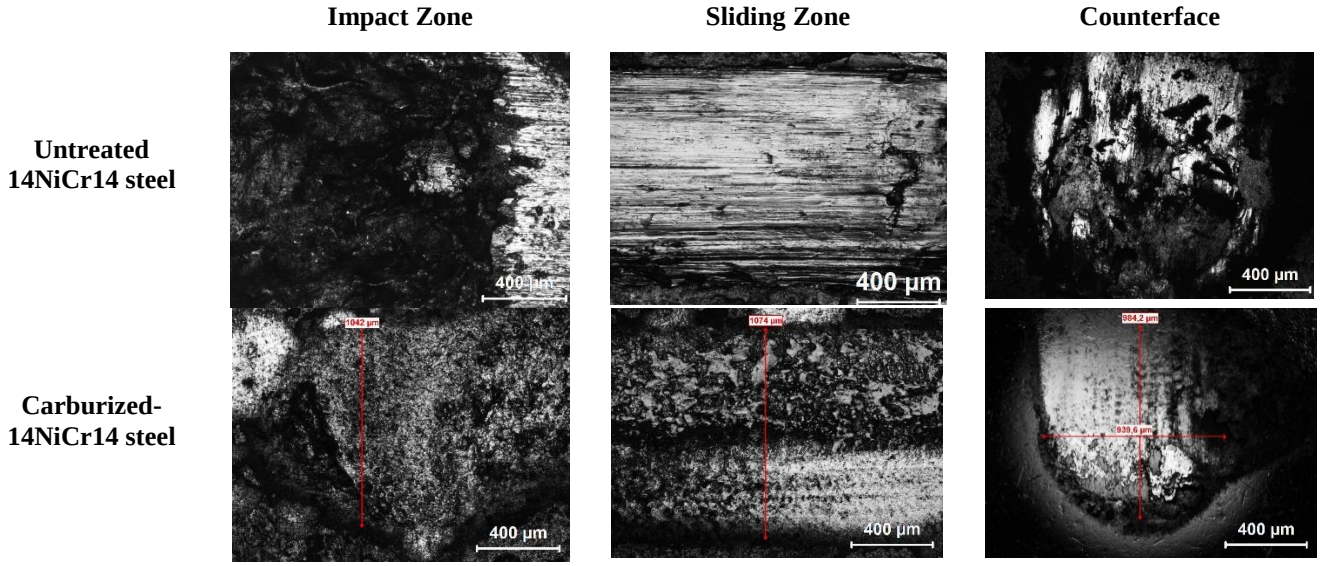

Figure 7. Low magnification LOM images showing the morphology of the wear tracks.

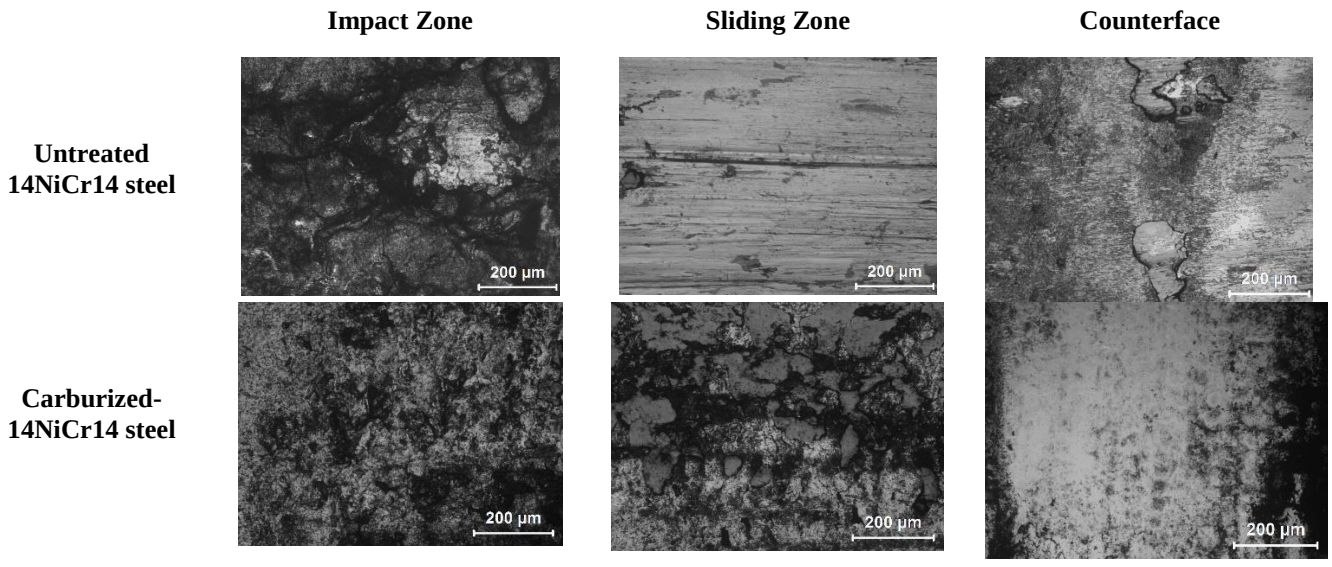

Figure 8. High magnification LOM images showing the morphology of the wear tracks.

4. CONCLUSION

The fatigue wear behavior of untreated and carburized 14NiCr14 steels was assessed under high contact stresses in an atmospheric setting using an inclined cyclic impact-sliding test, yielding successful results. The following is a concise summary of the present study's findings:

1. The plastic deformation was the main cause of the wear loss of untreated 14NiCr14 steel in the impact motion of the experiment. During the sliding motion of the experiment, abrasive wear and adhesive/oxidative damage were the main causes of wear loss in both untreated and carburized 14NiCr14 steels, respectively.
2. In the impact and sliding zones, carburized 14NiCr14 steel had an 87% and 37% reduced wear rate, respectively, compared to untreated steel under 40/240 N contact load conditions.
3. Carburized 14NiCr14 steel exhibited a decreased total wear rate, defined as the sum of the wear rates of the impact and sliding zones, indicating that it may be a viable candidate for gun barrel extensions.

SIMILARITY RATE: 15 %

AUTHOR CONTRIBUTION

Harun Mindivan: Conceptualization, methodology, writing, editing etc.
Ayşenur Eğercioğlu: Conceptualization, methodology.
Gökhan Özdemir: Methodology.
Ömer Faruk Çoşkun: Conceptualization, methodology.

All authors have read and agreed to the published version of the manuscript.

CONFLICT of INTEREST

The authors declared that they have no known conflict of interest.

ACKNOWLEDGEMENT

The financial support of the research foundation of Bilecik Seyh Edebali University (Project No.: 2023-01.BŞEÜ.03-01) is gratefully acknowledged. We would like to acknowledge Unal Colak for his technical assistance.

REFERENCES

[1] M. Polášek, M. Krbaťa, M. Eckert, P. Mikuš, R. Cíger, "Contact Fatigue Resistance of Gun Barrel Steels", *Procedia Structural Integrity*, vol. 43, pp. 306-311, 2023.
[2] A.Y. Albagachiev, M. E. Stavroskii, M. I. Sidorov, "Tribological Wear-Preventive Coatings", *Journal of Machinery Manufacture and Reliability*, vol. 49, no. 1 Mar., pp. 57-63, 2020.
[3] I. Barényi, J. Šandora, "Trends in Mechanical Properties Enhancing of Steels Used for Gun Barrels Production", *University Review*, vol. 8, no. 3-4, pp. 23-28, 2014.
[4] M. Jakopčić, D. Landek, "Abrasion Resistance of Surface-Modified Steels Used For Artillery Weapon Barrels", *Transactions of Famena Xli-1*, vol. 41, no. 1, Apr., pp. 15-20, 2017.
[5] V. F. Da Silva, L. F. Canale, D. Spinelli, W.W. Bose-Filho, O.R. Crnkovic, "Influence of Retained Austenite on Short Fatigue Crack Growth and Wear Resistance of Case Carburized Steel", *Journal of Materials Engineering and Performance*, vol. 8, pp. 543-548, 1999.
[6] H. Mohrbacher, "Metallurgical Concepts for Optimized Processing and Properties of Carburizing Steel", *Advances in Manufacturing*, vol. 4(2), pp. 105-114. 2016.
[7] A. Arulbrittoraj, P. Padmanabhan, M. Duraiselvam, R. Srinivasan, G. Ebenezer, "The Effect of Sliding Wear Parameters on Carburized AISI1040 Steel", *Journal of Mechanical Science and Technology*, vol. 30, pp. 1825-1833, 2016.
[8] P. Shukla, S. Awasthi, J. Ramkumar, K. Balani, "Protective Trivalent Cr-Based Electrochemical Coatings for Gun Barrels", *Journal of Alloys and Compounds*, vol. 768, Nov., pp.1039-1048, 2018.

[9] S. Li, L. Wang, G. Yang, "Surface Damage Evolution of Artillery Barrel Under High-Temperature Erosion and High-Speed Impact", *Case Studies in Thermal Engineering*, vol. 42, 102762, 2023.
[10] D. Dobrocký, P. Maňas, Z. Pokorný, Z. Studený, "The Influence of Plasma Nitriding Process on Mechanical Properties of 14NiCr14 Steel", *Solid State Phenomena*, vol. 258, Dec., pp. 542-545, 2017.
[11] Y.Nie, J.Zhang, "Cyclic Impact-Sliding Fatigue Wear Testing Instrument", *US Patent No. 8,402,811*, https://patents.google.com/patent/US8402811B2/en, 2013.
[12] M. Izciler, M. Tabur, "Abrasive Wear Behavior of Different Case Depth Gas Carburized AISI 8620 Gear Steel", *Wear*, vol. 260, pp. 90-98, 2006.
[13] S. Ates, O. Aslan, M. Tümer, C.F. Arisoy, "Impact Sliding Wear Behavior of Stellite 6 And Stellite 12 Hardfacings", *Materials Chemistry and Physics*, vol. 313, 128762. 2024.
[14] D. Dobrocky, Z. Joska, Z. Studeny, Z. Pokorny, E. Svoboda, "Quality Evaluation of Carburized Surfaces of Steels Used in Military Technology", *Manufacturing Technology*, vol. 20 (2), pp. 152-161, 2020.
[15] P. Zhang, F C. Zhang, Z.G. Yan, T.S. Wang, L.H. Qian, "Wear Property of Low-Temperature Bainite in the Surface Layer of a Carburized Low Carbon Steel", *Wear*, vol. 271(5-6), pp. 697-704, 2011.

Eurasian Journal of Science Engineering and Technology

Research Article

CONVCAT: A NEW CLASSIFICATION APPROACH USING UC MERCED AND RESISC45 DATASETS

Selim SÜRÜCÜ[1,*], Esma DEMİRKIRAN[2]

[1] *Çankırı Karatekin University, Faculty of Engineering, Department of Computer Engineering, 18100, Çankırı, Türkiye*
[2] *Yeşilova Anatolian High School, Hatay, Türkiye*

ABSTRACT

With advances in Earth observation systems, the importance of remote sensing data is increasing daily. These data are used in various fields ranging from image segmentation to terrain classification, from disaster impact assessment to climate change analysis. The use of remotely sensed images for terrain classification has been the subject of a number of studies. This study proposes a new method for terrain classification in the UC Merced Land Use Dataset and RESISC45 remote sensing images. This method is called ConvCat model, which is a combination of classical convolutional layer and CatBoost models. The performance of this model is measured in terms of accuracy, the Matthews Correlation Coefficient (MCC) and the Cohen's Kappa metrics. The results are compared with ensemble models (XGBoost, CatBoost), with ConvXGB, a combination of convolutional learning and XGBoost, and with ResNet50, one of the most widely used transfer learning models. The developed ConvCat model outperformed the other models, achieving an accuracy of 97.44% on the UC Merced data set and an accuracy of 96.89% on the Resisc45 data set. This study shows that our newly developed model provides the best results for the classification problem based on remote sensing images.

Keywords: Remote Sensing, Scene Classification, Ensemble Learning, ConvCat, Ground Observation Classification

1. INTRODUCTION

Remote sensing (RS) refers to the process of remote observation, recording and measurement of the properties of a surface or object and the technology that makes it possible. Remote sensing can be performed with many different tools and devices such as satellites, aircrafts (aircraft, drones, etc.). Today, with the increase in the number of satellites of states and companies, there is a high increase in UA data. Researchers are carried out on these data in many different fields from agriculture to defense.

Information extraction from UA data can usually be done by image classification techniques. UA image classification attempts to assign an area or pixel to a class (label) using certain features. These features can be spectral characteristics, colour or building materials. These features can be used for classification processes in many different subjects and areas, from crops in agricultural lands to the condition of forested areas, from damaged areas to the detection of landslide areas.

Scientists and researchers have made great efforts to develop advanced classification approaches and techniques to improve the accuracy of remote sensing image classification. With the advances in artificial intelligence technologies, there has been a great increase in the number of studies in the field of UA.

Recent years have seen significant advances in the application of Artificial Intelligence (AI) and in particular Deep Learning (DL) techniques to remote sensing imagery. These techniques allow useful information to be extracted from satellite imagery. This information can be used in a variety of applications. For example, it can be used in agricultural activities such as monitoring of the condition of agricultural land, identification of crop species and environmental monitoring through forest tracking. It can also be used for damage assessment in the event of disasters, while the tracking of objects (vehicles, ships, aircraft, etc.) can be used for many different reasons, such as defense and security.

The contributions of this paper are;

- This paper proposes a new convolution-based model for classifying UA data. This proposed method is run on UC Merced and RESISC45 datasets.
- The performance of this model is compared with another convolution-based model, ConvXGB, as well as classical deep learning methods.
- Cohen cappa and MCC metrics, which are rarely used in remote sensing imagery, were used to measure model success.
- The proposed model seems to give the most successful results.

* Corresponding author, e-mail: selimsurucu@karatekin.edu.tr, (S. Sürücü)
Recieved: 09.01.2024 Accepted: 06.05.2024
doi: 10.55696/ejset.1417171

After the introduction, the article continues with a literature section including recent studies. Section 3 is the methodology where the datasets, models and metrics are explained. Section 4, the results section, presents the results obtained from the developed model and other models. The discussion section, which includes other studies and general comparisons, takes the 5th place in the paper. The last section is conclusion and future work section.

2. LITERATURE REVIEW

In their study using resisc45 and UCMerced datasets, Tombe et al. proposed a method called deep coherence feature learning (ADCFL) [1]. The ADCFL method uses a convolutional neural network to extract spatial feature information from an image in combination with filters, which is then fed into a multigranular forest for feature learning and classification through majority voting with ensemble classifiers. Their method combined with VGG16 gave the best result with an accuracy of 91.05% on the Resisc45 dataset.

In a study on agricultural lands in Ukraine, an unsupervised neural network and a supervised neural network model were proposed for land cover and crop type classification from multi-temporal multi-source satellite images. The images used in the study were obtained from Landsat-8 and Sentinel-1A satellites, and an accuracy of 85% was achieved [2].

In another study, a peak-wave sparse cooperative representation convolutional neural network (RRSCRN) algorithm is proposed for remote sensing image classification. RRSCRN enables to learn the relationship between competition and co-operation of the remote sensing image to be sparsely classified, and to better learn the features of the remote sensing image. This algorithm is tested on Pavia University and Indian Pines datasets. This algorithm has shown better performance compared to traditional remote sensing image classification methods [3].

Yu et al. (2018) tried to classify remote sensing images based on the improved KNN (k nearest neighbour) algorithm. They improved the KNN algorithm with two methods. Firstly, they used the weighted distance to improve the locality of the KNN algorithm. Secondly, they used support vector machine to improve the accuracy. For the University of Pavia dataset, the accuracy of the improved KNN algorithm is 95.6%, while the accuracy of the traditional KNN algorithm is 94.8%. For the Pines dataset, accuracy values of 92.7% and 92.1% were obtained, respectively [4].

In another study, multi-label remote sensing image classification was studied using capsule networks, which can better capture the features of objects than traditional neural networks. For the University of Pavia dataset, the accuracy value of the capsule networks was 96.9%, while the accuracy value of the traditional neural networks was 95.2%. For Indian Pines dataset, 94.8% and 93.9% accuracy values were calculated respectively. In this study, it is shown that capsule networks achieve a higher classification performance than traditional neural networks. In the study in which success measurement was performed using RESISC45 dataset with ANN by feature extraction with enhanced attention module, an accuracy value of 94.29% was obtained. It was observed that feature extraction with the enhanced attention module achieved good performance compared to classical methods [5].

Dai et al. proposed an improved remote sensing scene image classification model to improve the overall accuracy (OA) of the AlexNet model [6]. They used Layer Normalization (LN) instead of Local Response Normalization (LRN) in AlexNet and modified the model by changing the convolution kernel to 7×7. They also used Block Attention Module (CBAM) and Compression and Excitation Module (SEM) to reduce the effect of backgrounds. An accuracy of 96.29% was achieved on the Resisc45 dataset.

In another study, Zhao et al. proposed a model called CGINet. They developed this model by combining global context and part-level discriminative features in a unified framework [7]. In another study, a hierarchical feature fusion with patch expansion of the transformer (HFFT-PD) was developed. The proposed model consists of a hierarchical transformer fusion (HTM) block and a lightweight adaptive channel compression (LACC) module. The most important contribution of this work is the newly proposed Patch Expansion strategy. In this strategy, it acts as a reassembly operator based on patch features [8]. In the artificial intelligence model developed by Sharma and Gupta with a hybrid approach, they used three attention mechanisms as channel, spatial and local relation attention with EfficientNet model. They dimensionally reduced the feature vector with PCA and performed classification with SVM. They tested this model on UC Merced, EuroSAT, MLRSNet and RSI-CB256 datasets and obtained an accuracy of 97.11% in UC Merced dataset [9].

3. MATERIAL AND METHOD

3.1 Dataset

Two datasets were used in this study.

UC Merced Land Use Dataset = UC Merced is a dataset created from 21 different urban areas. These classes are agriculture, aircraft, baseball diamond, baseball diamond, beach, buildings, chaparral, chaparral, denserresidential, dense

residential, forest, motorway, golf course, golfcourse, port, intersection, mediumresidential, mobilehome park, mobilehomepark, overpass, parking lot, river, runway, sparseresidential, storage tanks, tennis court, tenniscourt. In this dataset, which contains 2100 images in total, each class consists of 100 images. In addition, these images are RGB images with 256x256 pixel dimensions.

RESISC45 = It is a dataset used for Remote Sensing Image Scene Classification. The RESISC45 dataset consists of a set of satellite images containing 45 different classes of natural and human scenes. These classes include forests, farmland, motorways, beaches, lakes, buildings and other landscape elements. Each image consists of multi-spectral and/or hyper-spectral data from satellite sensors. The images contain high resolution pixels collected at different wavelengths.

To compare these two datasets;

- The UC Merced Land Use Dataset was launched in 2010, while RESISC45 was launched in 2017. As can be understood from this point, RESISC45 is a new dataset compared to the other dataset.
- While the UC Merced Land Use Dataset contains 2100 images in 21 different categories, the RESISC45 dataset contains 31500 images in 45 different categories. As can be seen, the RESISC45 dataset contains a much broader categorisation and more images, while the UC Merced Land Use Dataset focuses on specific land use and land cover types.
- Both datasets are 256x256 pixels in size and RGB.

3.2 Metrics

In this study, 3 different metrics were used to calculate the measurement of the success of the models.

Accuracy = It is a measure of success obtained by dividing the correctly predicted data (TP+TN) by the total data and gives a value between 0%-100% [10].

$$Accuracy = \frac{TP+TN}{TP+FP+TN+FN} \tag{1}$$

Matthews Correlation Coefficient (MCC) = MCC measures how well the classification results match the actual class labels and is used to calculate the classification performance [11]. A result between -1 and +1 is produced. If +1, this means a perfect classification.

$$MCC = \frac{TP\ x\ TN - FP\ x\ FN}{\sqrt{(TP+FP)(TP+FN)(TN+FN)(TN+FN)}} \tag{2}$$

Cohen's Cappa = Cohen's Kappa is calculated using a table based on the probability of observers being placed in their randomly selected category. The coefficient value usually ranges between -1 and 1. 1 means perfect agreement, 0 means randomness and -1 means complete disagreement [12].

$$k = \frac{p_0 - p_e}{1 - p_e} \tag{3}$$

Meanings of the expressions in the equation;

- p_e = Overall accuracy of the model
- p_0 = Agreement between model predictions and actual class values

3.3 Models

3.3.1 Convolutional neural networks (CNNs)

CNNs are a type of deep learning model designed to mimic the image processing ability of the human brain and are used in many fields such as image processing and natural language processing. CNNs consist of multiple convolution layers to extract features of the image and one or more fully connected layers to classify the image. In addition to these layers, there are many different layers such as the pooling layer, which is used to reduce the output of the convolution layers, the input layer to receive the input data to the neural network, and the dropout layer to reduce overfitting during training.

CNNs constitute one of the most basic processes of machine learning. It is widely used as a basic model for various tasks from image classification to object detection.

3.3.2 XGBoost

XGboost is a kind of gradient boosting method. Gradient Boosting is an ensemble learning method that builds a stronger model by combining the predictions of multiple models [13]. Gradient Boosting builds a powerful learning model by combining simple models whose predictions are often inaccurate [14]. Gradient boosting methods are optimized for high performance, scalability and accuracy. The XGBoost algorithm is a high-performance version of the Gradient boosting algorithm optimized with various modifications. This algorithm is among the most preferred algorithms among decision tree algorithms for many reasons such as the best performance, high prediction power, and the ability to manage empty data.

3.3.3 CatBoost

CatBoost is based on an algorithm similar to XGBoost. CatBoost differs from XGBoost by using a more efficient technique to process categorical data. In addition to this difference, it can work with larger data sets than the XGboost algorithm. As a powerful algorithm in machine learning studies, it can be used for many tasks such as classification, regression and time series prediction.

3.3.4 ConvXGB (CNN + XGBoost)

Thongsuwan et al. developed a new deep learning approach for the classification problem that combines the performances of a convolutional neural network and Extreme Gradient Boosting (XGBoost) models. Figure 1 shows the architecture of this proposed model [15].

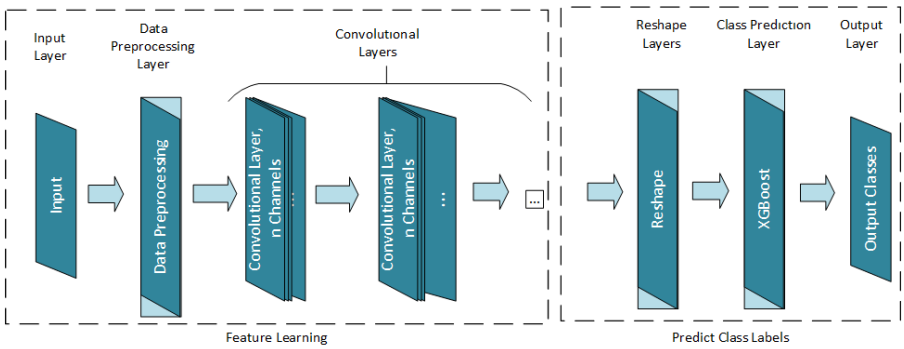

Figure 1. Architecture of the ConvXGB model

3.3.5 ResNet50

In 2015, He et al. announced in a paper titled "Deep Residual Learning for Image Recognition". The expression 50 in the nomenclature refers to the total number of convolution layers. It was developed as a solution to the performance degradation experienced in very deep networks [16]. As a solution method, shortcuts have been added between network layers. ResNet50 has been a turning point for deep learning networks. Good results can be obtained for many problems compared to other models. The architecture of this model is given in Figure 2.

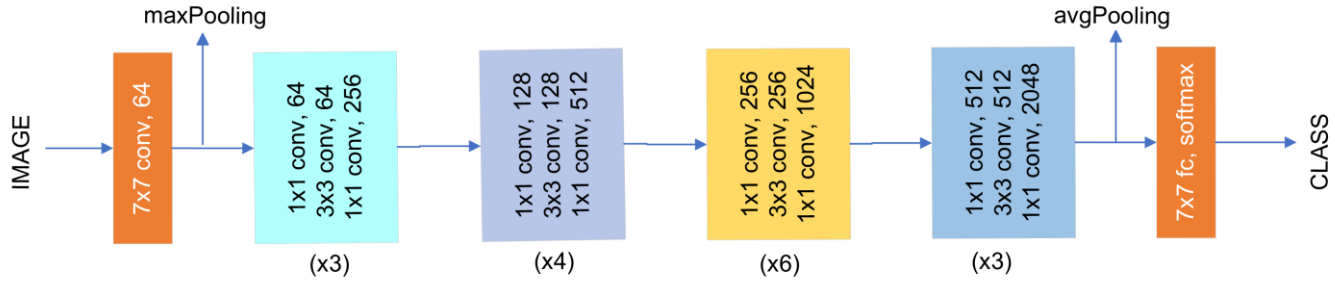

Figure 2. Architecture of the ResNet50 (Layers are successively interconnected.)

3.3.6 ConvCat (CNN + CatBoost)

In this study, we developed the ConvCat model inspired by the ConvXGB model. In our architecture, CatBoost algorithm is used for the class prediction task after the convolution layers. The architecture of this proposed model is shown in Figure 3.

Figure 3 shows that the classification layer, which is the last layer of the classical cnn structure, has been removed. In its new form, the classical CNN structure was used for feature extraction. After feature extraction, the extracted features were given to the catboost part of the model and classification was performed. By combining these two models, the feature extraction of the CNN structure and the power of the catboost model in classification are combined.

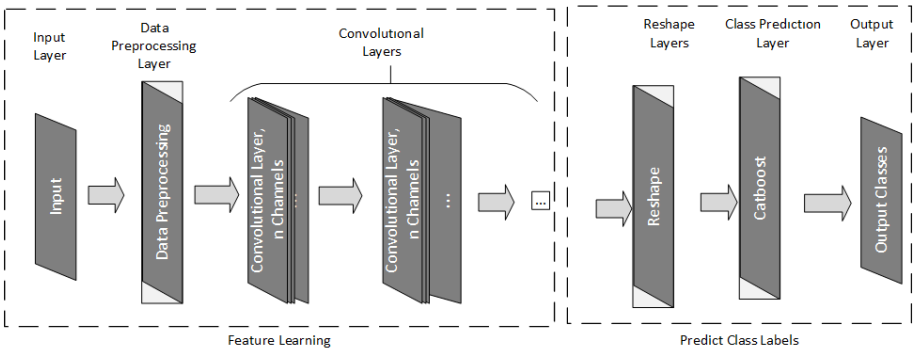

Figure 3. Architecture of our proposed ConvCat model

4. RESULTS AND DISCUSSION

In this study, 30 epoch trainings were performed on a machine with v100 GPU as the working environment and results were obtained.

When Table 1 is analysed, the ConvCat model we developed gave better results than the ConvXGB model developed by Thongsuwan et al. The ConvCat model achieved about 2 times more success than the classical ensemble (XGBoost, CatBoost) models. In addition, ConvCat and ConvXGB showed high success compared to the ResNet model, one of the most common transfer learning models. In addition to the accuracy metric, it was also observed that it gave the best results according to the MCC and Cohen's Cappa metrics.

Table 1. Results Obtained From models according to UC Merced and Resics45 Datasets

	UC Merced			**RESISC45**		
	Accuracy	**MCC**	**Cohen's Cappa**	**Accuracy**	**MCC**	**Cohen's Cappa**
XGBoost	42%	0.478	0.4425	70%	0.707	0.7001
CatBoost	55.6%	0.554	0.5236	66.6%	0.65	0.677
ResNet50	80.88%	0.80	0.7789	75%	0.755	0.781
ConvXGB	87%	0.857	0.866	82.75%	0.838	0.8155
ConvCat	**97.44%**	0.971	0.962	**96.89%**	0.9645	0.9505

Dai et al. obtained one of the best results with the RESISC45 dataset used in this study. Dai et al. obtained a good result with 96.29% with the improved version of the AlexNet model. With our proposed model, ConvCat, we obtained 96.89% accuracy. Compared to other studies in the literature, we obtained the best accuracy on the Resisc45 dataset. Table 2 gives an overview of the results.

Table 2. Results of studies with the Resics45 dataset in the literature

Paper	**Method**	**Result (Accuracy - %)**	**Year**
[1]	VGG16-Classifier-fusion(proposed)	91.05	2021
[4]	ANN	94.29	2021
[6]	Improved AlexNet (proposed)	96.29	2022
Our Proposed	ConvCat	96.89	

When the studies in the literature using the UC Merced dataset are examined, it is seen that the accuracy values are very close to each other. Using the same dataset, we obtained an accuracy of 97.44% with our ConvCat model. Although we obtained a better result than the studies in the literature, there is a very small difference. Table 3 shows the information about the studies in the literature.

Table 3. Results of studies with the UC Merced dataset in the literature

Paper	Method	Result (Accuracy - %)	Year
[1]	VGG16-Classifier-fusion(proposed)	96.55	2021
[6]	Improved AlexNet (proposed)	96.57	2022
[9]	EfficientNet + PCA+SVM	97.11	2023
Our Proposed	ConvCat	97.44	

5. CONCLUSION

This study shows that instead of using classical deep learning models for image classification problems, better results can be obtained by combining several models. In the combination models, the choice of models can be random as long as the inputs and outputs are taken into account. However, it is recommended to prefer transfer learning models in the feature extraction phase, as transfer learning models are more successful in feature extraction than other models. For classification, ensemble models can be preferred. This study shows that for the problem of terrain classification in remote sensing images, the combination of classical convolutional layers in the feature extraction phase and the CatBoost model, which is an ensemble model used as a classifier, gives the best result in the literature. In addition, it may be preferable to combine new models, such as Transformar, which has been developed in the last few years, with the classical models.

Furthermore, most of the studies on terrain classification in the literature have measured their success in terms of the accuracy metric. In this study, the MCC and Cohen's Cappa metrics were used in addition to the accuracy metric. These metrics have been used in land classification studies and have been shown to be useful.

In future studies, the ConvCat model proposed in this study can be adapted and used for many problems other than the classification of land. It can be preferred as a new approach to classifying problems.

SIMILARITY RATE: 14%

AUTHOR CONTRIBUTION

First Author: initiated the research idea, developed, analyzed and interpreted the data and wrote the manuscript
Second Author: suggested the research methods, structured the paper and edited the manuscript.

CONFLICT of INTEREST

The authors declared that they have no known conflict of interest.

REFERENCES

[1] R. Tombe and S. Viriri, "Adaptive Deep Co-Occurrence Feature Learning Based on Classifier-Fusion for Remote Sensing Scene Classification," in IEEE Journal of Selected Topics in Applied Earth Observations and Remote Sensing, vol. 14, pp. 155-164, 2021, doi: 10.1109/JSTARS.2020.3044264.

[2] N. Kussul, M. Lavreniuk, S. Skakun and A. Shelestov, "Deep Learning Classification of Land Cover and Crop Types Using Remote Sensing Data," in IEEE Geoscience and Remote Sensing Letters, vol. 14, no. 5, pp. 778-782, May 2017, doi: 10.1109/LGRS.2017.2681128.

[3] F. An and J. Liu, “Remote Sensing Image Classification algorithm based on ridge wave sparse collaborative representation convolutional neural network,” Multimedia Tools and Applications, vol. 80, no. 21–23, pp. 33099–33114, 2021. doi:10.1007/s11042-021-11406-w

[4] Z. Yu, "Research on Remote Sensing Image Terrain Classification Algorithm Based on Improved KNN," 2020 IEEE 3rd International Conference on Information Systems and Computer Aided Education (ICISCAE), Dalian, China, 2020, pp. 569-573, doi: 10.1109/ICISCAE51034.2020.9236884.

[5] Z. Zhao, J. Li, Z. Luo, J. Li and C. Chen, "Remote Sensing Image Scene Classification Based on an Enhanced Attention Module," in IEEE Geoscience and Remote Sensing Letters, vol. 18, no. 11, pp. 1926-1930, Nov. 2021, doi: 10.1109/LGRS.2020.3011405.

[6] D. Dai, Xu, W., and Huang, S., "Improved AlexNet and embedded multi-attention for remote sensing scene image classification", in Society of Photo-Optical Instrumentation Engineers (SPIE) Conference Series, 2022, vol. 12506. doi:10.1117/12.2661951.

[7] Zhao, Y., Chen, Y., Xiong, S., Lu, X., Zhu, X. X., & Mou, L., "Co-Enhanced Global-Part Integration for Remote-Sensing Scene Classification." IEEE Transactions on Geoscience and Remote Sensing. 62, 1-14, 2024.

[8] Chen, X., Ma, M., Li, Y., Mei, S., Han, Z., Zhao, J., & Cheng, W., "Hierarchical Feature Fusion of Transformer With Patch Dilating for Remote Sensing Scene Classification." IEEE Transactions on Geoscience and Remote Sensing. 61, 1-16. 2023.

[9] Sharma, I., and Savita G.. "A Hybrid Machine Learning and Deep Learning Approach for Remote Sensing Scene Classification." 2023 14th International Conference on Computing Communication and Networking Technologies (ICCCNT). IEEE, 2023.

[10] M. Hossin, Sulaiman M.N, "A Review on Evaluation Metrics for Data Classification Evaluations", in International Journal of Data Mining & Knowledge Management Process, 2015, 10.5121/ijdkp.2015.5201.

[11] P. Baldi, S. Brunak, Y. Chauvin, C. A. F. Andersen, and H. Nielsen, 'Assessing the accuracy of prediction algorithms for classification: an overview', Bioinformatics, vol. 16, no. 5, pp. 412–424, 05 2000.

[12] J. Cohen. "A Coefficient of Agreement for Nominal Scales." Educational and Psychological Measurement 20 (1960): 37 - 46.

[13] T. Chen and C. Guestrin, 'XGBoost: A Scalable Tree Boosting System', 08 2016, pp. 785–794.

[14] Y. Lecun, L. Bottou, Y. Bengio and P. Haffner, "Gradient-based learning applied to document recognition," in Proceedings of the IEEE, vol. 86, no. 11, pp. 2278-2324, Nov. 1998, doi: 10.1109/5.726791.

[15] S. Thongsuwan, S. Jaiyen, A. Padcharoen, and P. Agarwal, 'ConvXGB: A new deep learning model for classification problems based on CNN and XGBoost', Nuclear Engineering and Technology, vol. 53, no. 2, pp. 522–531, 2021.

[16] K. He, X. Zhang, S. Ren, and J. Sun, 'Deep Residual Learning for Image Recognition', 2016 IEEE Conference on Computer Vision and Pattern Recognition (CVPR), pp. 770–778, 2015.

Eurasian Journal of Science Engineering and Technology

Research Article

MODELING THERMAL BEHAVIOR IN HIGH-POWER SEMICONDUCTOR DEVICES USING THE MODIFIED OHM'S LAW

Alex Mwololo KIMUYA[1,*]

[1]*Department of Physical Science (Physics), Meru University of Science and Technology, Kenya*
Phone: +254704600418

ABSTRACT

This paper addresses the challenge of thermal management in high-power semiconductor devices, where increasing power densities and complex operating environments demand more accurate thermal prediction methods. Traditional approaches often rely on simplified models that do not account for the crucial factor of temperature-dependent resistance variations. This limitation leads to inaccurate device temperature predictions, potentially compromising device reliability. This work proposes a novel approach for thermal management by introducing the first empirical application of a Modified Ohm's Law. This modified law incorporates an exponential term to account for the non-linear relationship between temperature, current, and resistance. The paper demonstrates through simulations and empirical validation that the Modified Ohm's Law offers a more accurate representation of thermal behavior compared to the standard version. This translates to more precise predictions of device temperature, especially during periods of rapid temperature changes. The validation process goes beyond simply establishing the Modified Ohm's Law. It provides valuable insights into the thermal dynamics of the device, allowing for the refinement of simulation parameters used to assess various cooling strategies. These strategies include simulating different heat sink geometries and materials, modifying airflow rates over the device's surface, and exploring the impact of Thermal Interface Materials (TIMs) between the device and the heat sink. By incorporating these elements, the simulations provide a more comprehensive picture of the device's thermal behavior under various operating conditions and cooling configurations. Ultimately, this paper not only advances the theoretical understanding of thermal management but also offers practical benefits. Through enabling more accurate thermal predictions, the Modified Ohm's Law model paves the way for informed decision-making in device design and optimization.

Keywords: Thermal management, High-power semiconductor devices, Modified Ohm's Law, Nonlinear relationship, Temperature-dependent resistance, Heat dissipation, Simulation, Thermal behavior, Accuracy, Device temperature

1. INTRODUCTION

High-power semiconductor devices are indispensable components in a wide array of electronic systems, spanning industries such as power electronics, automotive engineering, telecommunications, and renewable energy [1,2]. These devices serve as the backbone of modern electronic systems, facilitating the delivery of high levels of power and efficiency required to drive various applications [2]. Whether powering electric vehicles, transmitting data across telecommunications networks, or harvesting renewable energy, high-power semiconductor devices form the cornerstone of technological advancements across diverse sectors [3,4]. However, as technological advancements drive the proliferation of high-power semiconductor devices, the accompanying increase in power densities poses significant challenges in terms of thermal management [5-7]. With more power packed into smaller footprints, these devices inevitably generate substantial amounts of heat during operation [7]. Effective thermal management becomes crucial to prevent excessive heat buildup, which can compromise device performance and reliability. Without adequate cooling mechanisms in place, high temperatures can lead to thermal stress, material degradation, and ultimately, device failure [8,9]. The relentless pursuit of miniaturization and efficiency in electronic systems intensifies the need for innovative thermal management solutions. Dissipating heat effectively and maintaining temperatures within safe operating ranges is paramount for achieving optimal device performance and reliability. Therefore, thermal management becomes increasingly crucial as power densities climb to meet the demands of emerging technologies like electric vehicles, 5G telecommunication networks, and renewable energy systems [6]. The escalating power densities of high-power semiconductor devices are a direct consequence of the miniaturization trend and the drive for more efficient electronics [10,11]. As these devices evolve to meet the demands of modern technology, they can handle significantly more power within a fixed volume. However, this miniaturization with increased power density comes at a significant cost-the generation of substantial heat during operation [10]. If not managed effectively, this heat can severely impact the performance and reliability of high-power semiconductor

* Corresponding author, e-mail: alexkimuya23@gmail.com (A. M. Kımuya)
Recieved: 02.04.2024 Accepted: 24.05.2024
doi: 10.55696/ejset.1463554

devices [5]. As heat accumulates within the devices, temperatures can rise beyond safe operating limits established by manufacturers. These elevated temperatures not only degrade the immediate performance of the devices but also compromise their long-term reliability. Over time, prolonged exposure to high temperatures can accelerate device aging, degrade materials, and ultimately lead to premature device failure [5,12]. Traditional thermal management approaches often rely on basic linear models, such as Standard Ohm's Law, to predict and mitigate heat generation in semiconductor devices [13]. While these models can be adequate for low to moderate power densities, they struggle with the complexities of thermal behavior exhibited by high-power devices. Notably, linear models may neglect significant non-linear effects that become more pronounced at higher power densities [14,15]. Non-linear phenomena such as temperature-dependent changes in resistance and thermal conductivity significantly impact the thermal behavior of high-power semiconductor devices [16,19]. These non-linearities cause deviations from linear model predictions, rendering them insufficient for accurate thermal modeling and management in high-power applications. Consequently, the need for more sophisticated thermal management techniques that account for these non-linear effects and provide more accurate performance and reliability predictions has become increasingly recognized. This paper proposes a novel method for managing heat in high-power semiconductor devices. It focuses on using a modified version of Ohm's Law to address this challenge empirically. This modified version incorporates the exponential relationship between temperature, resistance, and current. The objective is to offer a more precise and reliable way to model the thermal behavior of these devices. Through empirical validation and simulations, we aim to demonstrate how this Modified Ohm's Law can improve cooling strategies and mitigate thermal issues in high-power semiconductor devices. The paper establishes the first empirical applications of the Modified Ohm's Law in addressing thermal management challenges in high-power semiconductor devices. A comprehensive framework integrating theoretical insights with practical experimentation advances understanding of thermal dynamics and facilitates more effective cooling strategies. The benefits of employing the Modified Ohm's Law instead of traditional linear models are elucidated to aid in advancing thermal management techniques. By delving into the theoretical underpinnings of the Modified Ohm's Law, outlining the methodology for empirical validation, presenting simulated experiments, and discussing the implications of findings, a holistic understanding of its role in addressing thermal management challenges and unlocking the full potential of high-power semiconductor devices in diverse electronic applications is provided.

2. LITERATURE REVIEW

Thermal management in high-power semiconductor devices is a critical aspect of modern electronics, with various approaches and models developed to address associated challenges. This section provides an overview of current approaches, identifies their limitations, and highlights the need for innovative solutions to optimize device performance and reliability.

2.1 Historical Context

Early efforts in thermal management focused on developing basic heat dissipation techniques to combat rising temperatures in semiconductor devices [20-23]. The primary concern during this period was preventing overheating and ensuring reliable operation of electronic components. Simple solutions like heat sinks and fans became the workhorses of thermal management, dissipating heat generated by high-power devices to minimize thermal damage and extend the lifespan of semiconductor systems [23-25]. These pioneering thermal management techniques were the first steps towards addressing the thermal challenges of high-power devices. Through implementing these fundamental yet effective heat dissipation mechanisms, engineers laid the groundwork for the development of more sophisticated thermal management strategies in the years to come [26,27]. These foundational techniques not only helped mitigate immediate thermal concerns but also paved the way for more advanced cooling solutions as power densities continued to increase [26]. Through empirical experimentation and iterative refinement, engineers gained valuable insights into the thermal behavior of semiconductor devices and the effectiveness of different cooling methods. This period of experimentation and innovation laid the groundwork for the evolution of thermal management practices, providing a foundation for the development of more comprehensive and efficient cooling strategies in the future [20,28,29].

2.2 Current Approaches

Current thermal management practices for high-power semiconductor devices often rely on simplistic models, with a primary focus on the Standard Ohm's Law for temperature prediction and cooling strategy development [30]. This approach treats thermal behavior as a linear relationship between temperature (T), thermal resistance (R_{th}), and current (I). However, recent research highlights the limitations of these linear models in capturing the complexities of heat generation and transfer within high-power devices [31-33]. For instance, studies on power electronics modules have shown that thermal resistance is not constant, but rather increases as temperature rises [34,35]. This non-linearity can significantly affect temperature predictions based on the Standard Ohm's Law, potentially leading to underestimates of heat generation and overestimates of cooling effectiveness. Consequently, overdependence on linear models can result in suboptimal cooling solutions, as evidenced by cases where high-power LED

arrays experienced overheating and reduced lifespan due to inaccurate thermal management strategies [36]. These limitations become even more critical as power densities continue to increase and operating conditions become more dynamic. In high-power applications like data centers and electric vehicles, where precise thermal control is crucial for performance and reliability, linear models may struggle to predict temperature variations accurately, potentially leading to thermal runaway and device failure as discussed by [37].

2.3 Limitations of Current Approaches

Thermal management of high-power semiconductor devices faces several limitations with the rise of complex operating environments. While existing approaches offer a foundation, they often struggle to keep pace with the evolving demands of these devices.

A key constraint lies in the extensive use of linear models, like those derived from Standard Ohm's Law, to predict thermal behavior [1,2]. These models offer advantages in their simplicity and ease of implementation. However, they inherently disregard the non-linear effects caused by temperature dependence of resistance. This becomes particularly problematic in high-power devices that experience dynamic operating conditions and inevitable temperature fluctuations. A study by [38] demonstrated that neglecting such non-linear behavior in a high-power GaN transistor model led to significant underestimation of junction temperatures, potentially resulting in device failure under high-stress operating conditions.

Furthermore, commonly employed empirical methods in thermal management can lack the precision needed to capture the nuances of thermal behavior under diverse operating conditions. These approaches often rely on experimental data obtained from limited scenarios, such as specific power levels or ambient temperatures [22,25,28,29]. This limited data set fails to capture the complex thermal dynamics encountered in real-world applications, where various environmental factors like fluctuating power loads and changing ambient conditions can significantly impact device temperature. For instance, a study by [39] compared various empirical thermal models for a high-power IGBT module and found that all models exhibited significant deviations from experimental data at operating conditions beyond the limited range used to generate the empirical correlations. This highlights the limitations of such methods in accurately predicting device temperatures across a wide range of operating scenarios.

Current approaches also struggle to adapt to the ever-increasing diversity of operating conditions and device geometries encountered in high-power semiconductor applications [6,8,13,19]. These devices often operate in environments with significant variations in ambient temperature, power levels, and physical configurations. Failing to account for these variations can lead to thermal management strategies that are poorly suited to the specific needs of a device, potentially compromising its performance and reliability. For example, a study by [40] investigated the thermal performance of a high-power LED array under varying operating currents. The results showed that a thermal management strategy designed based on a constant operating current proved inadequate when the current was dynamically adjusted. This emphasizes the need for more adaptable thermal management approaches that can account for the diverse operating conditions experienced by high-power semiconductor devices.

2.4 Emerging Trends and Technologies

Recent advancements in materials science and computational modeling have revolutionized the field of thermal management, offering innovative solutions to the challenges posed by high-power semiconductor devices. These advancements play a significant role in improving thermal management techniques and optimizing device performance, as highlighted by [41,42].

Materials Science Advancements. One of the most exciting frontiers in thermal management for high-power electronics lies in the development of novel materials with exceptional thermal properties. These advancements are crucial for mitigating heat buildup and ensuring optimal device performance ([41,42]). A key area of focus is nanomaterials, particularly graphene and carbon nanotubes. These materials boast remarkably high thermal conductivity, surpassing traditional materials like copper by several orders of magnitude ([43,44]). This translates to significantly more efficient heat transfer within semiconductor devices. For example, studies have demonstrated that incorporating graphene films into device packaging can significantly reduce temperature gradients across the chip [45,46]. This translates to a two-fold benefit-improved device reliability by mitigating localized overheating and enabling miniaturization of electronic components due to more efficient heat dissipation.

Beyond graphene and carbon nanotubes, researchers are actively exploring other promising materials like diamond and boron nitride for their exceptional thermal conductivity. Additionally, the development of composite materials that combine high thermal conductivity fillers with polymer matrices offers a path towards creating lightweight and flexible heat dissipation solutions for various applications ([47,48]). These advancements in materials science are fundamentally transforming thermal management strategies, paving the way for a new generation of high-performance and reliable electronic devices.

Computational Modeling. Advancements in computational modeling have revolutionized the approach to thermal management for high-power semiconductor devices. These advancements empower engineers with powerful tools to analyze and predict thermal behavior within the devices with unprecedented detail. Finite element analysis (FEA) and computational

fluid dynamics (CFD) techniques have become the cornerstones of this revolution, playing a critical role in optimizing device performance and developing effective cooling strategies [49,50].

FEA excels at simulating heat transfer within complex geometries of semiconductor devices. By discretizing the device into a mesh of elements, FEA software can calculate temperature distribution throughout the device under various operating conditions. This allows engineers to identify potential thermal hotspots and assess the effectiveness of different heat sink designs. For instance, a study by [51] employed FEA to simulate the thermal performance of a novel microchannel heat sink design for a high-power LED array. The simulation results guided the optimization of the microchannel geometry, leading to a significant reduction in junction temperature compared to conventional heat sink designs [51].

On the other hand, CFD simulations excel at modeling fluid flow and heat transfer across surfaces. This capability is crucial for analyzing the performance of various cooling systems, such as forced convection cooling using fans or liquid cooling with microfluidic channels. For example, a study by [52] utilized CFD simulations to evaluate the thermal performance of a microfluidic cooling system for a high-power processor. The simulations enabled the researchers to optimize the flow path design within the microchannels, achieving a substantial improvement in heat dissipation from the processor.

By leveraging these computational modeling tools, engineers can explore a vast design space virtually. They can experiment with different materials, device geometries, and cooling system configurations without the need for expensive physical prototypes. This iterative design process facilitated by simulation software significantly reduces development time and cost while optimizing thermal management solutions for specific device requirements.

Novel Cooling Techniques. While advancements in materials and modeling offer significant improvements, novel cooling techniques are emerging to address the thermal challenges of high-power semiconductor devices. These techniques often push the boundaries of conventional heat dissipation methods. One such promising approach utilizes phase-change materials (PCMs) [53,54]. PCMs exhibit a unique property-they can reversibly transition between solid and liquid states. During this phase change, PCMs absorb or release significant amounts of latent heat, acting as a thermal buffer. This makes them ideal for thermal energy storage and passive cooling applications in electronic devices [54]. For instance, a PCM could be embedded within the device packaging or heat sink. As the device heats up, the PCM absorbs the excess heat by melting. When the device cools down, the PCM solidifies again, releasing the stored thermal energy. This cycle can be repeated, providing a passive and localized cooling mechanism that helps to regulate device temperature. Through incorporating these innovative materials and exploring other emerging methods, researchers are continuously seeking to improve thermal management strategies for high-power electronics, ensuring optimal device performance and reliability.

Microfluidic Cooling Systems. Microfluidic cooling systems are rapidly gaining traction as a promising alternative to conventional air or liquid cooling methods for high-power semiconductor devices. These systems take advantage of microfabrication techniques to integrate miniature channels, typically ranging from 10 to 100 micrometers in width, directly within the silicon substrate of the device. Coolant, such as water or a dielectric fluid, is then circulated through these microchannels. This design offers several advantages over traditional cooling methods. Due to the close proximity of the microchannels to heat sources within the device, microfluidic cooling enables highly efficient heat removal from localized hotspots. This translates to a more uniform temperature distribution across the device compared to conventional cooling approaches where heat transfer is less efficient. The improved thermal management provided by microfluidic cooling allows for significant performance benefits. Studies have shown that microfluidic cooling can lead to substantial reductions in junction temperatures, enabling higher clock speeds and improved device reliability [55,56]. For instance, research by [52] demonstrated a microfluidic cooling system that achieved a 44.4% reduction in peak junction temperature compared to a conventional air-cooled system, allowing the device to operate at a significantly higher clock speed. These advancements highlight the potential of microfluidic cooling to revolutionize thermal management strategies for next-generation high-power electronics.

2.5 Relevance to the Current Study

This section underscores the critical need to overcome limitations in current thermal management techniques for high-power semiconductor devices. Prior research has highlighted the shortcomings of linear models like Ohm's Law in accurately predicting thermal behavior under dynamic conditions. These models often neglect non-linear effects such as temperature-dependent resistance variations, which can negatively impact device performance and reliability. Conversely, research suggests promise in innovative approaches like the Modified Ohm's Law for addressing these challenges. By incorporating non-linear relationships between temperature, resistance, and current, the Modified Ohm's Law offers a more comprehensive framework for modeling thermal behavior in high-power devices [37]. Building on this foundation, this study aims to empirically validate the application of the Modified Ohm's Law for optimizing cooling strategies in high-power semiconductor devices. Through rigorous simulation experiments and analysis, this paper intend to demonstrate the effectiveness of the Modified Ohm's Law in accurately predicting thermal behavior and guiding the design of efficient cooling solutions. Leveraging insights from previous research and emerging technologies, our study contributes to advancements in thermal management within the field of electronics.

3. METHODOLOGY

This section presents a methodology aimed at validating the Modified Ohm's Law using simulated experiments, with a specific focus on its efficacy in managing thermal problems in high-power semiconductor devices. To achieve this goal, essential parameters such as temperature profiles, resistance variations, and current flows will be defined, forming a solid basis for simulating thermal dynamics. Subsequently, a simulation framework is developed, incorporating both Standard Ohm's Law and Modified Ohm's Law principles. Utilizing computational techniques, this framework will be fine-tuned to replicate real-world device characteristics. Through a series of simulated experiments encompassing diverse power levels, temperature gradients, and device geometries, a comparative analysis will be conducted to assess the predictive capabilities of the Standard Ohm's Law and Modified Ohm's Law in thermal management and cooling optimization. This analysis aims to elucidate how well the Modified Ohm's Law aligns with conventional expectations and its potential to enhance device performance and reliability.

3.1 Validation of Modified Ohm's Law through Simulated Experiments

This section describes the implementation of simulated experiments designed to validate the effectiveness of the Modified Ohm's Law in capturing the thermal behavior of high-power semiconductor devices compared to the Standard Ohm's Law. The section leverage the fundamental ingredients established in Appendix IV-Establishing a Simulation Framework to achieve this goal.

3.1.1 Simulation Environment Setup

We establish a framework that replicates real-world conditions experienced in high-power electronic systems, drawing upon the geometric parameters and material properties outlined in Appendix IV. This includes aspects like device geometry, substrate properties, and heat sink design. The methods for modeling heat transfer within the device and defining boundary conditions, such as ambient temperature, are rigorously defined. To model heat transfer accurately, we leverage principles from the field of computational fluid dynamics (CFD) [49,50]. Specifically, we employ the finite element method (FEM), a well-established numerical technique for solving the partial differential equations that govern heat conduction in solids [49]. The governing equation for heat conduction, often referred to as the heat equation, is expressed in Equation (1).

$$\frac{\partial T}{\partial t} = \alpha \nabla^2 T \tag{1}$$

Where T is the temperature distribution within the semiconductor device, t is time, α is the thermal diffusivity of the material, and ∇^2 is the Laplacian operator representing the spatial variation of temperature. Equation (1) describes how temperature changes over time due to heat diffusion within the material.

In addition to modeling heat conduction within the device, we define boundary conditions to simulate heat transfer at device interfaces. These conditions dictate the temperature and heat fluxes at the device's boundaries, including its contact with the surrounding environment. For instance, at the interface between the device and the heat sink, we may specify a convective heat transfer boundary condition to account for the cooling effect of airflow. This approach aligns with Newton's law of cooling, which describes how heat is transferred from the device to the surrounding environment via convection [57]. Mathematically, this boundary condition can be expressed as Equation (2).

$$q = h(T - T_{ambient}) \tag{2}$$

Where q is the heat flux, h is the convective heat transfer coefficient, T is the temperature at the device surface, and $T_{ambient}$ is the ambient temperature. This equation represents Newton's law of cooling and describes how heat is transferred from the device to the surrounding environment via convection. While Equation (2) explicitly represents the boundary condition, the actual implementation within the simulation process (described in the following section) utilizes implicit Dirichlet boundary conditions $T(0) = T_{ambient}$ and $T(L) = T_{hot}$ at the ends of the device [58,59]. This enforces specific temperature values at these designated locations.

3.1.2 Implementation of Standard and Modified Ohm's Law

This section involves the methodology for integrating both the standard and Modified Ohm's Laws applications into the simulation environment. Consider the following computational steps.

To solve equation (1) which represents the one-dimensional heat conduction equation, we will discretize the domain into N_x spatial grid points x_i where $i = 1,2,3, \dots N_x$. This allows us to approximate the spatial derivatives using finite differences. Let Δx be the spatial step size.

We will also consider the boundary conditions provided in equation (3).

- Dirichlet boundary conditions. $T(0) = T_{ambient}$ and $T(L) = T_{hot}$ (3)

To proceed, we approximate the second spatial derivative $\nabla^2 T$ using central finite differences with respect to spatial coordinate x as expressed in equation (4).

$$\frac{\partial^2 T}{\partial x^2} \approx \frac{T_{i+1} - 2T_i + T_{i-1}}{\Delta x^2} \quad (4)$$

Using the finite element method, we approximate the temperature field $T(x)$ as a linear combination of basis functions over finite elements.

Denote N_n to be the total number of nodes.

Then, we have:

$$T(x) \approx \sum_{j=1}^{N_n} N_j(x) \cdot T_j \quad (5)$$

Where $N_j(x)$ is the shape function associated with node j, and T_j is the temperature at node j.

Substituting the discretized second derivative and the FEM approximation into equation (1), we obtain a system of ordinary differential equations (ODEs) for each node i through equation (6).

$$\frac{\partial T_j}{\partial t} = \alpha \cdot \frac{T_{i+1} - 2T_i + T_{i-1}}{\Delta x^2} \quad (6)$$

Substituting this approximation into the one-dimensional heat conduction equation ($\frac{\partial T}{\partial t} = \alpha \frac{\partial^2 T}{\partial x^2}$);

We get:

$$\frac{T_i^{(n+1)} - T_i^{(n)}}{\Delta t} = \alpha \cdot \frac{T_{i+1}^{(n)} - 2T_i^{(n)} + T_{i-1}^{(n)}}{\Delta x^2} \quad (7)$$

Where $T_i^{(n)}$ represents the temperature at spatial point x_i and time step n, and Δt is the time step size.

3.1.3 Solver Implementation Algorithm

The finite difference equation can be solved iteratively using various numerical integration methods. These methods include the explicit or implicit Euler method, Runge-Kutta methods, and the Crank-Nicolson method [60-62]. In this paper, we prioritize computational efficiency by selecting the explicit Euler method. This method is a popular choice due to its straightforward implementation and ease of understanding [60]. While alternative methods like the implicit Euler method and Runge-Kutta methods may offer greater accuracy, the explicit Euler method proves to be computationally less expensive [60,62,63]. This benefit is particularly relevant considering limitations in our available computational resources. Additionally, the explicit Euler method's clear and simple implementation makes it well-suited for solving the finite difference equation within this context.

Boundary Conditions. We apply the Dirichlet boundary conditions established in equation (3); $T(0) = T_{ambient}$ and $T(L) = T_{hot}$ which specify the temperatures at the ends of the semiconductor device. These conditions specify the temperatures at the boundaries of the device, allowing us to capture the heat transfer occurring between the device and its surroundings.

Material Properties and Geometric Parameters. We define the material properties such as thermal conductivity $k(x)$ and geometric parameters like the device length L. These parameters are crucial for accurately modeling heat conduction within the device and determining its thermal behavior.

Application of Ohm's Laws. Once we have obtained the temperature distribution $T(x)$, we apply Ohm's Laws to calculate the current passing through the device. For the Standard Ohm's Law $= {}^{V}/_{R}$, we assign a constant resistance value based on the chosen material properties at a specific reference temperature. The Modified Ohm's Law for this application expressed as; $\left(I_{modified} = a \times e^{\frac{R_{short}}{R_0} \times \frac{x}{L}}\right)$ is integrated into the solver to account for the temperature dependence of resistance. Where V is the voltage, R is the resistance, a is a constant, R_0 is the reference resistance, R_{short} is the short resistance, and x is the spatial coordinate.

These steps constitute the solver algorithm for effectively simulating heat conduction within the semiconductor device, incorporating boundary conditions, material properties, geometric parameters, and the application of Ohm's Laws to accurately capture its thermal behavior. The solver algorithm is implemented according to the computation provided in Appendix I, ensuring a systematic approach to simulate heat conduction within the semiconductor device.

3.2 Simulation Experiment Design

3.2.1 Simulation and Design for Thermal Analysis of Semiconductor Devices

For the thermal analysis of semiconductor devices, the simulation experiment design employed a Monte Carlo simulation approach for synthetic data generation. This method was chosen due to its capability of systematically exploring a vast range of potential operating conditions by introducing perturbations within predefined ranges for material properties and boundary conditions [64]. Leveraging this technique, it was possible to randomly vary parameters like thermal conductivity and boundary temperatures for each sample within the simulation. This variation mimics the inherent uncertainties encountered in real-world scenarios. Subsequently, temperature distributions were computed using the Finite Element Method (FEM), enabling a detailed comprehension of the thermal behavior of the semiconductor device under various operating conditions and cooling strategies. To further enhance the realism of the synthetic data, noise was incorporated into the temperature distributions. This addition accounts for measurement errors and environmental uncertainties that may be present in real-world measurements. The provided simulations through the subsequent sections leverages the solver implementation framework outlined in Appendix I and the synthetic data generated by the simulation data generator described in Appendix II.

Operating Conditions. The initial step involves establishing the operating conditions for the semiconductor device simulation. These conditions encompass a range of parameters that significantly influence the temperature distribution and heat dissipation within the device. The key parameters include;

- **Power Levels.** Varying power levels simulate the device's operation under different workloads, directly impacting heat generation.
- **Heat Loads.** External heat loads represent additional heat sources that the device must dissipate, such as from surrounding components.
- **Ambient Temperatures.** Simulating different ambient temperatures reflects the device's operating environment and its effect on heat transfer.

Through varying these operating conditions, the simulation observes their impact on the thermal performance of the semiconductor device. This allows for the evaluation of different cooling strategies' effectiveness in maintaining optimal operating temperatures.

Cooling Strategies. The simulation experiment subsequently explores various cooling strategies employed to mitigate heat buildup within the device. These strategies encompass a range of techniques that enhance heat transfer from the device to its surroundings.

- **Airflow Rates.** Modifying the airflow rate over the device's surface influences convective heat transfer.

- **Heat Sink Configurations.** Simulating different heat sink geometries and materials evaluates their effectiveness in conducting heat away from the device.

- **Thermal Interface Materials (TIMs).** Varying the TIM properties between the device and the heat sink affects the thermal conductivity at the interface, impacting heat transfer.

The simulation process involves implementing these cooling strategies within the solver framework. The resulting data from each simulation run allows for the assessment of each cooling method's ability to effectively dissipate heat and maintain optimal operating temperatures for the semiconductor device.

Validation Metrics. To compare the results obtained with both the standard and Modified Ohm's Law versions, the experiment defines crucial validation metrics. These metrics serve as quantitative measures for evaluating the accuracy and reliability of the Modified Ohm's Law in predicting the thermal behavior of the semiconductor device compared to the traditional approach. The key validation metrics include;

- **Temperature Distribution.** The temperature distribution within the device provides a detailed picture of hot and cold spots, crucial for identifying potential thermal risks.

- **Maximum Device Temperature.** The peak temperature reached during operation is a critical parameter as it determines the device's reliability and performance.

- **Power Dissipation.** The power dissipated by the device represents the amount of heat it generates, which needs to be effectively managed by the cooling system.

Through analyzing these metrics for simulations run with both standard and Modified Ohm's Law implementations, the experiment aims to establish a clear understanding of the modified Law's effectiveness in accurately predicting the thermal behavior of the semiconductor device. The subsequent section presents the detailed results obtained from the simulation experiments.

4. SIMULATION ANALYSIS AND RESULTS

This section presents the results obtained from the simulation experiments designed to evaluate the thermal behavior of the semiconductor device under various operating conditions and cooling strategies. The analysis focuses primarily on the temperature distribution within the device, a critical factor impacting its performance and reliability.

4.1 Temperature Profiles Using Temperature-Dependent Resistance Models

A crucial aspect of the simulation analysis involves comparing the temperature profiles obtained with both the standard and Modified Ohm's Law implementations. This comparison highlights the impact of incorporating the non-linear behavior of resistance in the modified Law on the predicted temperature distribution. The simulations were conducted across a range of operating conditions, including varying power levels, heat loads, and ambient temperatures. The results consistently demonstrate noticeable differences in the temperature profiles predicted by the two versions of Ohm's Law.

4.1.1 Power Levels

Simulations were conducted using varying power densities to analyze their impact on the temperature distribution within the device, as shown in Figure 1. The results confirm that for both Standard Ohm's Law and Modified Ohm's Law, increasing power densities lead to a rise in temperature throughout the device. However, Figure 1 also reveals that the Modified Ohm's Law consistently predicts slightly higher temperatures compared to the standard approach. The observed discrepancy can be attributed to the non-linear dependence of resistance on temperature incorporated into the Modified Ohm's Law. As the power density increases within the device, so too does the temperature. This rise in temperature results in a greater increase in resistance for the Modified Ohm's Law compared to the Standard Ohm's Law, as evidenced by the wider temperature contours in the Modified Ohm's Law plots of Figure 1. The increased resistance leads to a more significant Joule heating effect, causing a higher predicted temperature according to the Modified Ohm's Law. This effect is most pronounced at higher power densities (300 W/mm^2), where the temperature difference between the two approaches is greatest. A notable observation in Figure 1 is that the hottest region in the temperature distribution for (300 W/mm^2) using the Modified Ohm's Law appears narrower compared to the other cases. This could be due to the following two factors:

- The non-linear effect of temperature on resistance can lead to a sharper temperature gradient near the heat source in the Modified Ohm's Law case, resulting in a narrower hot zone.

- Numerical discretization artifacts inherent to the applied finite difference method might also play a minor role. Further simulations with a finer mesh could be conducted to investigate this possibility, in a separate study.

According to Figure 1, the simulations demonstrate the significant impact of incorporating temperature-dependent resistance into the model. The Modified Ohm's Law predicts a more realistic temperature distribution within the device, particularly at higher power densities.

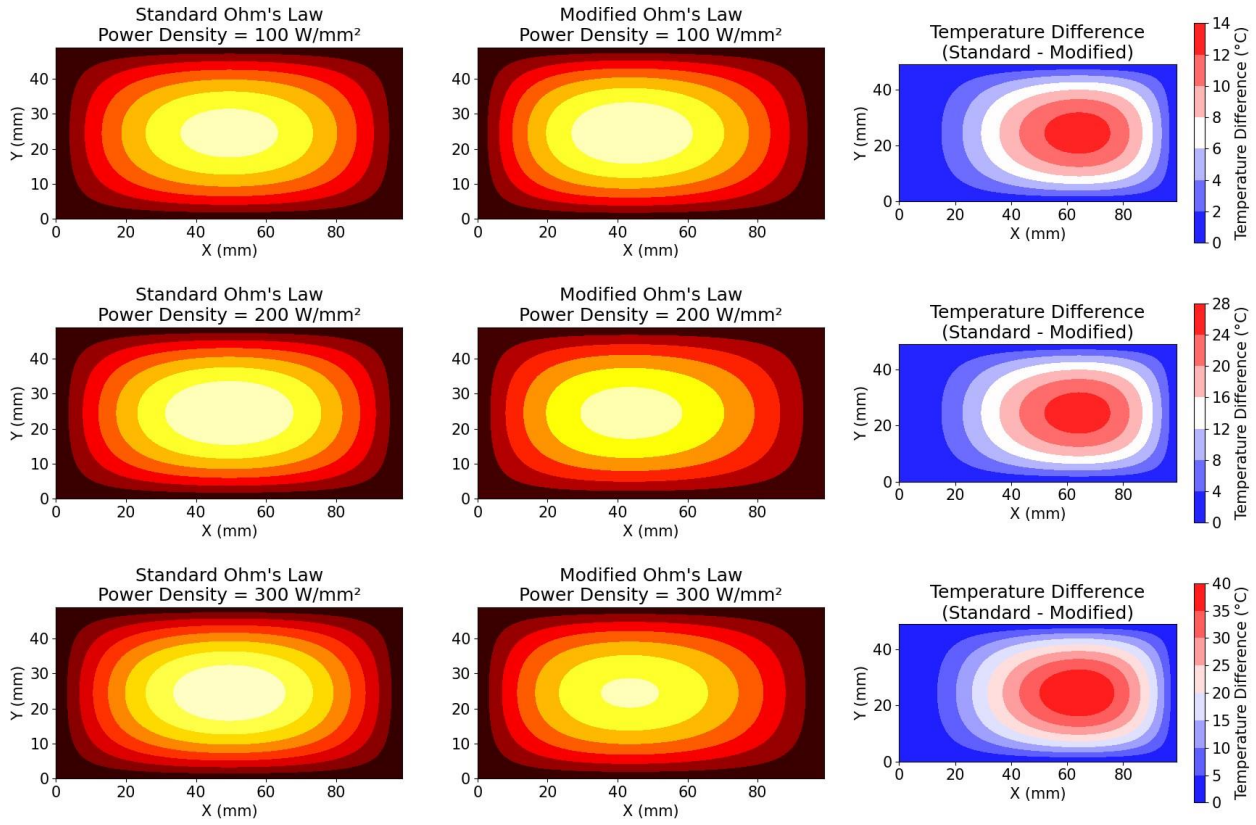

Figure 1. Temperature Distribution within the Device at Varying Power Densities. (*The figure shows the temperature distribution within the device under three different power densities (100 W/mm^2, 200 W/mm^2, and 300 W/mm^2) for both standard and Modified Ohm's Law.*)

Validation Remark 1. Both the standard and Modified Ohm's Laws are applied in the simulation analysis to predict the temperature distribution within the semiconductor device. However, the discrepancy observed between the temperature profiles obtained with the two versions suggests that the temperature-dependent resistance model more accurately captures the device's thermal behavior. The incorporation of temperature-dependent resistance accounts for the non-linear relationship between temperature and resistance, which is often observed in semiconductor materials. Therefore, while both versions of Ohm's Law are used in the analysis, the temperature-dependent resistance model appears to provide a more accurate representation of the device's thermal response under varying operating conditions.

4.1.2 Heat Loads

In this analysis, the influence of external heat loads on temperature distribution within the device was investigated using simulations incorporating various heat loads added to the device model. As illustrated in Figure 2(a) for Standard Ohm's Law and Figure 2(b) for Modified Ohm's Law, both approaches predict a rise in temperature throughout the device due to the presence of the additional heat source. The data in both figures shows a clear trend of increasing temperature throughout the device as the external heat load increases (represented by Load in Figure 2(a) for Standard Ohm's Law). This aligns with the core principle of

Standard Ohm's Law, where $V = IR$ ($Voltage = Current\ x\ Resistance$) and the requirements of the and Modified Ohm's Law provided by [37]. The addition of an external heat source raises the thermal energy within the device, which can be thought of as an increased difficulty for current flow. Consequently, both Ohm's Law equations would suggest a proportional rise in temperature as the device attempts to maintain its operating current under these new thermal conditions.

Standard Ohm's Law (Figure 2(a)) shows a consistent starting temperature distribution across the device, regardless of the applied heat load. This starting temperature appears to range between 0 °C and 20 °C on the Device Temperature (°C) axis. As the ambient temperature increases towards 80 °C, the temperature within the device also rises. The plot for the highest heat load (15 W) shows a temperature increase to around 100 °C on the Device Temperature (°C) axis.

For Modified Ohm's Law (Figure 2(b)), as the ambient temperature increases towards 80 °C, the temperature within the device also rises. However, the starting point for the temperature profiles is noticeably higher compared to the Standard Ohm's Law results. The plot for the lowest heat load (5 W) shows a temperature increase to around 100 °C on the Device Temperature (°C) axis, with all other temperature scenarios exceeding this value. This difference can likely be attributed to the inclusion of the temperature dependence of resistance in the Modified Ohm's Law model, which is not captured by Standard Ohm's Law.

A key distinction between Standard and Modified Ohm's Law lies in how they treat resistance. Standard Ohm's Law assumes a constant resistance value, while Modified Ohm's Law acknowledges that resistance increases as the temperature within the device rises due to the external heat load. This difference is reflected in the results. The Modified Law predicts slightly higher temperatures than the Standard Ohm's Law under similar conditions. As observed in Figure 2(b), the temperature profiles for all three heat loads (5 W, 10 W, and 15 W) on the Device Temperature (°C) axis start at a higher baseline temperature compared to Figure 2(a) for Standard Ohm's Law. Additionally, nearly all three profiles reach a temperature of 100 °C on the Device Temperature (°C) axis at the same ambient temperature (around 80 °C), whereas only the highest heat load (15 W) achieves this temperature in Figure 2(a). This observation further reinforces the notion that Modified Ohm's Law predicts a greater overall temperature rise within the device due to the temperature dependence of resistance. By incorporating this dependence, Modified Ohm's Law predicts a more pronounced temperature rise within the device under increasing external heat loads compared to Standard Ohm's Law. This highlights the importance of considering the non-linear relationship between resistance and temperature for accurate thermal modeling in semiconductor devices.

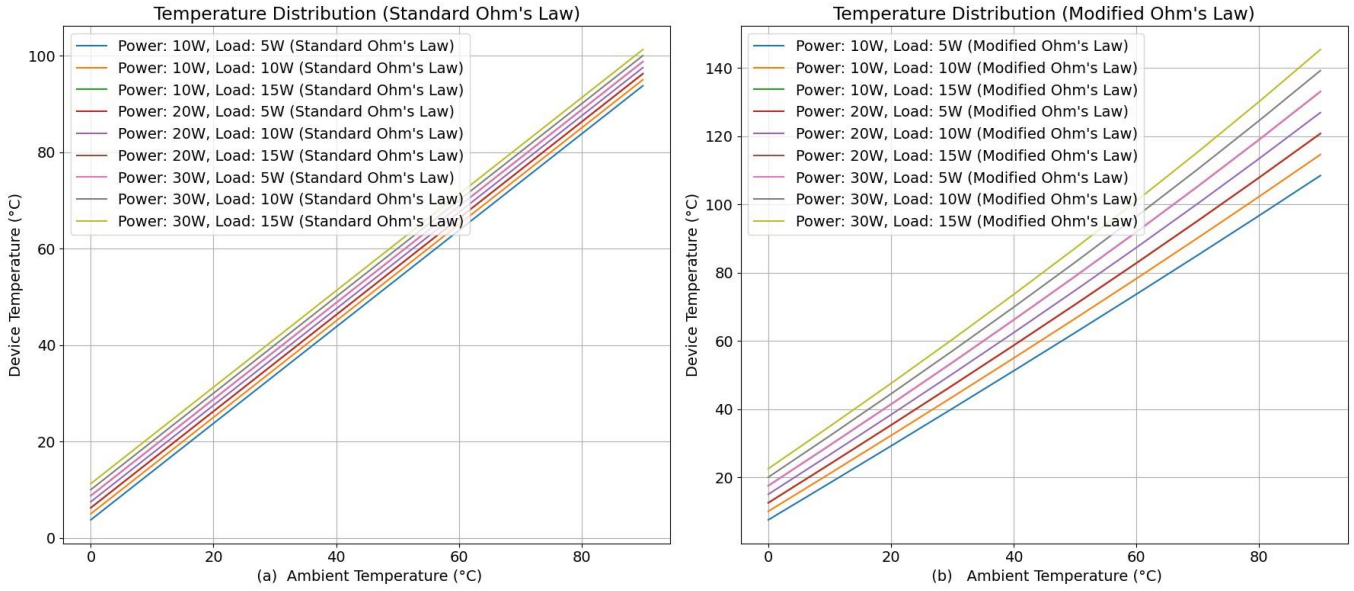

Figure 2. Temperature distribution analysis comparing Standard Ohm's Law (Figure 2(a)) and Modified Ohm's Law (Figure 2(b)) under varying heat loads. (The results illustrate the temperature rise within the semiconductor device as ambient temperature increases, with Modified Ohm's Law (Figure 2(b)) showing higher temperatures due to the incorporation of temperature-dependent resistance).

Validation Remark 2. The simulations demonstrate the importance of considering the temperature dependence of resistance in thermal modeling of semiconductor devices. Standard Ohm's Law assumes a constant resistance, which can lead to underestimating temperature rise within the device, particularly under increasing heat loads. In contrast, the Modified Ohm's Law incorporates this temperature dependence, resulting in a more accurate prediction of the temperature distribution. As observed in the simulations (Figure 1 and Figure 2), the modified Law predicts slightly higher temperatures and a more

pronounced temperature rise compared to the standard approach. This highlights the significance of accounting for the non-linear relationship between resistance and temperature for reliable thermal modeling. By validating the Modified Ohm's Law for this application, we gain a more comprehensive understanding of the thermal behavior in semiconductor devices. This knowledge is crucial for designing efficient cooling strategies to manage heat buildup and ensure optimal device operation.

4.1.3 Cooling Strategies and Thermal Performance Optimization

The primary objective of this section is to investigate and analyze different cooling strategies for semiconductor devices to optimize their temperature under varying ambient conditions. Specifically, the study aims to explore the effectiveness of different heat sink configurations and thermal interface materials in dissipating heat from the semiconductor device. Additionally, the study seeks to compare the thermal performance of the device using both the Finite Element Method (FEM) and standard/Modified Ohm's Law approaches to provide comprehensive insights into the effectiveness of each cooling strategy. Various parameters and configurations were defined to set the stage for the simulation. These include the ambient temperature range, representing the spectrum of environmental conditions under which the semiconductor device operates. Additionally, different heat sink configurations and thermal interface materials were identified to assess their impact on heat dissipation. Constants related to the semiconductor device, such as its physical dimensions (length, width) and thermal properties (thermal conductivity, thermal resistances), were also defined to establish the baseline for the simulations. The simulation process utilized the Finite Element Method (FEM) to simulate cooling strategy optimization. This function calculated the device temperature for various combinations of heat sink configurations and thermal interface materials. Through systematically iterating through different scenarios, the simulation provided a comprehensive understanding of how different cooling strategies influence device temperature under varying ambient conditions. Following the simulation, the obtained results are as depicted in Figure 3, which illustrates the device cooling temperature profiles for both standard and Modified Ohm's Laws using FEM. The results demonstrate how device temperature varies with ambient temperature for each cooling strategy between the Standard Ohm's Law application and the Modified Ohm's Law application.

Analysis of Device Temperature Profiles. The analysis of device temperature profiles for Standard and Modified Ohm's Laws provides valuable insights into the thermal behavior of semiconductor devices under varying ambient conditions. In Figure 3, the device temperature profiles for both Standard and Modified Ohm's Laws are depicted, offering a comparative view of their effectiveness in modeling heat dissipation.

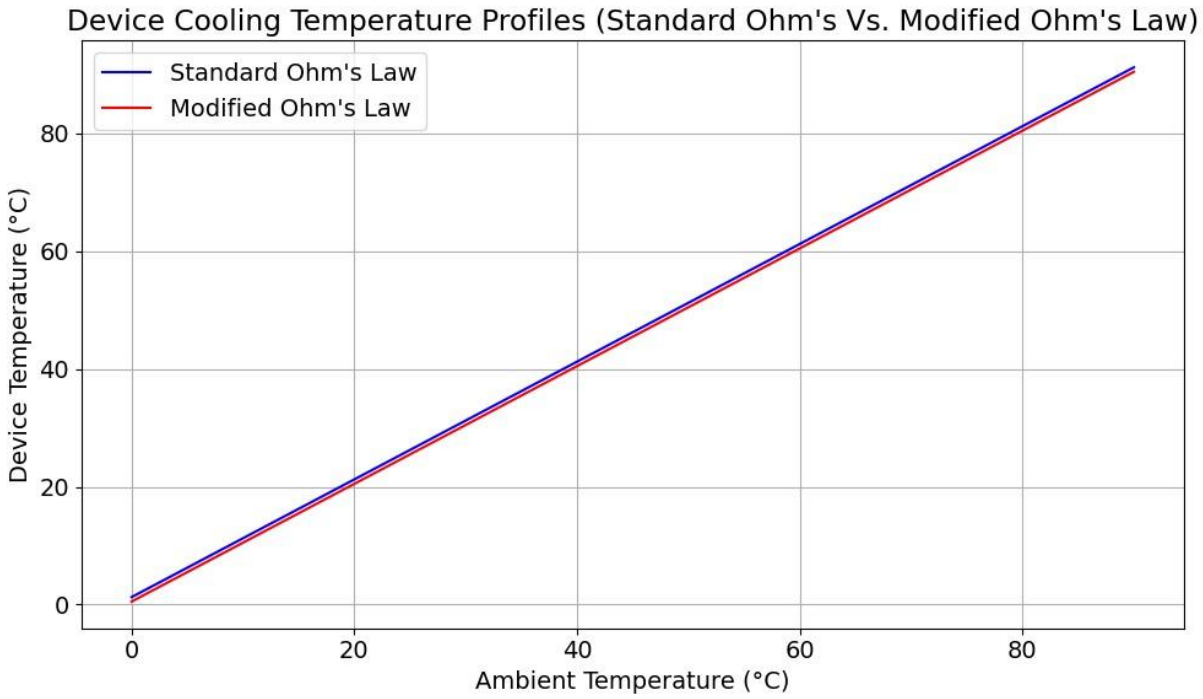

Figure 3. Device temperature profiles for Standard and Modified Ohm's Laws. (The Standard Ohm's Law (blue) line shows a linear increase in device temperature with rising ambient temperature, while the Modified Ohm's Law (red) line demonstrates a non-linear relationship with a steeper slope at lower temperatures and a more gradual increase at higher temperatures).

The Standard Ohm's Law analysis exhibits a linear increase in device temperature with rising ambient temperature. This linear relationship suggests a constant proportionality between the two variables, which deviates from the actual behavior observed in semiconductor devices. In reality, as the ambient temperature increases, the rate of heat transfer from the device to the environment also increases. However, this trend is not accurately captured by the Standard Ohm's Law line. Conversely, the Modified Ohm's Law demonstrates a non-linear relationship between device temperature and ambient temperature. It begins with a steeper slope at lower temperatures, indicating more rapid heat dissipation, and then transitions to a more gradual increase in a linear fashion at higher temperatures. This non-linear behavior better reflects the actual characteristics of semiconductor devices, where heat dissipation becomes more efficient at higher temperatures due to factors such as increased convection. Assuming zero temperature as the reference point, both the standard and Modified Ohm's Law curves approach zero temperature as the ambient temperature approaches zero. This observation suggests that the Modified Ohm's Law model is capable of predicting very low device temperatures, aligning with real-world scenarios. Moreover, in Appendix III, Figure 10 offers additional insights by delineating the temperature prediction differences or margins between standard and Modified Ohm's Laws. This result elucidates any discrepancies or advantages associated with each cooling strategy, facilitating the selection of the most suitable approach for optimizing device temperature and enhancing clarity in decision-making processes.

Cooling Strategy Optimization Using Standard and Modified Ohm's Laws. This section provides the analysis of the cooling strategy optimization for semiconductor devices based on both the Standard Ohm's Law and the Modified Ohm's Law, as illustrated in Figures 4(a) and 4(b) respectively. The visualization of device temperature profiles in Figure 4(a) under the framework of Standard Ohm's Law reveals critical insights into cooling strategy optimization. The results demonstrates the substantial impact of cooling components, showcasing how different heat sink configurations and thermal interface materials influence device temperature. Notably, configurations featuring larger heat sinks or more thermally conductive interface materials tend to result in lower device temperatures, emphasizing the efficacy of these strategies in dissipating heat and maintaining optimal operating conditions. Moreover, the results highlights the temperature sensitivity of semiconductor devices to ambient temperature fluctuations, underscoring the necessity for effective cooling solutions, particularly in environments with elevated ambient temperatures. In contrast, Figure 4(b) presents the device temperature profiles under the Modified Ohm's Law, which introduces adjustments to the calculation of device temperature. The curves in Figure 4(b) exhibit a more non-linear behavior compared to the linear trends observed in Figure 4(a), indicating that the Modified Ohm's Law accounts for factors influencing heat transfer in a more nuanced manner. These non-linear trends, attributed to specific mathematical relationships, capture phenomena such as increased heat dissipation efficiency at higher temperatures, which are not encompassed by the Standard Ohm's Law. Consequently, the Modified Ohm's Law provides more accurate predictions of device temperature, particularly at higher ambient temperatures, enhancing the efficacy of cooling system design and ensuring devices operate within safe temperature thresholds under real-world conditions.

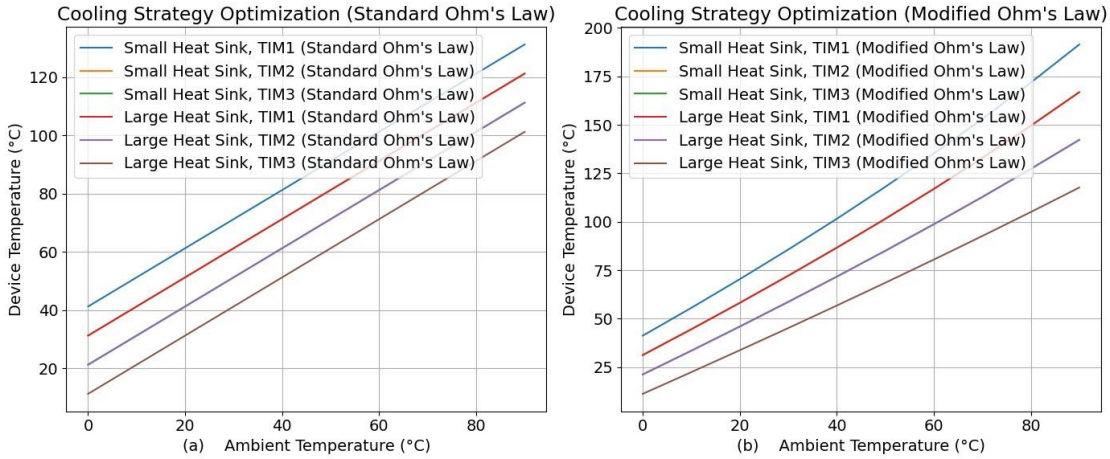

Figure 4. Cooling Strategy Optimization for Semiconductor Devices. (Figure (a)-Device temperature profiles for various heat sink configurations and thermal interface materials under Standard Ohm's Law. The results illustrates the impact of cooling components on device temperature, highlighting the sensitivity to ambient temperature fluctuations and the identification of optimal cooling strategies. Figure (b)-Device temperature profiles under Modified Ohm's Law, showing slight adjustments in temperature predictions compared to Standard Ohm's Law. The non-linear behavior of curves indicates sabtal factors influencing heat transfer, leading to more accurate temperature predictions, particularly at higher ambient temperatures).

Comparing the results between Figures 4(a) and 4(b), we can evaluate the efficacy of the modification introduced in Ohm's Law. This evaluation involves assessing how well the Modified Ohm's Law captures the device temperature behavior under different cooling conditions and ambient temperatures. The observed disparities in temperature trends underscore the potential advantages conferred by the Modified Ohm's Law for cooling strategy optimization, particularly in scenarios characterized by higher ambient temperatures.

Validation Remark 3. Based on the analysis, the Modified Ohm's Law emerges as the most suitable choice for the application of optimizing cooling strategies for semiconductor devices. The introduction of adjustments in the calculation of device temperature within the Modified Ohm's Law leads to more accurate predictions, particularly in scenarios characterized by higher ambient temperatures. The Modified Ohm's Law offers superior efficacy and reliability compared to the Standard Ohm's Law, making it the preferred choice for optimizing cooling strategies for semiconductor devices.

4.1.4 The Impact of Thermal Interface Materials (TIMs) on Heat Dissipation

This section presents an investigation into the impact of Thermal Interface Materials (TIMs) on the effectiveness of heat dissipation, focusing on varying TIM properties between the device and the heat sink. TIM properties significantly influence the thermal conductivity at the interface, thereby affecting heat transfer efficiency.

Effectiveness of Heat Sink Cooling Configuration. The investigation delves into the effectiveness of heat sink cooling configuration in light of Thermal Interface Materials (TIMs), with a specific focus on the variability of TIM properties between the device and the heat sink. Analysis of the data presented in Figure 5 reveals insights into the modeling of the cooling strategy within this context, shedding light on the suitability of the Modified Ohm's Law compared to the Standard Ohm's Law. Figure 5 underscores the pivotal role of TIM thermal conductivity in governing the heat transfer rate between the device and the heat sink. Notably, higher thermal conductivity materials correlate with lower device temperatures, while lower conductivity materials correspond to higher temperatures. This observation accentuates the significance of TIM properties in modulating the efficiency of heat dissipation mechanisms within the cooling configuration. Moreover, Figure 5 visually confirms the non-linear relationship between device current and ambient temperature, elucidating the influence of TIM properties on this dynamic. Each curve depicted in the results, representing different power densities, exhibits a non-linear increase in device current with escalating ambient temperature. This non-linearity arises from the enhanced heat dissipation observed at elevated temperatures, a phenomenon inadequately captured by the Standard Ohm's Law due to its inherent assumption of a linear current-voltage relationship.

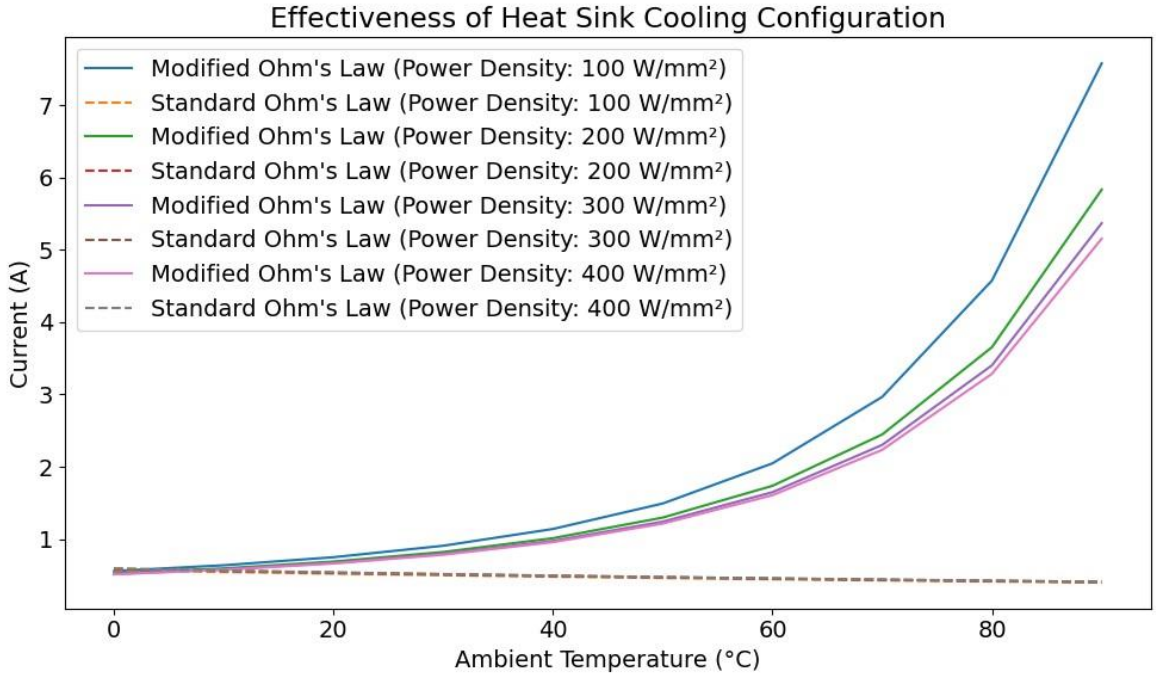

Figure 5. Assessment of Thermal Interface Material (TIM) Properties in Evaluating Heat Sink Cooling Configurations

The limitations of the Standard Ohm's Law become apparent within this context, as it fails to accurately model the observed non-linear trend in Figure 5. The Standard Ohm's Law's assumption of linearity between current and voltage results in a straight line representation in a current-temperature graph, which contradicts the non-linear behavior observed in the data. This discrepancy underscores the inadequacy of the Standard Ohm's Law in capturing the thermal dynamics influenced by TIM properties effectively. Conversely, the Modified Ohm's Law demonstrates greater adaptability to accommodate the non-linear heat transfer characteristics evident in Figure 5. By incorporating additional terms or equations that consider factors such as temperature-dependent thermal conductivity, the Modified Ohm's Law offers a more fitting framework for modeling the thermal behavior within the depicted cooling configuration. In scenarios where TIM properties exert a substantial influence on heat dissipation dynamics, as evidenced in Figure 5, the Modified Ohm's Law emerges as a more suitable choice for accurately representing the thermal phenomena at play.

Effectiveness of Fun Cooling Configuration. The analysis offers an in-depth examination of the impact of Thermal Interface Materials (TIMs) on heat dissipation effectiveness, with a specific focus on the variation in TIM properties between the device and the heat sink. Figure 6 underscores the substantial influence of TIM thermal conductivity on the heat transfer rate between the device and the heat sink. It elucidates that higher thermal conductivity materials result in lower device temperatures and correspondingly lower current, while lower conductivity materials lead to higher temperatures and higher current. This observation emphasizes the critical role of TIM properties in shaping the thermal behavior of the system. Moreover, Figure 6 depicts distinct thermal impedance characteristics, indicating a non-linear relationship between current and ambient temperature. This non-linearity arises from the improved heat dissipation observed at higher temperatures, a phenomenon not adequately captured by the Standard Ohm's Law. The limitations of the Standard Ohm's Law are highlighted within this context, as it assumes a linear relationship between current and voltage, resulting in a straight line representation in a current-temperature graph. However, the absence of such linear behavior in Figure 6 indicates a mismatch between the assumptions of the Standard Ohm's Law and the observed thermal behavior. Conversely, the Modified Ohm's Law can accommodate the non-linear heat transfer characteristics by integrating additional terms or equations that consider factors like temperature-dependent thermal conductivity. This flexibility enables the Modified Ohm's Law to provide a more accurate and comprehensive representation of the thermal behavior depicted in Figure 6.

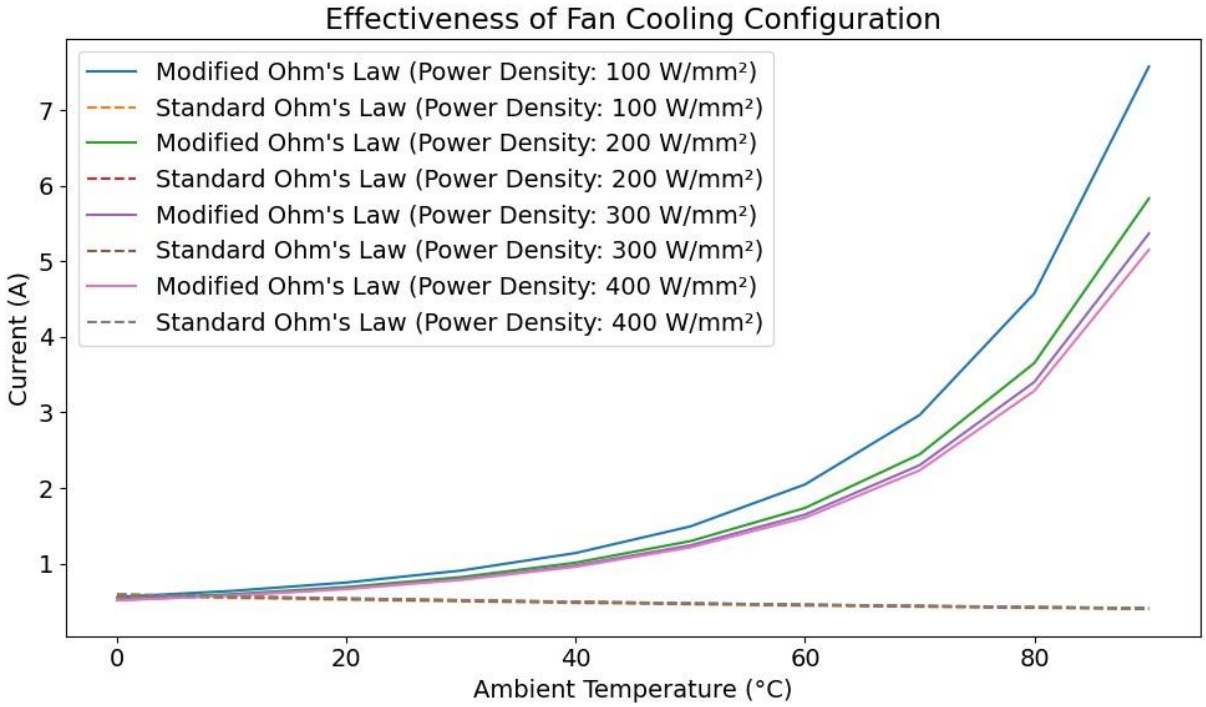

Figure 6. Relationship between current and ambient temperature for varying Thermal Interface Material (TIM) properties under different cooling configurations.

Thermal Interface Materials (TIMs) Impact on Heat Dissipation Effectiveness. This analysis sheds light on the critical role of Thermal Interface Materials (TIMs) in heat dissipation from high-power semiconductor devices. The focus lies on how variations in TIM properties between the device and the heat sink can significantly impact overall thermal performance. Figure 7 depicts a key finding-the thermal conductivity of the TIM directly affects the thermal resistance between the device and the heat sink. This resistance, in turn, influences the current flow within the system, as evident in the plotted relationship between current and ambient temperature for various TIM properties. The non-linear nature of these curves emphasizes the dynamic behavior of heat dissipation processes. Each curve exhibits a gradual increase in current at lower temperatures, followed by a steeper rise at higher temperatures. This observed non-linearity aligns closely with the predictions of the Modified Ohm's Law. The limitations of the Standard Ohm's Law become apparent in this context. It assumes a linear relationship between current and voltage, which contradicts the non-linear trends observed in Figure 7. Conversely, the Modified Ohm's Law incorporates factors like temperature-dependent thermal resistance, allowing it to account for these non-linear relationships. This adaptability makes it a more suitable choice for accurately modeling the complex thermal dynamics depicted in the figure. The visual confirmation provided by Figure 7 further reinforces the explanation. TIMs with higher thermal conductivity exhibit smaller changes in current across the temperature range. This indicates lower thermal resistance and more effective heat dissipation. Conversely, TIMs with lower thermal conductivity result in larger current variations, signifying higher thermal resistance and less efficient heat transfer. Following these results, the non-linear relationship observed in Figure 7 strongly suggests that the Modified Ohm's Law offers a more accurate representation of thermal behavior in this application compared to the standard approach. Its ability to account for temperature-dependent variations, particularly those influenced by varying TIM properties, makes it well-suited for modeling complex thermal environments in high-power semiconductor devices.

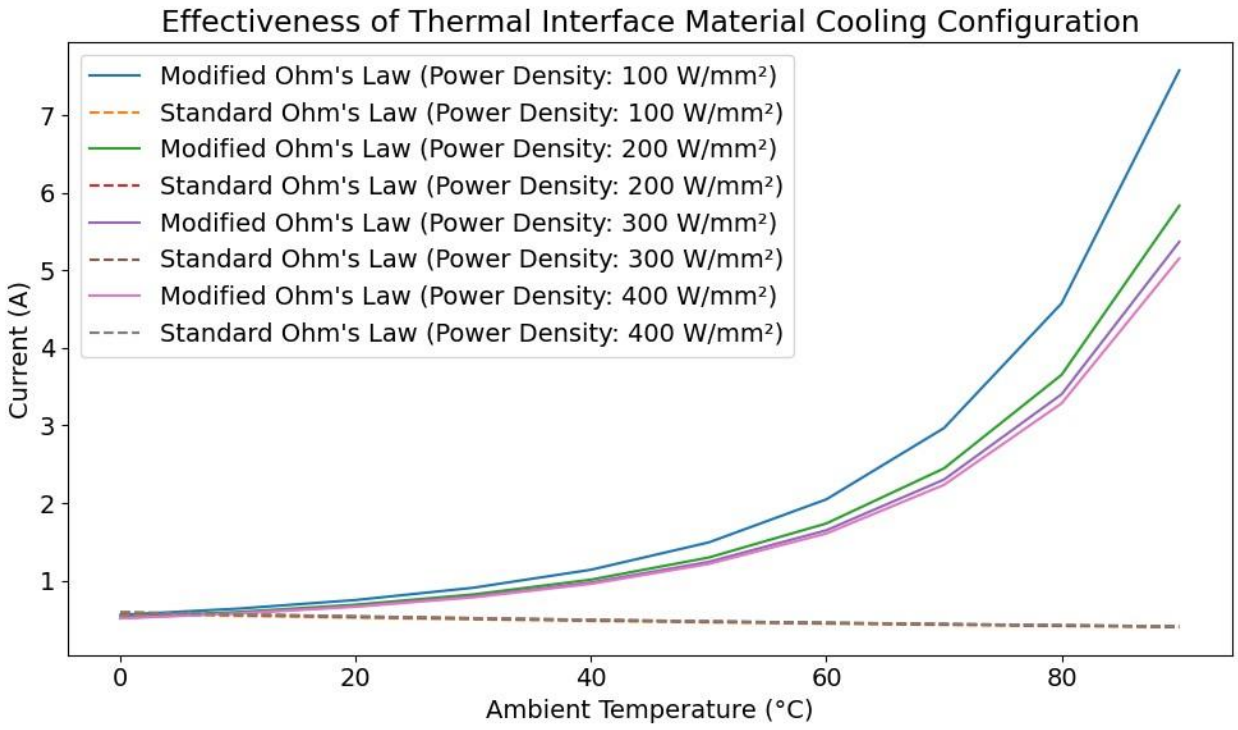

Figure 7. Thermal Interface Materials (TIMs) Impact on Heat Dissipation Effectiveness. (The figure shows that higher thermal conductivity TIMs result in smaller changes in current, indicating more effective heat dissipation, while lower thermal conductivity TIMs lead to larger current variations, reflecting higher thermal resistance and less efficient heat dissipation. The non-linear trends observed underscore the necessity of utilizing a Modified Ohm's Law framework for accurate modeling in scenarios influenced by varying TIM properties.)

Validation Remark 4. Through this analysis, it is evident that the Modified Ohm's Law offers a more suitable framework for accurately modeling the thermal behavior influenced by varying Thermal Interface Materials (TIMs) properties. The non-linear trends observed in the analysis, particularly in Figures 5,6 and 7, highlight the inadequacy of the Standard Ohm's Law, which assumes a linear relationship between current and voltage. In contrast, the Modified Ohm's Law, by incorporating temperature-dependent variations in resistance, better captures the complex interplay between thermal effects and electrical behavior, offering enhanced predictive capabilities in scenarios where TIM properties significantly impact heat dissipation

effectiveness. Therefore, for this specific application, the Modified Ohm's Law emerges as the preferred choice for modeling heat dissipation dynamics.

4.1.5 Validation and Comparative Analysis of Standard and Modified Ohm's Law Models

To validate the practical suitability of the Modified Ohm's Law against the Standard Ohm's Law, we conducted a thorough analysis using synthetic experimental simulation data generation and fitting both models on this dataset. This involved employing Finite Element Method (FEM) for computing temperature distributions, followed by calculating prediction error margins between the two models and the generated synthetic experimental data.

Comparative Analysis of Standard and Modified Ohm's Law Predictions. In this section, we examine the predictions of Standard and Modified Ohm's Law models in comparison with experimental data. Figure 8(a) portrays the prediction of Standard Ohm's Law (blue line) against the experimental data (green line), while Figure 8(b) illustrates the prediction of Modified Ohm's Law (red line) against the same experimental data. Analyzing both figures allows us to discern nuanced differences in how each model aligns with the experimental results. Both Standard and Modified Ohm's Law models appear to capture the overall trend of the experimental data, as indicated by the similarity in the shapes of the curves (green and blue/red lines) in both figures. This suggests that both models predict a comparable relationship between the independent variable (likely voltage or current) and the dependent variable (resistance or temperature). However, deviations from the experimental data are evident in both models. These discrepancies are particularly noticeable in regions where the experimental data exhibits sharp variations or steeper slopes. In Figure 8(a), the prediction of Standard Ohm's Law (blue line) demonstrates a slightly larger deviation from the experimental data (green line) compared to the Modified Ohm's Law in Figure 8(b). This disparity is especially apparent in regions with steeper slopes or sharp changes. The blue line appears smoother and less responsive to these rapid variations in the experimental data. Conversely, the prediction by Modified Ohm's Law (red line) in Figure 8(b) seems to better capture the sharp variations observed in the experimental data (green line). The red line more closely follows the steeper slopes and trends of the green line, indicating a stronger correlation between the model and the experimental observations. These discrepancies between the predictions and the experimental data may stem from the inherent limitations of each model. Standard Ohm's Law assumes a constant linear relationship between voltage and current, which might not hold true for real-world materials, especially at higher temperatures or voltage ranges. This non-linearity could explain why the Standard Ohm's Law prediction deviates more from the experimental data, particularly in regions with steeper slopes.

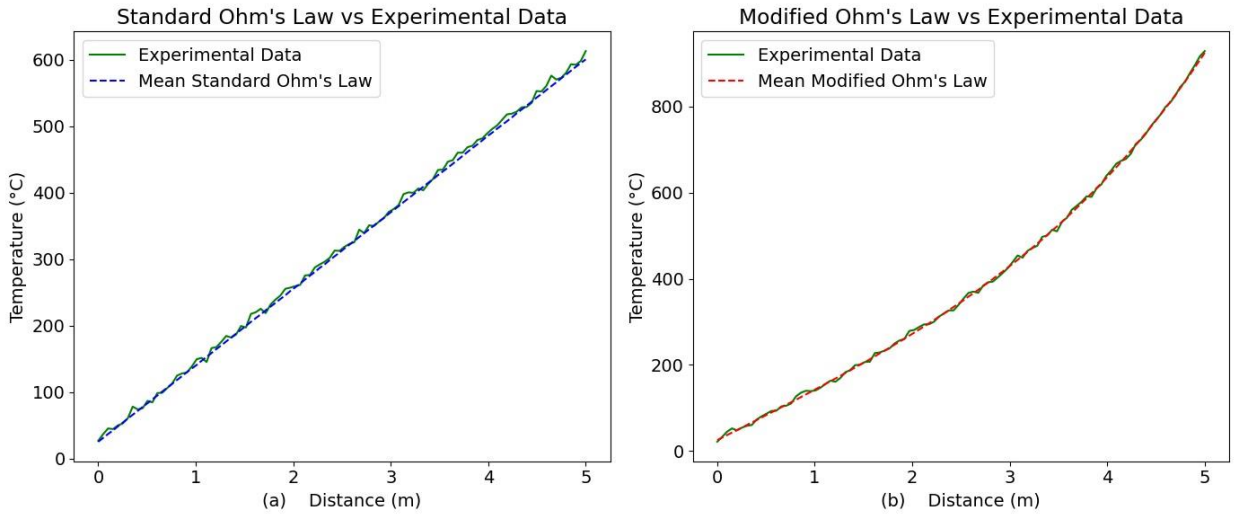

Figure 8. Comparison of model predictions with experimental data. (The blue line in Figure 8(a) represents the Standard Ohm's Law prediction, while the red line in Figure 8(b) shows the prediction from the Modified Ohm's Law. Both plots are overlaid with the experimental data represented by the green line. This allows for a direct comparison of the predicted temperature profiles with the actual measurements along the device (denoted by Distance (m)) and across the temperature range (indicated by Temperature (°C))).

On the other hand, Modified Ohm's Law incorporates the temperature dependence of resistance or other non-idealities, potentially providing a more accurate representation of the physical phenomena at play. This could elucidate why the Modified Ohm's Law prediction (red line) in Figure 8(b) demonstrates better alignment with the experimental data (green line), especially in areas with rapid changes. In the essence, the analysis of Figure 8(a) and Figure 8(b) suggests that both Standard and Modified Ohm's Law models can predict the general trend of the experimental data. However, Modified Ohm's Law appears to offer a more accurate representation, particularly in capturing the variations observed in the experimental results. This result highlights the importance of considering non-linear relationships and material properties when modeling real-world systems for improved accuracy.

Error Distribution Analysis and Comparison of Standard and Modified Ohm's Laws. The analysis is aimed at comparing the prediction accuracies of Standard and Modified Ohm's Laws in the context of temperature prediction based on simulated experimental data. In Figure 9, the distribution of prediction errors for both models is illustrated. Here, the horizontal axis represents the absolute error (°C), indicating the disparity between the predicted temperature values and the actual experimental temperatures. The vertical axis denotes the probability density, reflecting the likelihood of encountering specific error values. Upon examination of the error distributions depicted by the blue and red lines, insights into the prediction accuracies of each model emerge. The broader spread of the blue line associated with Standard Ohm's Law suggests a wider range of error values, indicating a higher probability of encountering larger deviations from the actual experimental temperatures. Conversely, the narrower distribution represented by the red line corresponding to Modified Ohm's Law implies that prediction errors are concentrated within a smaller range, suggesting a higher likelihood of predictions being closer to the actual temperatures. The observation of marginally smaller errors for Modified Ohm's Law aligns with the analysis of the error distributions. The reduced spread of errors, clustered closer to zero on the error index with device distance (m), indicates a higher degree of accuracy in temperature prediction compared to Standard Ohm's Law. This difference underscores the potential advantages of employing the Modified Ohm's Law over its standard counterpart in practical applications where precise temperature predictions are pivotal. The comparison drawn from Figure 9 suggests that Modified Ohm's Law offers slightly superior prediction accuracy compared to Standard Ohm's Law when applied to temperature prediction tasks based on simulated experimental data. While both models yield reasonable predictions, the narrower error distribution observed with Modified Ohm's Law signifies a closer alignment with the experimental data. This finding underscores the significance of utilizing more complex models, such as Modified Ohm's Law, to enhance temperature prediction accuracy, particularly in critical engineering applications where even minor temperature fluctuations can have substantial implications on performance and reliability.

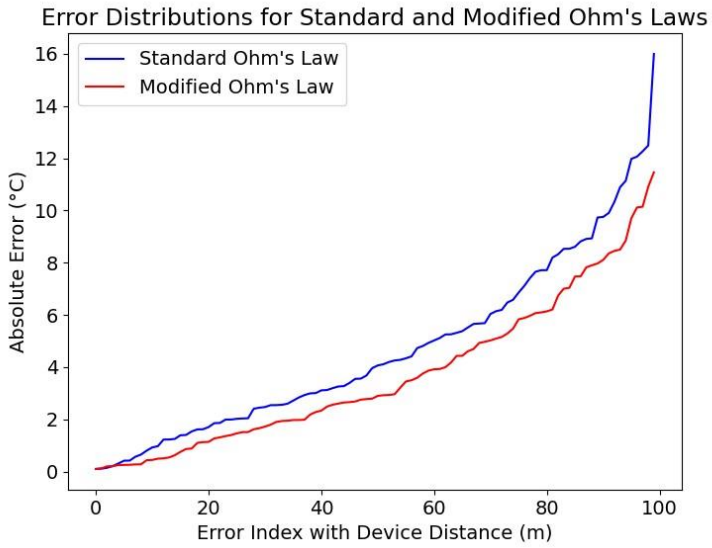

Figure 9. Error distributions for Standard and Modified Ohm's Law compared against synthetic experimental data. (These results illustrates the distribution of prediction errors for both Standard (blue line) and Modified (red line) Ohm's Laws compared against synthetic experimental data (likely temperature values). The horizontal axis represents the error index with device distance (m), which implies the spatial position within the thermal device where the errors occur. The vertical axis denotes the absolute error (°C), indicating the magnitude of deviation between the predicted and actual temperatures).

Remark on Long Device Distances in Analysis (Scaling for Simulation). The application of long device distances, such as 100 meters, within the analysis serves as a scaling factor within the simulation framework rather than representing physical dimensions of a semiconductor device. This abstraction allows for the exploration of temperature distributions and thermal behavior at a macroscopic level, enabling insights into system-level performance and thermal management strategies. While the distances utilized may appear large in the context of semiconductor devices, they facilitate comprehensive analysis and understanding of thermal phenomena across extended spatial domains within the simulation environment.

5. DİSCUSSİON

The results of simulated experiments provide compelling evidence for the effectiveness of the Modified Ohm's Law in addressing thermal management challenges in high-power semiconductor devices. This section delves into a detailed analysis, comparing it with the Standard Ohm's Law, to elucidate the strengths of the modified approach in thermal simulations. It also explores the significance of the validation process in understanding thermal behavior and its implications for optimizing cooling strategies.

5.1 Strengths of the Modified Ohm's Law in Thermal Simulations

The Modified Ohm's Law offers several advantages over the Standard Ohm's Law for simulating the intricate thermal dynamics of high-power semiconductor devices. A key strength lies in its ability to capture the non-linear relationships between temperature (T), current (I), and resistance (R). Unlike the Standard Ohm's Law, which assumes a linear proportionality ($I = V/R$), the modified version incorporates an exponential term to account for temperature-dependent variations in resistance $\left(I_{modified} = a \times e^{\frac{R_{short}}{R_0}}\right)$, [37]. This formulation aligns with the physics of semiconductor materials, where resistance increases with rising temperature due to lattice vibrations and carrier scattering [65,66]. This enhanced accuracy in predicting device temperature under varying operating conditions is crucial for optimizing cooling strategies and ensuring the reliability and longevity of semiconductor devices in real-world applications. Furthermore, the Modified Ohm's Law provides a more comprehensive framework for modeling heat dissipation mechanisms. By incorporating additional terms or equations that account for factors such as thermal conductivity (k) and thermal resistance (R_{th}) in practice, the modified approach offers a more nuanced understanding of the thermal behavior of semiconductor devices.

5.2 Validation Process Strengthens Understanding of Thermal Behavior

The comparison of predictions from standard and Modified Ohm's Law models with experimental data serves a critical role. This process validates the accuracy of simulation techniques employed by engineers and exposes areas for improvement. In our study, this comparison revealed the Modified Ohm's Law's consistent advantage over the standard approach in predicting device temperature, especially in regions with rapid thermal variations. This validation not only bolsters confidence in the Modified Ohm's Law model but also offers valuable insights into the fundamental thermal dynamics of semiconductor devices. Beyond theoretical validation, the process facilitates the refinement of simulation parameters and model assumptions to better reflect real-world conditions. Key parameters in the Modified Ohm's Law, such as R_{short} (representing variable resistance) and a (current scaling factor), can be adjusted based on experimental data to improve the accuracy and reliability of thermal simulations. This iterative approach leads to more informed decision-making in device design and optimization. The reference resistance (R_0) in the Modified Ohm's Law can also be calibrated to match the specific characteristics of the semiconductor device being modeled.

5.3 Implications for Optimizing Cooling Strategies

The Modified Ohm's Law's implications extend beyond theoretical modeling. It impacts practical applications by improving cooling strategies for high-power semiconductor devices. Analysis demonstrates that this modified approach offers superior accuracy and predictive capabilities compared to the Standard Ohm's Law, particularly in scenarios influenced by factors such as thermal interface materials (TIMs) and heat sink configurations. TIMs with varying thermal conductivities can significantly impact heat transfer efficiency between the device and the heat sink. The Modified Ohm's Law has demonstrated the ability to account for these variations by incorporating the thermal conductivity of the TIM into the model. Similarly, heat sink configurations with larger surface areas or improved airflow characteristics can enhance heat dissipation. The Modified Ohm's Law has shown the potential that it can be used to predict the effectiveness of different heat sink designs by incorporating their thermal resistance into the model. Thermal simulations based on Modified Ohm's Law provide engineers with valuable insights.

These insights can be used to optimize cooling strategies, mitigate thermal issues, and enhance device performance. For instance, simulations might identify configurations with larger heat sinks or more thermally conductive thermal interface materials (TIMs) that result in lower device temperatures. This information directly translates to the selection of appropriate cooling components, ensuring optimal device operation and preventing thermal runaway scenarios.

6. CONCLUSİON

Throughout the analysis, a modified version of Ohm's Law was applied to address the intricate thermal management challenges encountered in high-power semiconductor devices. Acknowledging the non-linear relationship between temperature, current, and resistance, the paper aimed to establish a more accurate and reliable method for modeling thermal behavior, ultimately enhancing cooling strategies and mitigating thermal issues. The workflow has demonstrated the effectiveness of the Modified Ohm's Law in addressing thermal management challenges inherent in high-power semiconductor devices. This paper presents one of the initial conventional applications of the Modified Ohm's Law within this domain, achieved through scrupulous combination of simulations and empirical validation. Integrating temperature-dependent variations in resistance, the modified approach offers a more refined representation of the complex thermal dynamics within these devices. This advancement not only deepens engineers' understanding but also enhances their predictive capability concerning semiconductor device behavior across various operating conditions, thereby facilitating the development of more effective thermal management strategies. A critical revelation of our analysis lies in the strengths exhibited by the Modified Ohm's Law when compared to the conventional approach. Firstly, the modified version adeptly captures the non-linear relationship between temperature, current, and resistance, resulting in more precise predictions of device temperature, particularly in scenarios characterized by rapid temperature fluctuations. Secondly, by incorporating factors such as thermal conductivity and thermal resistance, the Modified Ohm's Law provides a comprehensive framework for modeling heat dissipation mechanisms. This feature enables researchers and engineers to design cooling systems tailored to specific device configurations and operating environments, thereby enhancing overall efficiency. The validation process served as a cornerstone in solidifying our comprehension of thermal behavior within high-power semiconductor devices. Through rigorous comparisons between model predictions and simulated experimental data validated the modified approach's accuracy and yielded invaluable insights into the underlying thermal dynamics. This iterative process not only bolstered confidence in the Modified Ohm's Law model but also facilitated the refinement of simulation parameters and model assumptions. Consequently, this iterative refinement process enables more informed decision-making during device design and optimization endeavors. Beyond theoretical implications, the findings of this study bear practical significance in optimizing cooling strategies for high-power semiconductor devices. Leveraging insights gleaned from thermal simulations, engineers can identify optimal cooling configurations to mitigate thermal issues and enhance device performance. Notably, the analysis underscored that configurations featuring larger heat sinks or more thermally conductive interface materials tend to yield lower device temperatures. Such insights can guide the selection of appropriate cooling components to ensure optimal device operation and avert thermal-related malfunctions.

SIMILARITY RATE: 5%

AUTHOR CONTRIBUTION

First Author: Conceptualization, methodology, data curation, writing, editing etc.

CONFLICT of INTEREST

The authors declared that they have no known conflict of interest.

REFERENCES

[1] N. Hossain et al., "Advances and significances of nanoparticles in semiconductor applications – A review," Results Eng., vol. 19, p. 101347, Sep. 2023, doi: 10.1016/j.rineng.2023.101347.

[2] B. K. Bose, "Global Energy Scenario and Impact of Power Electronics in 21st Century," IEEE Trans. Ind. Electron., vol. 60, no. 7, pp. 2638–2651, Jul. 2013, doi: 10.1109/TIE.2012.2203771.

[3] R. Singh, S. V. Akram, A. Gehlot, D. Buddhi, N. Priyadarshi, and B. Twala, "Energy System 4.0: Digitalization of the Energy Sector with Inclination towards Sustainability," Sensors, vol. 22, no. 17, p. 6619, Sep. 2022, doi: 10.3390/s22176619.

[4] M. Kumar, K. P. Panda, R. T. Naayagi, R. Thakur, and G. Panda, "Comprehensive Review of Electric Vehicle Technology and Its Impacts: Detailed Investigation of Charging Infrastructure, Power Management, and Control Techniques," Appl. Sci., vol. 13, no. 15, Art. no. 15, Jan. 2023, doi: 10.3390/app13158919.

[5] M. Schulz, "Thermal management details and their influence on the aging of power semiconductors," in 2014 16th European Conference on Power Electronics and Applications, Lappeenranta, Finland: IEEE, Aug. 2014, pp. 1–6. doi: 10.1109/EPE.2014.6910898.

[6] T. Zhan et al., "Effects of Thermal Boundary Resistance on Thermal Management of Gallium-Nitride-Based Semiconductor Devices: A Review," Micromachines, vol. 14, no. 11, p. 2076, Nov. 2023, doi: 10.3390/mi14112076.

[7] Kim, Kwang-Seok, Choi, Don-Hyun, and Jung, Seung-Boo, "Overview on Thermal Management Technology for High Power Device Packaging," J. Microelectron. Packag. Soc., vol. 21, no. 2, pp. 13–21, Jun. 2014, doi: 10.6117/KMEPS.2014.21.2.013.

[8] Thermal and Power Management of Integrated Circuits. in Series on Integrated Circuits and Systems. Boston: Kluwer Academic Publishers, 2006. doi: 10.1007/0-387-29749-9.

[9] V. Bianco, M. De Rosa, and K. Vafai, "Phase-change materials for thermal management of electronic devices," Appl. Therm. Eng., vol. 214, p. 118839, Sep. 2022, doi: 10.1016/j.applthermaleng.2022.118839.

[10] S. Rafin, R. Ahmed, Md. Haque, Md. Hossain, Md. Haque, and O. Mohammed, "Power Electronics Revolutionized: A Comprehensive Analysis of Emerging Wide and Ultrawide Bandgap Devices," Micromachines, vol. 14, no. 11, p. 2045, Oct. 2023, doi: 10.3390/mi14112045.

[11] T. Van Do, J. P. F. Trovão, K. Li, and L. Boulon, "Wide-Bandgap Power Semiconductors for Electric Vehicle Systems: Challenges and Trends," IEEE Veh. Technol. Mag., vol. 16, no. 4, pp. 89–98, Dec. 2021, doi: 10.1109/MVT.2021.3112943.

[12] J. R. Celaya, P. Wysocki, V. Vashchenko, S. Saha, and K. Goebel, "Accelerated aging system for prognostics of power semiconductor devices," in 2010 IEEE AUTOTESTCON, Orlando, FL, USA: IEEE, Sep. 2010, pp. 1–6. doi: 10.1109/AUTEST.2010.5613564.

[13] J. Jaguemont and J. Van Mierlo, "A comprehensive review of future thermal management systems for battery-electrified vehicles," J. Energy Storage, vol. 31, p. 101551, Oct. 2020, doi: 10.1016/j.est.2020.101551.

[14] M. Uzair, G. Abbas, and S. Hosain, "Characteristics of Battery Management Systems of Electric Vehicles with Consideration of the Active and Passive Cell Balancing Process," World Electr. Veh. J., vol. 12, no. 3, p. 120, Aug. 2021, doi: 10.3390/wevj12030120.

[15] S. S. Madani, C. Ziebert, and M. Marzband, "Thermal Behavior Modeling of Lithium-Ion Batteries: A Comprehensive Review," Symmetry, vol. 15, no. 8, p. 1597, Aug. 2023, doi: 10.3390/sym15081597.

[16] K. Gorecki and J. Zarebski, "Nonlinear Compact Thermal Model of Power Semiconductor Devices," IEEE Trans. Compon. Packag. Technol., vol. 33, no. 3, pp. 643–647, Sep. 2010, doi: 10.1109/TCAPT.2010.2052052.

[17] A. M. Darwish, A. J. Bayba, A. Khorshid, A. Rajaie, and H. A. Hung, "Calculation of the Nonlinear Junction Temperature for Semiconductor Devices Using Linear Temperature Values," IEEE Trans. Electron Devices, vol. 59, no. 8, pp. 2123–2128, Aug. 2012, doi: 10.1109/TED.2012.2200040.

[18] M. Janicki, Z. Sarkany, and A. Napieralski, "Impact of nonlinearities on electronic device transient thermal responses," Microelectron. J., vol. 45, no. 12, pp. 1721–1725, Dec. 2014, doi: 10.1016/j.mejo.2014.04.043.

[19] O. Yamashita, "Effect of linear and non-linear components in the temperature dependences of thermoelectric properties on the energy conversion efficiency," Energy Convers. Manag., vol. 50, no. 8, pp. 1968–1975, Aug. 2009, doi: 10.1016/j.enconman.2009.04.019.

[20] J. L. Smoyer and P. M. Norris, "Brief Historical Perspective in Thermal Management and the Shift Toward Management at the Nanoscale," Heat Transf. Eng., vol. 40, no. 3–4, pp. 269–282, Feb. 2019, doi: 10.1080/01457632.2018.1426265.

[21] D. Bandhu, M. D. Khadir, A. Kaushik, S. Sharma, H. A. Ali, and A. Jain, "Innovative Approaches to Thermal Management in Next-Generation Electronics," E3S Web Conf., vol. 430, p. 01139, 2023, doi: 10.1051/e3sconf/202343001139.

[22] Z. He, Y. Yan, and Z. Zhang, "Thermal management and temperature uniformity enhancement of electronic devices by micro heat sinks: A review," Energy, vol. 216, p. 119223, Feb. 2021, doi: 10.1016/j.energy.2020.119223.

[23] N. A. Pambudi, A. Sarifudin, R. A. Firdaus, D. K. Ulfa, I. M. Gandidi, and R. Romadhon, "The immersion cooling technology: Current and future development in energy saving," Alex. Eng. J., vol. 61, no. 12, pp. 9509–9527, Dec. 2022, doi: 10.1016/j.aej.2022.02.059.

[24] M. Ekpu, R. Bhatti, N. Ekere, S. Mallik, E. Amalu, and K. Otiaba, "Investigation of effects of heat sinks on thermal performance of microelectronic package," in 3rd IEEE International Conference on Adaptive Science and Technology (ICAST 2011), Abuja, Nigeria: IEEE, Nov. 2011, pp. 127–132. doi: 10.1109/ICASTech.2011.6145164.

[25] M. C. Shaw et al., "Enhanced thermal management by direct water spray of high-voltage, high power devices in a three-phase, 18-hp AC motor drive demonstration," in ITherm 2002. Eighth Intersociety Conference on Thermal and

Thermomechanical Phenomena in Electronic Systems (Cat. No.02CH37258), San Diego, CA, USA: IEEE, 2002, pp. 1007–1014. doi: 10.1109/ITHERM.2002.1012567.

[26] L. He, H. Jing, Y. Zhang, P. Li, and Z. Gu, "Review of thermal management system for battery electric vehicle," J. Energy Storage, vol. 59, p. 106443, Mar. 2023, doi: 10.1016/j.est.2022.106443.

[27] R. S. Longchamps, X.-G. Yang, and C.-Y. Wang, "Fundamental Insights into Battery Thermal Management and Safety," ACS Energy Lett., vol. 7, no. 3, pp. 1103–1111, Mar. 2022, doi: 10.1021/acsenergylett.2c00077.

[28] W. Wang, X. Zhang, C. Xin, and Z. Rao, "An experimental study on thermal management of lithium ion battery packs using an improved passive method," Appl. Therm. Eng., vol. 134, pp. 163–170, Apr. 2018, doi: 10.1016/j.applthermaleng.2018.02.011.

[29] J. Cho and J. Woo, "Development and experimental study of an independent row-based cooling system for improving thermal performance of a data center," Appl. Therm. Eng., vol. 169, p. 114857, Mar. 2020, doi: 10.1016/j.applthermaleng.2019.114857.

[30] Xingsheng Liu, M. H. Hu, C. G. Caneau, R. Bhat, L. C. Hughes, and Chung-En Zah, "Thermal management strategies for high power semiconductor pump lasers," in The Ninth Intersociety Conference on Thermal and Thermomechanical Phenomena In Electronic Systems (IEEE Cat. No.04CH37543), Las Vegas, NV, USA: IEEE, 2004, pp. 493–500. doi: 10.1109/ITHERM.2004.1318324.

[31] L. Maguire, M. Behnia, and G. Morrison, "An Experimental and Computational Study of Heat Transfer in High Power Amplifiers," Heat Transf. Eng., vol. 26, no. 2, pp. 81–92, Mar. 2005, doi: 10.1080/01457630590897295.

[32] T. Zhang, "Analytical Solution of Nonlinear Thermoelectric Heat Transport Equation Using Homotopy Perturbation Method," J. Comput. Intell. Electron. Syst., vol. 4, no. 1, pp. 59–66, Mar. 2015, doi: 10.1166/jcies.2015.1115.

[33] Z. Hu, M. Cui, and X. Wu, "Real-Time Temperature Prediction of Power Devices Using an Improved Thermal Equivalent Circuit Model and Application in Power Electronics," Micromachines, vol. 15, no. 1, p. 63, Dec. 2023, doi: 10.3390/mi15010063.

[34] A. Ibrahim, M. Salem, M. Kamarol, M. Delgado, and M. K. Mat Desa, "Review of Active Thermal Control for Power Electronics: Potentials, Limitations, and Future Trends," IEEE Open J. Power Electron., vol. 5, pp. 414–435, Apr. 2024, doi: 10.1109/OJPEL.2024.3376086.

[35] M. Baumann, W. Wondrak, and J. Lutz, Insight into thermal management concepts for power electronics modules in automotive application. 2023.

[36] M. Sofwan, M. Z. Abdullah, and M. K. Abdullah, "Experimental study on the cooling performance of high power LED arrays under natural convection," IOP Conf. Ser. Mater. Sci. Eng., vol. 50, Dec. 2013, doi: 10.1088/1757-899X/50/1/012030.

[37] A. Kimuya, "THE MODIFIED OHM'S LAW AND ITS IMPLICATIONS FOR ELECTRICAL CIRCUIT ANALYSIS," Eurasian J. Sci. Eng. Technol., vol. 4, no. 2, pp. 59–70, Dec. 2023, doi: 10.55696/ejset.1373552.

[38] M. Thorsell, K. Andersson, M. Fagerlind, M. Sudow, P.-A. Nilsson, and N. Rorsman, "Thermal Study of the High-Frequency Noise in GaN HEMTs," IEEE Trans. Microw. Theory Tech., vol. 57, no. 1, pp. 19–26, Jan. 2009, doi: 10.1109/TMTT.2008.2009084.

[39] M. Tounsi, A. Oukaour, B. Tala-Ighil, H. Gualous, B. Boudart, and D. Aissani, "Characterization of high-voltage IGBT module degradations under PWM power cycling test at high ambient temperature," Microelectron. Reliab., vol. 50, no. 9–11, pp. 1810–1814, Sep. 2010, doi: 10.1016/j.microrel.2010.07.059.

[40] W.-H. Chi, T.-L. Chou, C.-N. Han, and K.-N. Chiang, "Analysis of Thermal Performance of High Power Light Emitting Diodes Package," in 2008 10th Electronics Packaging Technology Conference, Singapore, Singapore: IEEE, Dec. 2008, pp. 533–538. doi: 10.1109/EPTC.2008.4763488.

[41] Z. Zhang, X. Wang, and Y. Yan, "A review of the state-of-the-art in electronic cooling," E-Prime - Adv. Electr. Eng. Electron. Energy, vol. 1, p. 100009, 2021, doi: 10.1016/j.prime.2021.100009.

[42] S. Rashidi, N. Karimi, B. Sunden, K. C. Kim, A. G. Olabi, and O. Mahian, "Progress and challenges on the thermal management of electrochemical energy conversion and storage technologies: Fuel cells, electrolysers, and supercapacitors," Prog. Energy Combust. Sci., vol. 88, p. 100966, Jan. 2022, doi: 10.1016/j.pecs.2021.100966.

[43] B. Kumanek and D. Janas, "Thermal conductivity of carbon nanotube networks: a review," J. Mater. Sci., vol. 54, no. 10, pp. 7397–7427, May 2019, doi: 10.1007/s10853-019-03368-0.

[44] W. Yu, C. Liu, and S. Fan, "Advances of CNT-based systems in thermal management," Nano Res., vol. 14, no. 8, pp. 2471–2490, Aug. 2021, doi: 10.1007/s12274-020-3255-1.

[45] S. Huang et al., The effects of graphene-based films as heat spreaders for thermal management in electronic packaging. 2016, p. 892. doi: 10.1109/ICEPT.2016.7583272.

[46] P. Huang et al., "Graphene film for thermal management: A review," Nano Mater. Sci., vol. 3, Sep. 2020, doi: 10.1016/j.nanoms.2020.09.001.

[47] Q. Chen et al., "Recent advances in thermal-conductive insulating polymer composites with various fillers," Compos. Part Appl. Sci. Manuf., vol. 178, p. 107998, Mar. 2024, doi: 10.1016/j.compositesa.2023.107998.

[48] Y.-H. Zhao, Y.-F. Zhang, and S.-L. Bai, "High thermal conductivity of flexible polymer composites due to synergistic effect of multilayer graphene flakes and graphene foam," Compos. Part Appl. Sci. Manuf., vol. 85, pp. 148–155, Jun. 2016, doi: 10.1016/j.compositesa.2016.03.021.
[49] Z. Sun, J. W. Chew, N. J. Hills, K. N. Volkov, and C. J. Barnes, "Efficient FEA/CFD Thermal Coupling for Engineering Applications," in Volume 4: Heat Transfer, Parts A and B, Berlin, Germany: ASMEDC, Jan. 2008, pp. 1505–1515. doi: 10.1115/GT2008-50638.
[50] Z. Sun, J. W. Chew, N. J. Hills, K. N. Volkov, and C. J. Barnes, "Efficient Finite Element Analysis/Computational Fluid Dynamics Thermal Coupling for Engineering Applications," J. Turbomach., vol. 132, no. 3, p. 031016, Jul. 2010, doi: 10.1115/1.3147105.
[51] L. Yuan, S. Liu, M. Chen, and X. Luo, "Thermal Analysis of High Power LED Array Packaging with Microchannel Cooler," in 2006 7th International Conference on Electronic Packaging Technology, Shanghai, China: IEEE, Aug. 2006, pp. 1–5. doi: 10.1109/ICEPT.2006.359826.
[52] S. Kochupurackal Rajan, B. Ramakrishnan, H. Alissa, W. Kim, C. Belady, and M. Bakir, "Integrated Silicon Microfluidic Cooling of a High-Power Overclocked CPU for Efficient Thermal Management," IEEE Access, vol. 10, pp. 1–1, Jan. 2022, doi: 10.1109/ACCESS.2022.3179387.
[53] A. Usman, F. Xiong, W. Aftab, M. Qin, and R. Zou, "Emerging Solid-to-Solid Phase-Change Materials for Thermal-Energy Harvesting, Storage, and Utilization," Adv. Mater., vol. 34, no. 41, p. 2202457, Oct. 2022, doi: 10.1002/adma.202202457.
[54] K. Venkateswarlu and K. Ramakrishna, "Recent advances in phase change materials for thermal energy storage-a review," J. Braz. Soc. Mech. Sci. Eng., vol. 44, no. 1, p. 6, Jan. 2022, doi: 10.1007/s40430-021-03308-7.
[55] Z.-Q. Yu, M.-T. Li, and B.-Y. Cao, "A comprehensive review on microchannel heat sinks for electronics cooling," Int. J. Extreme Manuf., vol. 6, no. 2, p. 022005, Apr. 2024, doi: 10.1088/2631-7990/ad12d4.
[56] A. Bar-Cohen, J. J. Maurer, and A. Sivananthan, "Near-Junction Microfluidic Cooling for Wide Bandgap Devices," MRS Adv., vol. 1, no. 2, pp. 181–195, Jan. 2016, doi: 10.1557/adv.2016.120.
[57] M. I. Davidzon, "Newton's law of cooling and its interpretation," Int. J. Heat Mass Transf., vol. 55, no. 21–22, pp. 5397–5402, Oct. 2012, doi: 10.1016/j.ijheatmasstransfer.2012.03.035.
[58] H.-P. Hsu, T.-W. Tu, and J.-R. Chang, "An Analytic Solution for 2D Heat Conduction Problems with General Dirichlet Boundary Conditions," Axioms, vol. 12, no. 5, p. 416, Apr. 2023, doi: 10.3390/axioms12050416.
[59] G. Feltrin, "Dirichlet Boundary Conditions," in Positive Solutions to Indefinite Problems, in Frontiers in Mathematics. , Cham: Springer International Publishing, 2018, pp. 3–37. doi: 10.1007/978-3-319-94238-4_1.
[60] B. N. Biswas, S. Chatterjee, S. Mukherjee, and S. Pal, "A DISCUSSION ON EULER METHOD: A REVIEW," Electron. J. Math. Anal. Appl., vol. 1, pp. 294–317, Jun. 2013.
[61] J. Liu and Y. Hao, "Crank–Nicolson method for solving uncertain heat equation," Soft Comput., vol. 26, no. 3, pp. 937–945, Feb. 2022, doi: 10.1007/s00500-021-06565-9.
[62] E. Hairer and G. Wanner, "Stiff differential equations solved by Radau methods," J. Comput. Appl. Math., vol. 111, no. 1–2, pp. 93–111, Nov. 1999, doi: 10.1016/S0377-0427(99)00134-X.
[63] C. Milici, J. Tenreiro Machado, and G. Drăgănescu, "Application of the Euler and Runge–Kutta Generalized Methods for FDE and Symbolic Packages in the Analysis of Some Fractional Attractors," Int. J. Nonlinear Sci. Numer. Simul., vol. 21, no. 2, pp. 159–170, Apr. 2020, doi: 10.1515/ijnsns-2018-0248.
[64] R. Y. Rubinstein and D. P. Kroese, Simulation and the Monte Carlo Method, 1st ed. in Wiley Series in Probability and Statistics. Wiley, 2007. doi: 10.1002/9780470230381.
[65] M. A. Rahman, "A Review on Semiconductors Including Applications and Temperature Effects in Semiconductors," Am. Sci. Res. J. Eng. Technol. Sci., vol. 7, no. 1, Art. no. 1, Apr. 2014, Accessed: Mar. 29, 2024. [Online]. Available: https://asrjetsjournal.org/index.php/American_Scientific_Journal/article/view/693
[66] Y. Wu et al., "Lattice Strain Advances Thermoelectrics," Joule, vol. 3, no. 5, pp. 1276–1288, May 2019, doi: 10.1016/j.joule.2019.02.008.
[67] M. R. Hajmohammadi, M. Ahmadian, and S. S. Nourazar, "Introducing highly conductive materials into a fin for heat transfer enhancement," Int. J. Mech. Sci., vol. 150, pp. 420–426, Jan. 2019, doi: 10.1016/j.ijmecsci.2018.10.048.
[68] Á. Lakatos and A. Trník, "Thermal Diffusion in Fibrous Aerogel Blankets," Energies, vol. 13, no. 4, p. 823, Feb. 2020, doi: 10.3390/en13040823.

Appendix I. Solver Implementation Framework

Leveraging the Finite Element Method (FEM), the solver computes temperature distributions within the device under diverse operating conditions and cooling strategies. The solver integrates the one-dimensional heat conduction equation discretized using finite differences to solve for the temperature distribution over time. Boundary conditions, including ambient and hot temperatures, are applied to simulate heat transfer at device interfaces. Additionally, the solver incorporates parameters such as thermal diffusivity, spatial and temporal step sizes, and the length of the device to define the simulation domain and parameters. Through iteratively updating the temperature distribution at each spatial grid point using explicit Euler method, the solver effectively captures the thermal behavior of the semiconductor device.

Python based Solver Implementation

```
import numpy as np
import matplotlib.pyplot as plt

# Define parameters
L = 100.0  # Length of the device (m)
Nx = 100  # Number of spatial grid points
T_ambient = 25.0  # Ambient temperature (°C)
T_hot = 100.0  # Temperature of the hot end (°C)
alpha = 0.1  # Thermal diffusivity (m^2/s)
t_final = 100.0  # Final time for simulation (s)
dt = 0.01  # Time step size (s)
dx = L / Nx  # Spatial step size (m)

# Initialize temperature array
T = np.zeros(Nx)
T[0] = T_ambient
T[-1] = T_hot

# Perform time integration using explicit Euler method
for t in np.arange(0, t_final, dt):
    T_new = np.zeros(Nx)
    for i in range(1, Nx - 1):
        T_new[i] = T[i] + alpha * dt * (T[i+1] - 2*T[i] + T[i-1]) / dx**2
    T = T_new

# Plot temperature distribution
x = np.linspace(0, L, Nx)
plt.plot(x, T)
plt.xlabel('Distance (m)')
plt.ylabel('Temperature (°C)')
plt.title('Temperature Distribution')
plt.grid(True)
plt.show()

# Apply Ohm's Laws
# Standard Ohm's Law: V = RI
R_standard = 50.0  # Constant resistance value (Ω)
V_standard = R_standard * np.ones(Nx)  # Example voltage (V)

# Modified Ohm's Law: V_modified = a * e^(R_short / R_0 * x / L)
R_short = 400.0  # Short resistance (Ω)
R_0 = 100.0  # Reference resistance (Ω)
a = 1  # Constant for Modified Ohm's Law
x_values = np.linspace(0, L, Nx)
V_modified = a * np.exp(R_short / R_0 * x_values / L)
```

```
# Plot voltage distributions
plt.plot(x_values, V_standard, label='Standard Ohm\'s Law', color='blue')
plt.plot(x_values, V_modified, label='Modified Ohm\'s Law', color='red')
plt.xlabel('Distance (m)')
plt.ylabel('Voltage (V)')
plt.title('Voltage Distribution')
plt.grid(True)
plt.legend()
plt.show()
```

Appendix II. Synthetic Data Generator

A Monte Carlo simulation approach was utilized, enabling systematic exploration of a wide range of potential operating conditions by introducing perturbations within predefined ranges for material properties and boundary conditions. This variation, resembling real-world uncertainties, allowed for the random adjustment of parameters such as thermal conductivity and boundary temperatures for each sample within the simulation. Subsequently, temperature distributions were computed using the Finite Element Method (FEM), providing insight into the thermal behavior of the semiconductor device under diverse operating conditions and cooling strategies. To enhance the realism of the synthetic data, noise was incorporated into the temperature distributions, accounting for measurement errors and environmental uncertainties typically encountered in experimental scenarios.

Python Based Synthetic Data Generator

```
import numpy as np
import matplotlib.pyplot as plt
import pandas as pd

# Set font size
plt.rcParams.update({'font.size': 14})

# Define parameters
L = 5.0  # Length of the device (m)
Nx = 100  # Number of spatial grid points
T_ambient = 25.0  # Ambient temperature (°C)
T_hot = 100.0  # Temperature of the hot end (°C)
k_0 = 100  # Thermal conductivity at reference temperature (W/mK)
T_0 = 25.0  # Reference temperature (°C)
a = 1.0  # Constant for Modified Ohm's Law
R_0 = 100.0  # Reference resistance (Ω)
R_short = 50.0  # Short resistance (Ω)
noise_std = 5.0  # Standard deviation of noise

# Define spatial grid
x = np.linspace(0, L, Nx)

# Generate synthetic experimental data using Monte Carlo simulation
np.random.seed(0)  # for reproducibility
num_samples = 1000  # Number of Monte Carlo samples

# Initialize arrays to store synthetic data
temperature_standard_samples = np.zeros((num_samples, Nx))
temperature_modified_samples = np.zeros((num_samples, Nx))

# Finite Element Method (FEM) computation
for i in range(num_samples):
    # Perturb material properties or boundary conditions within some range
    k_material_perturbed = k_0 * np.exp(np.random.uniform(-0.1, 0.1, size=Nx))
    T_boundary_perturbed = np.linspace(np.random.uniform(20, 30), np.random.uniform(90, 110), Nx)

    # Calculate temperature distribution using Finite Element Method (FEM) for Standard Ohm's Law
    T_standard = np.zeros_like(x)
    for j in range(Nx):
        T_standard[j] = np.trapz(k_material_perturbed[:j + 1], x[:j + 1]) + T_boundary_perturbed[j]

    # Calculate temperature distribution using Finite Element Method (FEM) for Modified Ohm's Law
    T_modified = np.zeros_like(x)
    for j in range(Nx):
        T_modified[j] = np.trapz(
```

```
            k_material_perturbed[:j + 1] * np.exp(-a * R_short / R_0 * x[:j + 1] / L), x[:j + 1]) + T_boundary_perturbed[
                j]

    # Add noise to the temperature distributions
    temperature_standard_samples[i] = T_standard + np.random.normal(loc=0, scale=noise_std, size=Nx)
    temperature_modified_samples[i] = T_modified + np.random.normal(loc=0, scale=noise_std, size=Nx)

# Create DataFrame to store synthetic experimental data
df = pd.DataFrame({'Distance': x})
for i in range(num_samples):
    df[f'Temperature_Standard_{i}'] = temperature_standard_samples[i]
    df[f'Temperature_Modified_{i}'] = temperature_modified_samples[i]

# Save data to Excel
df.to_excel('synthetic_experimental_data.xlsx', index=False)
```

Appendix III. Prediction Margins and Temperature Discrepancies

The analysis also involved calculating the margins between the device temperatures predicted by standard and Modified Ohm's Laws, which are depicted in Figure 10. These margins represent the differences in temperature predictions between the two cooling strategies and offer valuable insights into the non-linear relationship between temperature and resistance.

Non-linearity and Margin Variations. A crucial observation from Figure 10 is that the margins between the temperature predictions are not constant across the entire range of ambient temperatures. The depicted results indicate that the margins vary as the ambient temperature increases from 0 °C to 80 °C. This variation contradicts the behavior expected from a strictly linear relationship between temperature and resistance, as assumed by the Standard Ohm's Law. In a scenario with a perfectly linear relationship, the difference in temperature predictions between the two Laws would be constant regardless of the ambient temperature. However, the observed variation in margins suggests a more complex interplay between temperature and resistance, which the Modified Ohm's Law aims to capture.

Validation of Modified Ohm's Law. The non-constant margins observed in Figure 10 validate the importance of considering the temperature dependence of resistance in thermal modeling. The Modified Ohm's Law incorporates this dependence through an exponential term or additional equations, allowing it to predict a more nuanced variation in temperature margins across different ambient conditions. While the Standard Ohm's Law might predict a constant difference in temperature throughout the operating range, the reality reflected in Figure 10 is likely to be closer to the non-linear behavior captured by the Modified Ohm's Law. This highlights the merit of the modified approach for accurate thermal simulations, particularly in scenarios where temperature variations are significant.

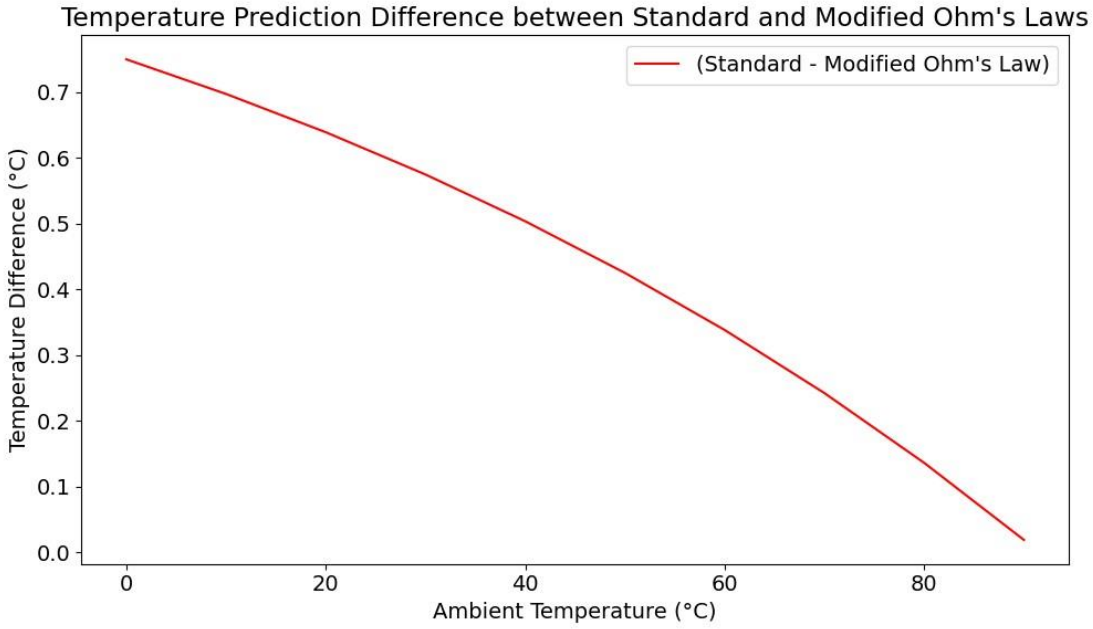

Figure 10. Temperature Prediction Margins between Standard and Modified Ohm's Laws.

Appendix IV. Establishing a Simulation Framework

This section outlines the development of a simulation framework to analyze heat generation and dissipation within a semiconductor device as worked out through section 3 and section 4.

Geometric Parameters

The chosen geometric parameters define the physical characteristics of the device and its surrounding environment, influencing thermal behavior.

Device Geometry. This section details the specifications for the device geometry, including the size and shape of the active regions, contact pads, and interconnects. These dimensions directly influence heat generation within the device.

Substrate Properties. The thickness and material properties of the underlying substrate play a critical role in heat conduction and dissipation. A substrate's thickness can significantly impact its thermal conductivity, with thicker substrates potentially exhibiting different thermal behavior compared to thinner ones.

Heat Sink Design. The design of the heat sink, responsible for transferring heat away from the device, will be scrupulously defined. Parameters including; fin dimensions, spacing, and orientation will be carefully considered to optimize heat transfer efficiency and maximize cooling performance.

Material Properties

Consideration is given to material properties, including thermal conductivity, specific heat capacity, and density, for various components within the semiconductor device, substrate, packaging, and cooling components. For this paper, we will choose the following material properties to represent the thermal characteristics of high-power semiconductor devices.

Thermal Conductivity (κ). This property signifies a material's ability to conduct heat. Materials with higher thermal conductivity can dissipate heat more efficiently, making them ideal for applications involving heat transfer [67].

Specific Heat Capacity (cp). Specific heat capacity refers to the amount of heat energy required to raise the temperature of one unit mass (typically 1 kilogram) of a material by one degree Celsius. This property influences a material's ability to store thermal energy.

Density (ρ). Density represents the mass per unit volume of a material. It plays a role in a material's thermal inertia, which is its resistance to temperature changes. Materials with higher density tend to have higher thermal inertia, meaning they require more heat energy to experience a significant temperature increase [68]. Additionally, density can influence a material's heat storage capacity, as denser materials can store more heat per unit volume.

Boundary Conditions

Choosing appropriate boundary conditions is essential for accurately modeling heat transfer at device interfaces. Boundary conditions govern heat fluxes, temperatures, and thermal resistances at junctions and interfaces, influencing the overall thermal performance of the device. The following boundary conditions to govern heat transfer at device interfaces are established.

Heat Fluxes. The rate of heat transfer per unit area at the device interfaces.

Temperatures. The initial temperatures assigned to different regions of the semiconductor device and the surrounding environment.

Thermal Resistances. The resistance to heat flow at junctions and interfaces between different materials.

These boundary conditions will be applied to govern heat transfer and temperature distribution within the simulated environment, allowing for a realistic representation of thermal behavior in high-power semiconductor devices.

Eurasian Journal of Science Engineering and Technology

Research Article

STRUCTURAL, MAGNETIC AND MAGNETOCALORIC PROPERTIES OF $La_{0.7}Sr_{0.2}Ba_{0.1}MnO_3$ MANGANITE

Mehmet Selim ASLAN[1,*], Selda KILIÇ ÇETİN[2], Ahmet EKİCİBİL[3]

[1,2,3] *Cukurova University, Faculty of Arts and Sciences, Physics Department, Adana, Türkiye*

ABSTRACT

In this present work, the structural, magnetocaloric and magnetic properties of $La_{0.7}Sr_{0.2}Ba_{0.1}MnO_3$ (LSBM) manganite were investigated. The material was synthesized using the sol-gel method and X-Ray Diffraction (XRD), Scanning Electron Microscope (SEM) devices were used to analyze structural properties such as crystal structure and surface morphology. XRD measurement revealed that the crystal structure of LSBM manganite is hexagonal. Based on the magnetic measurements, the T_C value of $La_{0.7}Sr_{0.2}Ba_{0.1}MnO_3$ manganite compounds was calculated as 362 K. The ΔS_M value of sample is established as 2.79 Jkg-1K-1 in an applied magnetic field of 5T. Arrott curves revealed that the phase transition was second order.

Keywords: Magnetocaloric effect, Perovskite, Magnetic entropy change, Curie temperature.

1. INTRODUCTION

As a result of increasing expectations regarding climate change, population growth and living comfort, energy demands for cooling technologies are increasing worldwide. In addition to the increasing energy demand, it becomes necessary to develop new technologies that can replace the cooling systems that are widely used today. These systems in current use have low energy efficiency and are known for consuming significant amounts of energy. Moreover, the use of high vibration compressors in these systems causes noise pollution and more energy consumption. In addition, the refrigerants used in these systems cause environmental pollution [1, 2].

Magnetic cooling (MC) is an alternative cooling technology that can operate without gas-based coolers. Compared to gas compression systems, they have advantages such as not containing environmentally harmful cooling materials, being more efficient, compactness, and operating without noise and vibration [3, 4]. Although it has been heard by everyone for a long time, magnetic cooling technologies cannot yet be used as a potential cooling method in our daily life and industrial areas. The basis of MC systems is based on the MCE principle [5]. MCE is defined as the change in temperature of a magnetic material under an external magnetic field [6, 7]. MCE covers two fundamental processes: adiabatic temperature change (ΔTad) and magnetic entropy change (ΔS_M). The important requirement for MC technologies is that these two parameters have high values around room temperature. While various material families are being investigated for this purpose, manganites are promising due to their low costs, high resistivity, reduced eddy-current-loss compared to metallic alloys, simple production methods and second-order phase transition [8]. Additionally, the fact that magnetic phase transition temperatures can be adjusted through doping makes these materials stand out [8, 9]. This work presents the structural, magnetocaloric and magnetic properties of LSBM sample and provides detailed analysis and measurements to reveal the properties of this material.

2. MATERIAL AND METHOD

In the production of magnetic materials with high magnetocaloric effect, doping elements and amounts are also of great importance, as well as the material production method [10, 11]. Among various methods, the sol-gel method was preferred due to its advantages such as obtaining finer and homogeneously dispersed particle sizes.

Firstly, the stoichiometric amounts of the starting compounds were calculated. Then, aqueous solutions of each compound were prepared and mixed with a magnetic stirrer. Ethylene glycol and citric acid are added to the solution in appropriate proportions to obtain the gel structure. The material obtained in gel form was subjected to heat treatment in the oven at 450°C for 1 hour in order to be removed from the beaker properly. The obtained powder sample was calcined at 600°C for 6 hours to remove organic compound residues. Then, the samples were ground in an agate mortar for a total of 60 minutes with 6 grinding sessions of 10 minutes each. The powdered samples were turned into tablets using a hydraulic press. As a final process, the materials were sintered in a cylindrical oven at 1200 °C for 24 hours to crystallize.

* Corresponding author, e-mail: mehmetselimaslan34@gmail.com (M. S. Aslan)
Recieved: 24.04.2024 Accepted: 30.05.2024
doi: 10.55696/ejset.1417171

The structural analysis of the produced manganite compound was carried out by XRD and SEM measurements. Diffraction patterns of the manganite compound were analyzed in HighScore Plus programs. Additionally, magnetic properties are evaluated using the PPMS Dynacool 9T instrument to determine key parameters such as Curie temperature, type of magnetic phase transition and ΔS_M values.

3. RESULTS AND DISCUSSION

XRD method was used to understand the structural properties of the synthesized samples. According to the XRD curve given in Figure 1, the presence of sharp and narrow-based peaks indicates that crystallization has occurred well. The fact that the FHWM value for the 2θ = 32.576 peak is 0.25279 supports this. Based on the XRD results, our manganite compound is classified under R-3c space group and exhibits a hexagonal structure. The lattice parameters were obtained using the HighScore Plus program, where a = 5.5100, b = 5.5100 and c = 13.3880 Å, respectively. It was determined that the observed peaks were compatible with the reference code (98-018-7646)[12]. Additionally, the XRD pattern of the compound did not exhibit any peaks associated with undesirable phases. This absence indicates that the synthesis process was successful in obtaining the desired material without significant impurities.

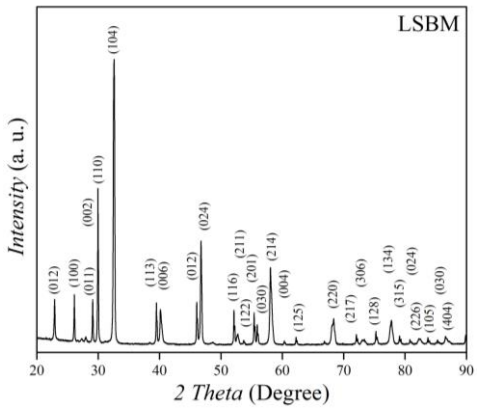

Figure 1. XRD pattern of LSBM manganite.

Scanning Electron Microscope (SEM) technique has been selected to obtain a grain structure image to analyze morphological features of the the sample. SEM images taken at 5, 10, 20 and 40 kX magnifications are given in Figure 2. When the SEM images of the compound are examined, many volumetric particle structures are revealed. These structures exhibit a wide range of different sizes and polygonal shapes, each distinctly separated from each other.

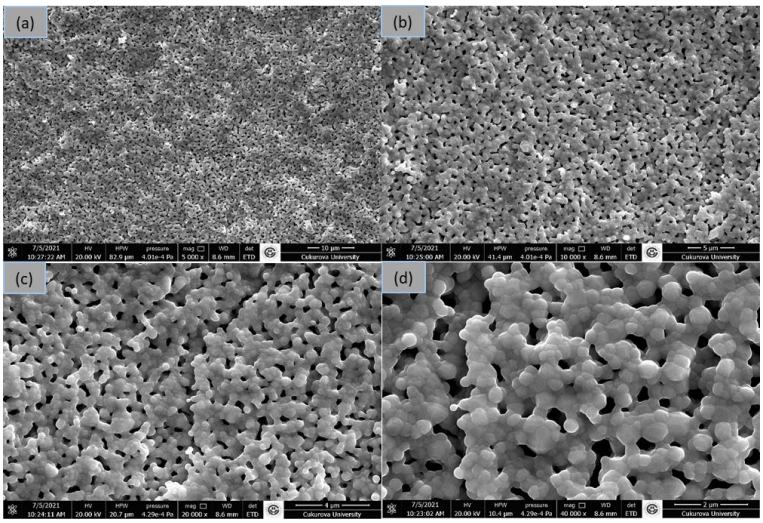

Figure 2. SEM images of LSBM manganite taken at different magnifications; (a) 5 kX, (b) 10 kX, (c) 20 kX and (d) 40 kX

The transition temperature value of the material has been identified using the *M(T)* curves, and the magnetocaloric features have been examined based on the isothermal magnetization curves obtained in the vicinity of this determined temperature. *M(T)* measurements have been performed under Field Cooling (FC) and Zero Field Cooling (ZFC) mode. In Figure 3, we observe the temperature-induced magnetization changes in a low magnetic field value of 10mT for both the ZFC and FC processes. While the *M(T)* curves obtained in the ZFC and FC steps behave similarly at temperatures above T_C, they diverge in the low-temperature range. This distinction between ZFC and FC steps is related to consepts such as spin glass like behavior, long-range or short range magnetic interaction in the material and the magnitude of its magnetic anisotropy [13, 14]. By examining the *dM/dT-T* curve, the temperature at which it reachs its minumum point signifies the T_C for this sample. The sample did a transition from ferromagnetic to paramagnetic at T_C=360 K.

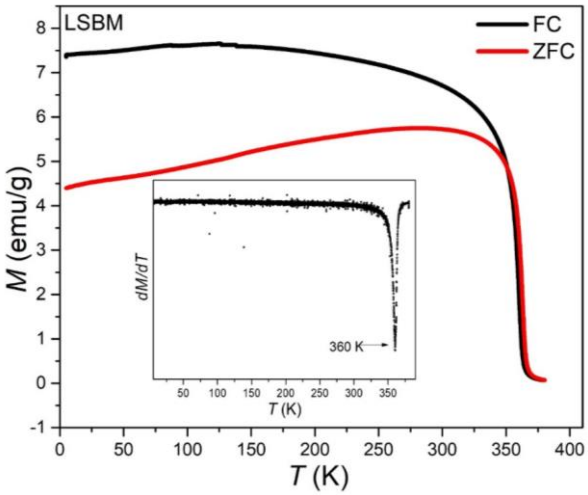

Figure 3. The *M(T)* curves of the LSBM manganite subjected to a 10 mT magnetic field in both ZFC and FC modes. Inset figures display (*dM/dT*)-*T* curves of the sample.

After determining the magnetic phase transition temperature, isothermal magnetization measurements, *M(H),* were conducted in the vicinity of that temperature region. Measurements were taken from 254 K to 378 K, with a 4 K increment, as illustrated in Figure 4. *M(H)* curves exhibit transitions from saturated curves in the ferromagnetic region to linear curves in the paramagnetic region as the temperature increases. This observation suggests a shift in magnetic behavior from one dominated by ferromagnetic alignment, where the magnetic moments of atoms align parallel to each other resulting in saturation of magnetization, to one characterized by paramagnetic behavior, where the alignment becomes disordered with increasing temperature, leading to a linear relationship between magnetization and magnetic field.

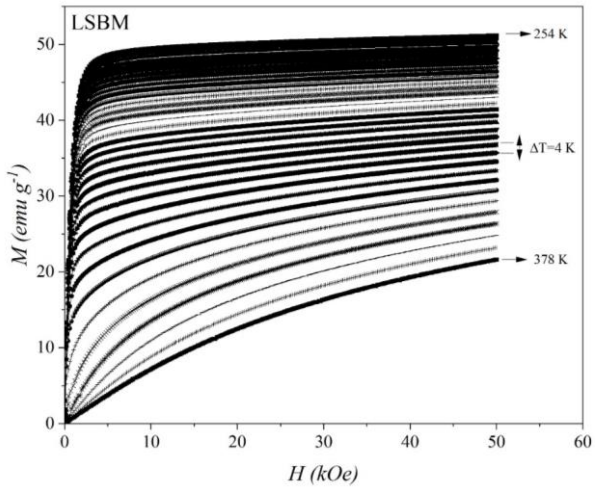

Figure 4. *M(H)* curves of LSBM at 4K temperature steps around T_C temperature.

Isothermal magnetic entropy change, ΔS_M, serves a crucial parameter for characterizing the magnetocaloric properties of a magnetic material. The values of ΔS_M were determined by performing a series of calculations on the isothermal *M(H)* curves, which are given in Figure 5. The ΔS_M as a function of temperature curves showed a peak around the Curie temperature region, as expected. Moreover, the ΔS_M values increased with increasing applied field strengths. This observation is consistent with the behavior typically exhibited by magnetic materials undergoing phase transitions, where the ΔS_M tends to peak around the critical temperature and shows dependence on the applied magnetic field strength. The ΔS_M values corresponding to various applied magnetic fields are listed in Table 1.

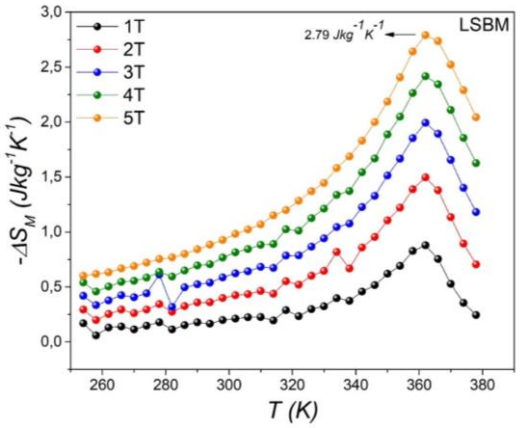

Figure 5. The magnetic entropy change curves of LSBM compound at different field values.

Table 1. ΔS_M values obtained under different applied magnetic fields.

Sample	ΔS_M (Jkg^{-1}K^{-1})					T_C (K)
	1 T	2 T	3 T	4 T	5 T	
LSBM	0.89	1.52	2.01	2.24	2.79	360

Figure 6 displays Arrott measurements conducted to determine the type of magnetic phase transition of our manganite compound. Curves can exhibit positive or negative slope. In the case where the Arrott curve exhibits a positive slope, as observed in our material, it indicates a second-order magnetic phase transition [15]. The positive slope of the Arrott curve suggests that the material undergoes a gradual transition from one magnetic phase to another, without the formation of domain walls or the release of latent heat, which are characteristic of first-order phase transitions [16].

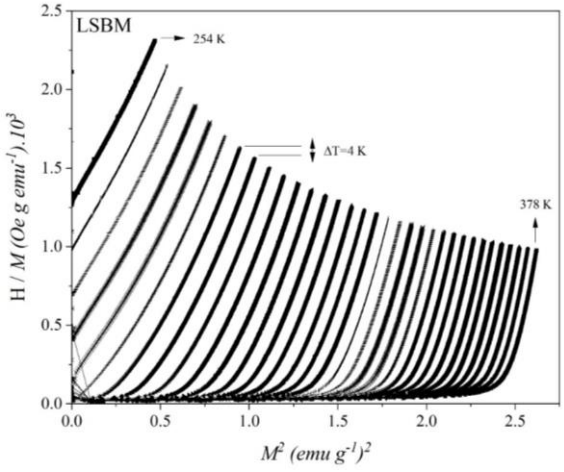

Figure 6. Arrott curves of LSBM manganite.

4. CONCLUSION

In the present study, $La_{0.7}Sr_{0.2}Ba_{0.1}MnO_3$ manganite was synthesized using the Sol-Gel method. The structural, magnetocaloric and magnetic properties of the synthesized this compound were examined in detail. XRD analysis revealed that the compound crystallized in the R-3c space group, exhibiting a hexagonal structure. SEM images taken at magnifications of 5, 10, 20 and 40 kX revealed volumetric particle structures of various sizes and polygonal shapes. Measurements of magnetization as a function of temperature indicated that as the temperature decreased, the sample transitioned from a ferromagnetic state to a paramagnetic state. To determine ΔS_M values, isothermal magnetization measurements were made around the transition temperature of the sample, where the magnetization change is maximum. As a result of magnetic studies, it was determined that the *Tc* temperature of our manganite was 360 K and the ΔS_M value under a 5T changing magnetic field was 2.79 $Jkg^{-1}K^{-1}$. Furthermore, it is understood from the Arrott curves that the sample has a second-order magnetic phase transition.

SIMILARITY RATE: 16%

AUTHOR CONTRIBUTION

Mehmet Selim ASLAN: Conceptualization, methodology, data curation, writing, editing etc.
Selda KILIÇ ÇETİN: Conceptualization, methodology, data curation, writing, editing etc.
Ahmet EKİCİBİL: Characterization, editing.

CONFLICT of INTEREST

The authors declared that they have no known conflict of interest.

ACKNOWLEDGEMENT

We are grateful that present study is supported by the Çukurova University Scientific Research Projects under grant agreement no: FDK-2021-13983.

REFERENCES

[1] M. Mazaheri, M. Akhavan, "Electrical behavior of nano-polycrystalline (La1−yKy)0.7Ba0.3MnO3 manganites", *Journal of Magnetism and Magnetic Materials*, 322 (2010) 3255-3261.
[2] X. Zhao, X. Zheng, X. Luo, F. Gao, H. Zeng, G. Yu, S.U. Rehman, C. Chen, S. Ma, W. Ren, Z. Zhong, "Large magnetocaloric effect and magnetoresistance in ErNi single crystal", *Journal of Materials Science & Technology*, 86 (2021) 56-63.
[3] A. Elghoul, A. Krichene, N. Chniba Boudjada, W. Boujelben, "Rare earth effect on structural, magnetic and magnetocaloric properties of La0.75Ln0.05Sr0.2MnO3 manganites", *Ceramics International*, 44 (2018) 12723-12730.
[4] S.M. Gombi, D. Sahu, "A Review on Magneto-Caloric Materials for Room Temperature Refrigeration", *International Journal of Automotive and Mechanical Engineering*, 17 (2020) 7805-7815.
[5] X. Tang, H. Sepehri-Amin, N. Terada, A. Martin-Cid, I. Kurniawan, S. Kobayashi, Y. Kotani, H. Takeya, J. Lai, Y. Matsushita, T. Ohkubo, Y. Miura, T. Nakamura, K. Hono, "Magnetic refrigeration material operating at a full temperature range required for hydrogen liquefaction", *Nat Commun*, 13 (2022) 1817.
[6] A.M. Gomes, F. Garcia, A.P. Guimarães, M.S. Reis, V.S. Amaral, P.B. Tavares, "Magnetocaloric effect of the (Pr,Ca)MnO3 manganite at low temperatures", J*ournal of Magnetism and Magnetic Materials*, 290-291 (2005) 694-696.
[7] M. Quintero, J. Sacanell, L. Ghivelder, A.M. Gomes, A.G. Leyva, F. Parisi, "Magnetocaloric effect in manganites: Metamagnetic transitions for magnetic refrigeration", *Applied Physics Letters*, 97 (2010).
[8] S.K. Çetin, "Reversible Magnetocaloric Effect of (La0.8Pr0.2)(0.67)Ba0.33MnO3 from Direct Measurements", *Journal Of Superconductivity And Novel Magnetism*, 33 (2020) 683-691.
[9] M.-H. Phan, H.-X. Peng, S.-C. Yu, N. Duc Tho, N. Chau, "Large magnetic entropy change in Cu-doped manganites", *Journal of Magnetism and Magnetic Materials*, 285 (2005) 199-203.

[10] F. Ayadi, F. Saadaoui, W. Cheikhrouhou-Koubaa, M. Koubaa, A. Cheikhrouhou, L. Sicard, S. Ammar, "Effect of monovalent doping on the physical properties of La0.7Sr0.3MnO3compound synthesized using sol-gel technique", *IOP Conference Series: Materials Science and Engineering*, 28 (2012).
[11] S. Choura Maatar, R. M'nassri, W. Cheikhrouhou Koubaa, M. Koubaa, A. Cheikhrouhou, "Structural, magnetic and magnetocaloric properties of La0.8Ca0.2−Na MnO3 manganites (0≤x≤0.2)", *Journal of Solid State Chemistry*, 225 (2015) 83-88.
[12] A.C.B. Cheikhrouhou, N.;Cheikhrouhou-Koubaa, W.;M'nassri, R., *Journal of Solid State Chemistry*, 119 (1995) 191-196.
[13] B. Kumar, J.K. Tiwari, H.C. Chauhan, S. Ghosh, "Multiple magnetic phase transitions with different universality classes in bilayer La1.4Sr1.6Mn2O7 manganite", *Scientific Reports*, 11 (2021) 21184.
[14] A. Coşkun, E. Taşarkuyu, A.E. Irmak, S. Aktürk, "High magnetic entropy change in La0.70Ca0.21Ag0.09MnO3 compound", *Journal of Alloys and Compounds*, 669 (2016) 217-223.
[15] M. Balli, P. Fournier, S. Jandl, M.M. Gospodinov, "A study of the phase transition and magnetocaloric effect in multiferroic La2MnNiO6 single crystals", *Journal of Applied Physics*, 115 (2014).
[16] J.Y. Law, V. Franco, L.M. Moreno-Ramírez, A. Conde, D.Y. Karpenkov, I. Radulov, K.P. Skokov, O. Gutfleisch, "A quantitative criterion for determining the order of magnetic phase transitions using the magnetocaloric effect", *Nat Commun*, 9 (2018) 2680.

Eurasian Journal of Science Engineering and Technology

Research Article

A NEW SOFT SET OPERATION: COMPLEMENTARY EXTENDED STAR OPERATION

Aslıhan SEZGİN[1,*], Murat SARIALİOĞLU[2]

[1] *Amasya University, Faculty of Education, Department of Mathematics and Science Education, Amasya, Türkiye*
[2]*Amasya University, Graduate School of Natural and Applied Sciences, Department of Mathematics, Amasya, Türkiye*

ABSTRACT

Soft set theory has established itself as a valuable mathematical framework for tackling issues marked by uncertainty, demonstrating its applicability across a range of theoretical and practical fields since its inception. Central of this theory is the operations of soft sets. To enhance the theory and to make a theoretical contribution to the theory, a new type of soft set operation, called "complementary extended star operation" for soft set, is proposed. An exhaustive examination of the properties of this operation has been undertaken, including its distributions over other soft set operations, with the goal of clarifying the relationship between the complementary extended star operation and other soft set operations. This paper also attempts to make a contribution to the literature of soft sets in the sense that studying the algebraic structure of soft sets from the standpoint of soft set operations offers a comprehensive understanding of their application as well as an appreciation of how soft set can be applied to classical and nonclassical logic.

Keywords: Soft Set, Soft Set Operations, Complementary Extended Soft Set Operations

1. INTRODUCTION

In our everyday experiences, we frequently encounter subjective notions like beauty, warmth, and boredom, which lack the objective certainty of scientific knowledge and vary from individual to individual. To navigate the intricacies of uncertainty, people have sought diverse solutions over time. However, existing methodologies have demonstrated inconsistencies in addressing novel, complex challenges stemming from changing circumstances. Among the array of theories proposed to manage uncertain scenarios, Zadeh's theory of fuzzy sets emerges as particularly prominent. Fuzzy sets are delineated by their membership functions. As the theory of fuzzy sets underwent rapid evolution, certain structural dilemmas surfaced. In response, Molodtsov [1] introduced soft set theory as a remedy for these structural intricacies.

Since its introduction, the soft set has been used in a wide range of theoretical and practical contexts, and several new research have been released in the literature. By defining the equality of two soft sets, the subset and superset of a soft set, the complement of a soft set, and soft binary operations like and/or, union, and intersection operations for soft sets, Maji et al. [2] cleared the way for further research in the field of soft set theory. Based on ideas from set theory, Pei and Miao [3] redefined the terms "soft subset" and "intersection of two soft sets." Next, several additional soft set operations were proposed by Ali et al. [4], and they were thoroughly examined by Sezgin and Atagün [5] and Ali et al. [6]. Extended difference and extended symmetric difference of soft sets were described by Sezgin et al. [7] and Stojanovic [8], respectively, and their characteristics were thoroughly examined in connection to other operations on soft sets.

Analysis of the research done to date reveals that soft set operations often fall into two categories: restricted soft set operations and extended soft set operations. The soft binary piecewise difference operation for soft sets was defined and analyzed by Eren and Çalışıcı [9], while Sezgin and Çalışıcı [10] conducted a detailed study of this soft set operation's properties. In 2021, Çağman [11] introduced a new notion in set theory: the inclusive and exclusive complement of sets. He then used this concept in group theory. Five new ideas related to binary complement operations presented by Çağman [11] were introduced by Sezgin et al. [12]. Aybek [13] presented several additional restricted and extended soft set operations and examined their properties. Furthermore, by taking the complement of the image set in the first row, the soft binary piecewise operation form-of which Eren and Çağman [9] were the pioneers-was somewhat changed. As a result, the complementary soft binary piecewise operations have been thoroughly examined by a number of scholars [14-22]. On the other hand, by taking the complement of the image set in the first and second rows and defining the complementary extended difference, lambda and union, plus and theta, respectively, and giving their algebraic properties and relations with other soft set operations, Akbulut [23] and Demirci [24] changed the form of the existing extended soft set operations in the literature. We refer to the following for more uses of soft sets in relation to algebraic structures: [25-32].

* Corresponding author, e-mail:aslihan.sezgin@amasya.edu.tr
Received: 10.05.2024 Accepted: 11.06.2024
doi: 10.55696/ejset.1481722

Studying the properties of specified operations on sets, alongside the sets themselves, constitutes an essential aspect of algebraic structures, aiming to classify mathematical structures. Within the framework of algebra, this examination plays a crucial role. When considering soft sets as algebraic structures, attention is drawn to two primary types of soft set collections: one characterized by a fixed set of parameters, and the other by variable parameter sets. Just as classical set theory operations are foundational for soft sets, concepts pertaining to soft set operations are equally indispensable.

In this paper, in an effort to propel the theory of soft sets forward, this paper introduces a new soft set operation called "complementary extended star operation" and conducts a comprehensive examination of its properties. Furthermore, an analysis is undertaken to explore the interaction between the complementary extended star operation and other types of soft set operations, with the objective of elucidating their relationships. This subject is important within the framework as an understanding of the applications of soft sets requires a comprehension of their algebraic structures in connection to innovative operations.

PRELIMINARIES

Definition 2.1. Let U be the universal set, E be the parameter set, P(U) be the power set of U, and let $D \subseteq E$. A pair (F, D) is called a soft set on U. Here, F is a function given by $F: D \rightarrow P(U)$ [1].

The notation of the soft set (F,D) is also shown as F_D, however, we prefer to use the notation of (F,D) as is used by Molodtsov [1] and Maji et al. [2].

The set of all soft sets over U is denoted by $S_E(U)$. Let K be a fixed subset of E, then the set of all soft sets over U with the fixed parameter set K is denoted by $S_K(U)$. In other words, in the collection $S_K(U)$, only soft sets with the parameter set K are included, while in the collection $S_E(U)$, soft sets over U with any parameter set can be included. Clearly, the set $S_K(U)$ is a subset of the set $S_E(U)$.

Definition 2.2. Let (F,D) be a soft set over U. If $F(\aleph)=\emptyset$ or all $\aleph \in D$, then the soft set (F,D) is called a null soft set with respect to D, denoted by $\emptyset_D$. Similarly, let (F,E) be a soft set over U. If $F(e)=\emptyset$ for all $\aleph \in E$, then the soft set (F,E) is called a null soft set with respect to E, denoted by $\emptyset_E$ [4].

A soft set can be defined as $F: \emptyset \longrightarrow P(U)$, where U is a universal set. Such a soft set is called an empty soft set and is denoted by $\emptyset_\emptyset$. Thus, $\emptyset_\emptyset$ is the only soft set with an empty parameter set [6].

Definition 2.3. Let (F,D) be a soft set over U. If $F(\aleph)=U$ for all $\aleph \in D$, then the soft set (F,K) is called a relative whole soft set with respect to D, denoted by U_D. Similarly, let (F,E) be a soft set over U. If $F(e)=U$ for all $\aleph \in E$, then the soft set (F,E) is called a whole soft set with respect to E, denoted by U_E [4].

Definition 2.4. Let (F,D) and (G,Y) be soft sets over U. If $D \subseteq Y$ and $F(\aleph) \subseteq G(\aleph)$ for all $\aleph \in D$, then (F,D) is said to be a soft subset of (G,Y), denoted by $(F,D) \widetilde{\subseteq} (G,Y)$. If (G,Y) is a soft subset of (F,D), then (F,D) is said to be a soft superset of (G,Y), denoted by $(F,D) \widetilde{\supseteq} (G,Y)$. If $(F,D) \widetilde{\subseteq} (G,Y)$ and $(G,Y) \widetilde{\subseteq} (F,D)$, then (F,D) and (G,Y) are called soft equal sets [3].

Definition 2.5. Let (F,D) be a soft set over U. The soft complement of (F,D), denoted by $(F,D)^r = (F^r,D)$, is defined as follows: for all $\aleph \in D$, $F^r(\aleph)=U-F(\aleph)$ [4]

Çağman [11] introduced two new complements as a novel concept in set theory, termed as the inclusive complement and exclusive complement. For ease of representation, we denote these binary operations as + and θ, respectively. For two sets D and Y, these binary operations are defined as $D+Y=D' \cup Y$, $D\theta Y=D' \cap Y'$. Sezgin et al. [12] examined the relations between these two operations and also defined three new binary operations and analyzed their relations with each other. Let D and Y be two sets $D*Y=D' \cup Y'$, $D\gamma Y= D' \cap Y$, $D\lambda Y=D \cup Y'$.

As a summary for soft set operations, we can categorize all types of soft set operations as follows: Let "$\circledast$" be used to represent the set operations (i.e., here $\circledast$ can be $\cap, \cup, \setminus, \Delta, +, \theta, *, \lambda, \gamma$), then all type of soft set operations are defined as follows:

Definition 2.6. Let $(F, D), (G, Y) \in S_E(U)$. The restricted $\circledast$ operation of (F, D) and (G, Y) is the soft set (H,P), denoted by $(F, D) \circledast_{\Re} (G, Y) = (H, P)$, where $P=D \cap Y \neq \emptyset$ and $H(\aleph)=F(\aleph) \circledast G(\aleph)$ for all $\aleph \in P$. Here, if $P=D \cap Y=\emptyset$, then $(F, D) \circledast_R (G, Y)=\emptyset_\emptyset$ [4,5,6,13].

Definition 2.7. Let $(F, D), (G, Y) \in S_E(U)$. The extended $\circledast$ operation (F, D) and (G, Y) is the soft set (H, P), denoted by (F, D) $\circledast_\varepsilon$(G, Y) = (H, P), where $P = D \cup Y$ and for all $\aleph \in P$,

$$H(\aleph) = \begin{cases} F(\aleph), & \aleph \in D - Y \\ G(\aleph), & \aleph \in Y - D \\ F(\aleph) \circledast G(\aleph), & \aleph \in D \cap Y \end{cases}$$

[2,4,6,7,8,13].

Definition 2.8. Let $(F, D), (G, Y) \in S_E(U)$. The complementary extended $\circledast$ operation (F, D) and (G, Y) is the soft set (H, P), denoted by $(F, D) \overset{*}{\underset{\circledast_\varepsilon}{}} (G, Y) = (H, P)$, where $P = D \cup Y$ and for all $\aleph \in P$,

$$H(\aleph) = \begin{cases} F'(\aleph), & \aleph \in D - Y \\ G'(\aleph), & \aleph \in Y - D \\ F(\aleph) \circledast G(\aleph), & \aleph \in D \cap Y \end{cases}$$

[23,24].

Definition 2.9. Let $(F, D), (G, Y) \in S_E(U)$. The soft binary piecewise $\circledast$ of (F,D) and (G,Y) is the soft set (H,D), denoted by $(F, D) \underset{\circledast}{\sim} (G, Y) = (H, D)$, where for all $\aleph \in D$

$$H(\aleph) = \begin{cases} F(\aleph), & \aleph \in D - Y \\ F(\aleph) \circledast G(\aleph), & \aleph \in D \cap Y \end{cases}$$

[9,10,33,34].

Definition 2.10. Let $(F, D), (G, Y) \in S_E(U)$. The complementary soft binary piecewise $\circledast$ of (F,D) and (G,Y) is the soft set (H,D), denoted by $(F, D) \overset{*}{\underset{\circledast}{\sim}} (G, Y) = (H, D)$, where for all $\aleph \in D$

$$H(\aleph) = \begin{cases} F'(\aleph), & \aleph \in D - Y \\ F(\aleph) \circledast G(\aleph), & \aleph \in D \cap Y \end{cases}$$

[14-22].

For the considerations of graph applications and network analysis as regards soft sets, we refere to [35], which is motivated by the divisibility of determinants.

3. COMPLEMENTARY EXTENDED STAR OPERATION

In this section, a new soft set operation called complementary extended star operation of soft sets is introduced with its example and its full algebraic properties are analyzed.

Definition 3.1. Let (F, Z), (G,C) be soft sets over U. The complementary extended star operation $(*)$ operation of (F, Z) and (G, C) is the soft set (H, K), denoted by $(F , Z) \overset{*}{\underset{*_\varepsilon}{}} (G,C) = (H, K)$, where for all $\aleph \in K = Z \cup C$,

$$H(\aleph) = \begin{cases} F'(\aleph), & \aleph \in Z\text{-}C \\ G'(\aleph), & \aleph \in C\text{-}Z \\ F(\aleph) * G(\aleph), & \aleph \in Z \cap C \end{cases}$$

where $F(\aleph) * G(\aleph) = F'(\aleph) \cup G'(\aleph)$ for all $\aleph \in Z \cap C$.

Example 3.2 Let $E=\{e_1,e_2,e_3,e_4\}$ be the parameter set and $Z=\{e_1, e_3\}$ and $C=\{e_2, e_3, e_4\}$ be two subsets of E, and $U=\{h_1,h_2,h_3,h_4,h_5\}$ be the universal set. Assume that $(F,Z)=\{(e_1,\{h_2,h_5\}),(e_3,\{h_1,h_2,h_5\})\}$, $(G,C)=\{(e_2,\{h_1,h_4,h_5\}),(e_3,\{h_2,h_3,h_4\}),(e_4,\{h_3,h_5\})\}$ be two soft sets over U. Let $(F,Z) \overset{*}{\underset{*_\varepsilon}{}} (G,C)=(L,Z \cup C)$, where for all $\aleph \in Z \cup C$,

$$L(\aleph)=\begin{cases} F'(\aleph), & \aleph\in Z-C \\ G'(\aleph), & \aleph\in C-Z \\ F'(\aleph)\cup G'(\aleph), & \aleph\in Z\cap C \end{cases}$$

Here, since $Z\cup C=\{e_1,e_2,e_3,e_4\}$, $Z-C=\{e_1\}$, $C-Z=\{e_2,e_4\}$, $Z\cap C=\{e_3\}$, $L(e_1)=F'(e_1)=\{h_1,h_3,h_4\}, L(e_2)=G'(e_2)=\{h_2,h_3\}, L(e_4)=G'(e_4)=\{h_1,h_2,h_4\}, H(e_3)=F'(e_3)\cup G'(e_3)=\{h_3,h_4\}\cup\{h_1,h_5\}=\{h_1,h_3,h_4,h_5\}$. Hence,

$$(F,Z)\overset{*}{}_{*_\varepsilon}(G,C)=\{(e_1,\{h_1,h_3,h_4\}),(e_2,\{h_2,h_3\}),(e_3,\{h_1,h_3,h_4,h_5\}),(e_4,\{h_1,h_2,h_4\})\}$$

Theorem 3.3. (Algebraic Properties of Operation)

1) The set $S_E(U)$ is closed under $\overset{*}{}_{*_\varepsilon}$.

***Proof*:** It is clear that $\overset{*}{}_{*_\varepsilon}$ is a binary operation on $S_E(U)$. Indeed,

$$\overset{*}{}_{*_\varepsilon}: S_E(U)\text{x } S_E(U)\to S_E(U)$$

$$((F,Z),(G,C))\to (F,Z)\overset{*}{}_{*_\varepsilon}(G,C)=(L,Z\cup C)$$

Similarly,

$$\overset{*}{}_{*_\varepsilon}: S_Z(U)\text{x } S_Z(U)\to S_Z(U)$$

$$((F,Z),(G,Z))\to (F,Z)\overset{*}{}_{*_\varepsilon}(G,Z)=(T,Z\cup Z)=(T,Z)$$

That is, when Z is a fixed subset of the set E and (F,Z) and (G,Z) be elements of $S_Z(U)$, then so is $(F,Z)\overset{*}{}_{*_\varepsilon}(G,Z)$. Namely, $S_Z(U)$ is closed under $\overset{*}{}_{*_\varepsilon}$ either.

2) $[(F,Z)\overset{*}{}_{*_\varepsilon}(G,C)]\overset{*}{}_{*_\varepsilon}(H,R)\neq(F,Z)\overset{*}{}_{*_\varepsilon}[(G,C)\overset{*}{}_{*_\varepsilon}(H,R)]$.

Proof : First, let's handle the left hand side (LHS). Let $(F,Z)\overset{*}{}_{*_\varepsilon}(G,C)=(T,Z\cup C)$, where for all $\aleph\in Z\cup C$,

$$T(\aleph)=\begin{cases} F'(\aleph), & \aleph\in Z-C \\ G'(\aleph), & \aleph\in C-Z \\ F'(\aleph)\cup G'(\aleph), & \aleph\in Z\cap C \end{cases}$$

Let $(T,Z\cup C)\overset{*}{}_{*_\varepsilon}(H,R)=(M,Z\cup C\cup R)$, where for all $\aleph\in Z\cup C\cup R$,

$$M(\aleph)=\begin{cases} T'(\aleph), & \aleph\in(Z\cup C)-R \\ H'(\aleph), & \aleph\in R-(Z\cup C) \\ T'(\aleph)\cup H'(\aleph), & \aleph\in(Z\cup C)\cap R \end{cases}$$

Thus,

$$M(\aleph)=\begin{cases} F(\aleph), & \aleph\in(Z-C)-R=Z\cap C'\cap R' \\ G(\aleph), & \aleph\in(C-Z)-R=Z'\cap C\cap R' \\ F(\aleph)\cap G(\aleph), & \aleph\in(Z\cap C)-R=Z\cap C\cap R' \\ H'(\aleph) & \aleph\in R-(Z\cup C)=Z'\cap C'\cap R \\ F(\aleph)\cup H'(\aleph), & \aleph\in(Z-C)\cap R=Z\cap C'\cap R \\ G(\aleph)\cup H'(\aleph), & \aleph\in(C-Z)\cap R=Z'\cap C\cap R \\ \big(F(\aleph)\cap G(\aleph)\big)\cup H'(\aleph), & \aleph\in(Z\cap C)\cap R=Z\cap C\cap R \end{cases}$$

Now let's handle the right hand side (RHS) of the equation. Let $(G,C) \overset{*}{*_\varepsilon} (H,R)=(K,C\cup R)$. Here, for all $x\in C\cup R$,

$$K(x)=\begin{cases} G'(x), & x\in C-R \\ H'(x), & x\in R-C \\ G'(x)\cup H'(x), & x\in C\cap R \end{cases}$$

Assume that $(F,Z) \overset{*}{*_\varepsilon} (K,C\cup R) = (S,Z\cup C\cup R)$, where for all $x\in Z\cup C\cup R$,

$$S(x)=\begin{cases} F'(x), & x\in Z-(C\cup R) \\ K'(x), & x\in (C\cup R)-Z \\ F'(x)\cup K'(x), & x\in Z\cap (C\cup R) \end{cases}$$

Thus,

$$S(x)=\begin{cases} F'(x), & x\in Z-(C\cup R)=Z\cap C'\cap R' \\ G(x), & x\in (C-R)-Z=Z'\cap C\cap R' \\ H(x) & x\in (R-C)-Z=Z'\cap C'\cap R \\ G(x)\cap H(x), & x\in (C\cap R)-Z=Z'\cap C\cap R \\ F'(x)\cup G(x), & x\in Z\cap (C-R)=Z\cap C\cap R' \\ F'(x)\cup H(x), & x\in Z\cap (R-C)=Z\cap C'\cap R \\ F'(x)\cup (G(x)\cap H(x)), & x\in Z\cap (C\cap R)=Z\cap C\cap R \end{cases}$$

It is seen that $M\neq S$. That is, in the set $S_E(U)$, $\overset{*}{*_\varepsilon}$ is not associative.

3) $[(F,Z) \overset{*}{*_\varepsilon} (G,Z)] \overset{*}{*_\varepsilon} (H,Z) \neq (F,Z) \overset{*}{*_\varepsilon} [(G,Z) \overset{*}{*_\varepsilon} (H,Z)]$.

Proof : Firstly, let's look at the LHS. Let $(F,Z) \overset{*}{*_\varepsilon} (G,Z)=(T,Z\cup Z)$, where for all $x \in Z\cup Z=Z$,

$$T(x)=\begin{cases} F'(x), & x\in Z-Z=\emptyset \\ G'(x), & x\in Z-Z=\emptyset \\ F'(x)\cup G'(x), & x\in Z\cap Z=Z \end{cases}$$

Let $(T,Z) \overset{*}{*_\varepsilon} (H,Z) = (M, Z\cup Z)$, where for all $x\in Z$,

$$M(x)=\begin{cases} T'(x), & x\in Z-Z=\emptyset \\ H'(x), & x\in Z-Z=\emptyset \\ T'(x)\cup H'(x), & x\in Z\cap Z=Z \end{cases}$$

Thus,

$$M(x)=\begin{cases} T'(x), & x \in Z-Z=\emptyset \\ H'(x), & x\in Z-Z=\emptyset \\ (F(x)\cap G(x))\cup H'(x), & x\in Z\cap Z=Z \end{cases}$$

Now, let's handle RHS. Let $(G,Z) \overset{*}{*_\varepsilon} (H,Z)=(L, Z\cup Z)$, where for all $x\in Z$,

$$L(x)=\begin{cases} G'(x), & x\in Z-Z=\emptyset \\ H'(x), & x\in Z-Z=\emptyset \\ G'(x)\cup H'(x), & x\in Z\cap Z=Z \end{cases}$$

Let $(F,Z) \overset{*}{}_{*_\varepsilon} (L,Z) = (N,Z\cup Z)$, where for all $\aleph\in Z$,

$$N(\aleph)=\begin{cases} F'(\aleph), & \aleph\in Z-Z=\emptyset \\ L'(\aleph), & \aleph\in Z-Z=\emptyset \\ F'(\aleph)\cup L'(\aleph), & \aleph\in Z\cap Z=Z \end{cases}$$

Hence,

$$N(\aleph)=\begin{cases} F'(\aleph), & \aleph\in Z-Z=\emptyset \\ L'(\aleph), & \aleph\in Z-Z=\emptyset \\ F'(\aleph)\cup(G(\aleph)\cap H(\aleph)), & \aleph\in Z\cap Z=Z \end{cases}$$

It is seen that $M\neq N$. That is, in the set $S_z(U)$, $\overset{*}{}_{*_\varepsilon}$ does not have associative property, where Z is a fixed subset of E.

4) $(F,Z) \overset{*}{}_{*_\varepsilon} (G,C)=(G,C) \overset{*}{}_{*_\varepsilon} (F,Z)$.

Proof: Firstly, we observe that the parameter set of the soft set on both sides of the equation is $Z\cup C$, and thus the first condition of the soft equality is satisfied. Now let us look at the LHS. Let $(F,Z) \overset{*}{}_{*_\varepsilon} (G,C)=(H,Z\cup C)$, where for all $\aleph\in Z\cup C$,

$$H(\aleph)=\begin{cases} F'(\aleph), & \aleph\in Z-C \\ G'(\aleph), & \aleph\in C-Z \\ F'(\aleph)\cup G'(\aleph), & \aleph\in Z\cap C \end{cases}$$

Now let's handle the RHS. Assume that $(G,C) \overset{*}{}_{*_\varepsilon} (F,Z)=(T,C\cup Z)$, where for all $\aleph\in C\cup Z$,

$$T(\aleph)=\begin{cases} G'(\aleph), & \aleph\in C-Z \\ F'(\aleph), & \aleph\in Z-C \\ G'(\aleph)\cup F'(\aleph), & \aleph\in C\cap Z \end{cases}$$

Thus, it is seen that $H=T$. Similarly, it is easily seen that $(F,Z) \overset{*}{}_{*_\varepsilon} (G,Z)= (G,Z) \overset{*}{}_{*_\varepsilon} (F,Z)$. That is, $\overset{*}{}_{*_\varepsilon}$ operation is not commutative in both $S_E(U)$ and $S_Z(U)$.

5) $(F,Z) \overset{*}{}_{*_\varepsilon} (F,Z)=(F,Z)^r$.

***Proof*:** Let $(F,Z) \overset{*}{}_{*_\varepsilon} (F,Z)=(H,Z\cup Z)$, where for all $\aleph\in Z$,

$$H(\aleph)=\begin{cases} F'(\aleph), & \aleph\in Z-Z=\emptyset \\ F'(\aleph), & \aleph\in Z-Z=\emptyset \\ F'(\aleph)\cup F'(\aleph), & \aleph\in Z\cap Z=Z \end{cases}$$

Hence, for all $\aleph\in Z$, $H(\aleph)=F'(\aleph)\cup F'(\aleph)=F'(\aleph)$, and so $(H,Z)= (F,Z)^r$ That is, $\overset{*}{}_{*_\varepsilon}$ is not idempotent in $S_E(U)$.

6) $(F,Z) \overset{*}{}_{*_\varepsilon} \emptyset_Z=\emptyset_Z \overset{*}{}_{*_\varepsilon} (F,Z)= U_Z$.

***Proof*:** Let $\emptyset_Z=(T,Z)$. Thus, for all $\aleph\in Z$, $T(\aleph)=\emptyset$. Let $(F,Z) \overset{*}{}_{*_\varepsilon} (T,Z) =(H,Z\cup Z)$, where for all $\aleph\in Z$,

$$H(\aleph)=\begin{cases} F'(\aleph), & \aleph\in Z-Z=\emptyset \\ T'(\aleph), & \aleph\in Z-Z=\emptyset \\ F'(\aleph)\cup T'(\aleph), & \aleph\in Z\cap Z=Z \end{cases}$$

Hence, for all $\aleph\in Z$, $H(\aleph)= F'(\aleph)\cup T'(\aleph)= F'(\aleph)\cup U= U$ and so $(H,Z)= U_Z$.

7) $(F,Z) \overset{*}{}_{*_\varepsilon} \emptyset_E=\emptyset_E \overset{*}{}_{*_\varepsilon} (F,Z) =U_E$.

***Proof*:** Let $\emptyset_E =(S,E)$. Thus, for all $\aleph\in E$, $S(\aleph)= \emptyset$. Let $(F,Z) \overset{*}{}_{*_\varepsilon} (S,E)=(H,Z\cup E)$, where for all $\aleph\in E$,

$$H(\aleph)=\begin{cases} F'(\aleph), & \aleph\in Z-E=\emptyset \\ S'(\aleph), & \aleph\in E-Z=Z' \\ F'(\aleph)\cup S'(\aleph), & \aleph\in Z\cap E=Z \end{cases}$$

Hence, for all $\aleph\in Z$, $H(\aleph)= F'(\aleph)\cup S'(\aleph)=F'(\aleph)\cup U=U$. Thus,

$$H(\aleph)=\begin{cases} F'(\aleph), & \aleph\in Z-E=\emptyset \\ U, & \aleph\in E-Z=Z' \\ U, & \aleph\in Z\cap E=Z \end{cases}$$

Thus, $(H,Z)= U_E$.

8) $(F,Z) \overset{*}{}_{*_\varepsilon} \emptyset_\emptyset= \emptyset_\emptyset \overset{*}{}_{*_\varepsilon} (F,Z) = (F,Z)^r$

***Proof*:** Let $\emptyset_\emptyset= (K, \emptyset)$ and $(F,Z) \overset{*}{}_{*_\varepsilon} (K, \emptyset) = (Q,Z \cup \emptyset) = (Q,Z)$, where for all $\aleph\in Z$,

$$Q(\aleph)=\begin{cases} F'(\aleph), & \aleph\in Z-\emptyset=Z \\ K'(\aleph), & \aleph\in \emptyset-Z=\emptyset \\ F'(\aleph)\cup K'(\aleph), & \aleph\in Z\cap\emptyset=\emptyset \end{cases}$$

Hence, for all $\aleph\in Z$, $Q(\aleph)= F'(\aleph)$ and thus $(Q,Z) = (F,Z)^r$. Similarly, let $\emptyset_\emptyset \overset{*}{}_{*_\varepsilon} (F,Z)= (W, \emptyset \cup Z) = (W,Z)$, where for all $\aleph\in Z$,

$$W(\aleph)=\begin{cases} K'(\aleph), & \aleph\in \emptyset-Z=\emptyset \\ F'(\aleph), & \aleph\in Z-\emptyset=Z \\ K'(\aleph)\cup F'(\aleph), & \aleph\in \emptyset\cap Z=\emptyset \end{cases}$$

Hence, for all $\aleph\in Z$, $W(\aleph)= F'(\aleph)$, and thus $(W,Z) = (F,Z)^r$.

9) $(F,Z) \overset{*}{}_{*_\varepsilon} U_Z=U_Z \overset{*}{}_{*_\varepsilon} (F,Z)= (F, Z)^r$.

***Proof*:** Let $U_Z =(H,Z)$, where for all $\aleph\in Z$, $H(\aleph)=U$. Let $(F,Z) \overset{*}{}_{*_\varepsilon} (H,Z)=(T,Z\cup Z)$ where for all $\aleph\in Z$,

$$T(\aleph)=\begin{cases} F'(\aleph), & \aleph\in Z-Z=\emptyset \\ H'(\aleph), & \aleph\in Z-Z=\emptyset \\ F'(\aleph)\cup H'(\aleph), & \aleph\in Z\cap Z=Z \end{cases}$$

Here for all $\aleph\in Z$, $T(\aleph)= F'(\aleph)\cup H'(\aleph)= F'(\aleph) \cup \emptyset=F'(\aleph)$, and thus $(T,Z)= (F, Z)^r$. Similarly, let $U_Z \overset{*}{}_{*_\varepsilon} (F,Z)= (W, Z \cup Z) = (W,Z)$, where for all $\aleph\in Z$,

$$W(\aleph)=\begin{cases} H'(\aleph), & \aleph\in Z-Z=\emptyset \\ F'(\aleph), & \aleph\in Z-Z=\emptyset \\ H'(\aleph)\cup F'(\aleph), & \aleph\in Z\cap Z=Z \end{cases}$$

Here for all $\aleph\in Z$, $W(\aleph)= H'(\aleph)\cup F'(\aleph)=\emptyset) \cup F'(\aleph) =F'(\aleph)$, and thus $(W,Z)= (F, Z)^r$.

10) $(F,Z) \overset{*}{}_{*_\varepsilon}(F,Z)^r = (F,Z)^r \overset{*}{}_{*_\varepsilon}(F,Z)= U_Z$.

***Proof*:** Let $(F,Z)^r =(H,Z)$, where for all $\aleph\in Z$, $H(\aleph)=F'(\aleph)$. Let $(F,Z) \overset{*}{}_{*_\varepsilon}(H,Z)=(T,Z\cup Z)$ where for all $\aleph\in Z$,

$$T(\aleph)=\begin{cases} F'(\aleph), & \aleph\in Z-Z=\emptyset \\ H'(\aleph), & \aleph\in Z-Z=\emptyset \\ F'(\aleph)\cup H'(\aleph), & \aleph\in Z\cap Z=Z \end{cases}$$

Here for all $\aleph\in Z$, $T(\aleph)= F'(\aleph)\cup H'(\aleph)= F'(\aleph)\ UF(\aleph)=U$, and thus $(T,Z)= U_Z$.

11) $[(F,Z) \overset{*}{}_{*_\varepsilon}(G,C)]^r =(F,Z) \cap_\varepsilon(G,C)$.

***Proof*:** Let $(F,Z) \overset{*}{}_{*_\varepsilon} (G,C)=(H,Z\cup C)$, where for all $\aleph\in Z\cup C$,

$$H(\aleph)=\begin{cases} F'(\aleph), & \aleph\in Z-C \\ G'(\aleph), & \aleph\in C-Z \\ F'(\aleph)\cup G'(\aleph), & \aleph\in Z\cap C \end{cases}$$

Let $(H,Z\cup C)^r =(T,Z\cup C)$, where for all $\aleph\in Z\cup C$,

$$T(\aleph)=\begin{cases} F(\aleph), & \aleph\in Z-C \\ G(\aleph), & \aleph\in C-Z \\ F(\aleph)\cap G(\aleph), & \aleph\in Z\cap C \end{cases}$$

Hence, $(T,Z\cup C) =(F,Z) \cap_\varepsilon(G,C)$.

12) $(F,Z) \overset{*}{}_{*_\varepsilon}(G,C)= \emptyset_{Z\cup C} \Leftrightarrow (F,Z) = U_Z$ and $(G,C) = U_C$.

Proof: Let $(F,Z) \overset{*}{}_{*_\varepsilon}(G,C) =$ (T,Z∪C). Here, for all $\aleph\in Z\cup C$,

$$T(\aleph)=\begin{cases} F'(\aleph), & \aleph\in Z-C \\ G'(\aleph), & \aleph\in C-Z \\ F'(\aleph)\cup G'(\aleph), & \aleph\in Z\cap C \end{cases}$$

Since $(T,Z\cup C)= \emptyset_{Z\cup C}, T(\aleph)=\emptyset$ for all $\aleph\in Z\cup C$. Hence, for all $\aleph\in Z-C$, $F'(\aleph)=\emptyset$; for all $\aleph\in C-Z$, $G'(\aleph)=\emptyset$ and for all $\aleph\in Z\cap C$, $F'(\aleph)\cup G'(\aleph)= \emptyset$. Thus, for all $\aleph \in Z - C$, $F(\aleph)=U$, for all $\aleph \in C - Z$, $G(\aleph)=U$, for all $\aleph \in Z \cap C, F'(\aleph) = \emptyset$, $G'(\aleph) = \emptyset$. Thus, for all $\aleph \in Z \cap C, F(\aleph) = U$, $G(\aleph) = U$. Thus, for all $\aleph\in Z$, $F(\aleph)=U$ and for all $\aleph\in C$, $G(\aleph)=U$. Thus, $(F, Z) = U_Z$ and $(G, C) = U_C$.

13) $\emptyset_Z \tilde{\subseteq}(F,Z) \overset{*}{}_{*_\varepsilon}(G,C)$, $\emptyset_C \tilde{\subseteq}(F,Z) \overset{*}{}_{*_\varepsilon}(G,C)$, $\emptyset_{Z\cup C} \tilde{\subseteq}(F,Z) \overset{*}{}_{*_\varepsilon}(G,C)$, $(F,Z) \overset{*}{}_{*_\varepsilon}(G,C) \tilde{\subseteq} U_{Z\cup C}$.

14) $(F,Z) \overset{r}{\tilde{\subseteq}} (F,Z) \overset{*}{}_{*_\varepsilon}(G,C)$ and $(G,C) \overset{r}{\tilde{\subseteq}} (F,Z) \overset{*}{}_{*_\varepsilon}(G,C)$.

***Proof*:** Let $(F,Z) \overset{*}{}_{*_\varepsilon}(G,C)=(H, Z \cup C)$ where $Z\subseteq Z \cup C$ and for all $\aleph\in Z\cup C$,

$$H(\aleph)=\begin{cases} F'(\aleph), & \aleph\in Z-C \\ G'(\aleph), & \aleph\in C-Z \\ F'(\aleph)\cup G'(\aleph), & \aleph\in Z\cap C \end{cases}$$

Here, for all $\aleph\in Z-C$, $F'(\aleph)\subseteq F'(\aleph)=H(\aleph)$ and for all $\aleph\in Z\cap C$, $F'(\aleph)\subseteq F'(\aleph)\cup G'(\aleph)=H(\aleph)$. Thus for all $\aleph\in Z$, $F'(\aleph)\subseteq H(\aleph)$. So $(F,Z)\ {}^{r}\widetilde{\subseteq}(F,Z)\ \overset{*}{}_{*_\varepsilon}(G,C)$. Similarly, for all $\aleph\in C-Z$, $G'(\aleph)\subseteq G'(\aleph)=H(\aleph)$ and for all $\aleph\in C\cap Z$, $G'(\aleph)\subseteq F'(\aleph)\cup G'(\aleph)=H(\aleph)$. Thus for all $\aleph\in C$, $G'(\aleph)\subseteq H(\aleph)$. So $(G,C)^{r}\widetilde{\subseteq}(F,Z)\ \overset{*}{}_{*_\varepsilon}(G,C)$.

15) If $(F,Z)\ \widetilde{\subseteq}\ (G,Z)$ then $(F,Z)\ \overset{*}{}_{*_\varepsilon}(G,Z)=(F,Z)^{r}$.

***Proof*:** Let $(F,Z)\widetilde{\subseteq}\ (G,Z)$. Then, for all $\aleph\in Z$, $F(\aleph)\subseteq G(\aleph)$. Let $(F,Z)\ \overset{*}{}_{*_\varepsilon}(G,Z)=(H,Z\cup Z)$, where for all $\aleph\in Z$,

$$H(\aleph)=\begin{cases} F'(\aleph), & \aleph\in Z-Z=\emptyset \\ G'(\aleph), & \aleph\in Z-Z=\emptyset \\ F'(\aleph)\cup G'(\aleph), & \aleph\in Z\cap Z=Z \end{cases}$$

Hence, $F(\aleph)\subseteq G(\aleph)$ for all $\aleph\in Z$ and so $G'(\aleph)\subseteq F'(\aleph)$. Thus, for all $\aleph\in Z$, $H(\aleph)=F'(\aleph)\cup G'(\aleph)=F'(\aleph)$. Therefore, $(F,Z)\ \overset{*}{}_{*_\varepsilon}(G,Z)=(F,Z)^{r}$.

16) If $(F,Z)\ \widetilde{\subseteq}(G,Z)$, then $(G,Z)\ \overset{*}{}_{*_\varepsilon}(H,C)\ \widetilde{\subseteq}\ (F,Z)\ \overset{*}{}_{*_\varepsilon}(H,C)$.

***Proof*:** Let $(F,Z)\ \widetilde{\subseteq}\ (G,Z)$. Then, $F(\aleph)\subseteq G(\aleph)$ for all $\aleph\in Z$, and so $G'(\aleph)\subseteq F'(\aleph)$. Let $(G,Z)\ \overset{*}{}_{*_\varepsilon}(H,C)=(W,Z\cup C)$ where for all $\aleph\in Z\cup C$,

$$W(\aleph)=\begin{cases} G'(\aleph), & \aleph\in Z-C \\ H'(\aleph), & \aleph\in C-Z \\ G'(\aleph)\cup H'(\aleph), & \aleph\in Z\cap C \end{cases}$$

Let $(F,Z)\ \overset{*}{}_{*_\varepsilon}(H,C)=(L,Z\cup C)$, where for all $\aleph\in Z\cup C$,

$$L(\aleph)=\begin{cases} F'(\aleph), & \aleph\in Z-C \\ H'(\aleph), & \aleph\in C-Z \\ F'(\aleph)\cup H'(\aleph), & \aleph\in Z\cap C \end{cases}$$

Thus, $W(\aleph)=G'(\aleph)\subseteq G'(\aleph)=L(\aleph)$ for all $\aleph\in Z-C$; $W(\aleph)=H'(\aleph)\subseteq H'(\aleph)=L(\aleph)$ for all $\aleph\in C-Z$; $W(\aleph)=G'(\aleph)\cup H'(\aleph)\subseteq F'(\aleph)\cup H'(\aleph)=L(\aleph)$ for all $\aleph\in Z\cap C$. Thus, $(G,Z)\ \overset{*}{}_{*_\varepsilon}(H,C)\ \widetilde{\subseteq}\ (F,Z)\ \overset{*}{}_{*_\varepsilon}(H,C)$.

17) If $(G,Z)\ \overset{*}{}_{*_\varepsilon}(H,C)\ \widetilde{\subseteq}\ (F,Z)\ \overset{*}{}_{*_\varepsilon}(H,C)$, then $(F,Z)\widetilde{\subseteq}(G,Z)$ need not to hold. That is, the converse of Theorem 3.3. (16) is not true.

***Proof*:** Let us give an example to show that the converse of Theorem 3.3. (16) is not true. Let $E=\{e_1,e_2,e_3,e_4,e_5\}$ be the parameter set, $A=\{e_1,e_3\}$, $C=\{e_1,e_3,e_5\}$ be the subset of E, and $U=\{h_1,h_2,h_3,h_4,h_5\}$ be the universal set.

Let $(F,Z)=\{(e_1,\{h_2,h_5\}),(e_3,\{h_1,h_2,h_5\})\}$,$(G,Z)=\{(e_1,\{h_2\}),(e_3,\{h_1,h_2\})\}$, $H,C)=\{(e_1,\emptyset),(e_3,\emptyset),(e_5,\{h_2,h_3,h_4\})\}$ be soft sets over U. Let $(G,Z)\ \overset{*}{}_{*_\varepsilon}(H,C)=(L,Z\cup C)$, then $(L,Z\cup C)=(L,Z\cup C)=\{(e_1,U),(e_3,U),(e_5,\{h_1,h_5\})\}$ and let $(F,Z)\ \overset{*}{}_{*_\varepsilon}(H,C)=(K,Z\cup C)$, thus $(K,Z\cup C)=\{(K,Z\cup C)=\{(e_1,U),(e_3,U),(e_5,\{h_1,h_5\})\}$. Hence, $(G,Z)\ \overset{*}{}_{*_\varepsilon}(H,C)\ \widetilde{\subseteq}\ (F,Z)\ \overset{*}{}_{*_\varepsilon}(H,C)$ but (F,Z) is not a soft subnset of (G,Z).

18) If (F,Z) $\tilde{\subseteq}$ (G, Z) and (K,C) $\tilde{\subseteq}$ (L, C), then (G,Z) $\overset{*}{}_{*_\varepsilon}$(L,C) $\tilde{\subseteq}$(F,Z) $\overset{*}{}_{*_\varepsilon}$(K,C).

***Proof*:** Let (F,Z)$\tilde{\subseteq}$ (G, Z) and (K,C) $\tilde{\subseteq}$ (L, C). Hence, Z⊆C and for all א∈Z, F(א)⊆ G(א) and G'(א)⊆ F′(א) and for all א∈C, K(א)⊆ L(א) and L'(א)⊆ K′(א) Let (G,Z) $\overset{*}{}_{*_\varepsilon}$(L, C) = (W,Z∪C). Thus, for all א∈ Z∪C,

$$W(א)=\begin{cases} G'(א), & א\in Z-C \\ L'(א), & א\in C-Z \\ G'(א)\cup L'(א), & א\in Z\cap C \end{cases}$$

Let (F,Z) $\overset{*}{}_{*_\varepsilon}$(K, C) = (S,Z∪C). Thus, for all א∈Z∪C,

$$S(א)=\begin{cases} F'(א), & א\in Z-C \\ K'(א), & א\in C-Z \\ F'(א)\cup K'(א), & א\in Z\cap C \end{cases}$$

Hence, since for all א∈ Z-C, W(א)=G'(א)⊆F'(א)=S(א),for all א∈ C-Z, W(א)=L'(א)⊆K'(א)=S(א),for all א∈ Z∩C, W(א)=G'(א)∪L'(א) ⊆ F'(א)∪K'(א)=S(א) , (G, Z) $\overset{*}{}_{*_\varepsilon}$(L, C) $\tilde{\subseteq}$ (F, Z) $\overset{*}{}_{*_\varepsilon}$(K, C).

Theorem 3.4. The complementary extended star operation has the following distributions over other soft set operations:

Theorem 3.4.1. The complementary extended star operation has the following distributions over restricted soft set operations:

i) LHS Distributions of the Complementary Extended Star Operation on Restricted Soft Set Operations:

1) If Z'∩C∩R= Z∩C∩R=∅ then (F,Z)$\overset{*}{}_{*_\varepsilon}$ [(G,C)∩$_R$(H,R)]=[(F,Z)$\overset{*}{}_{*_\varepsilon}$ (G,C)]∩$_R$[(F,Z)$\overset{*}{}_{*_\varepsilon}$(H,R)].

Proof: Consider the LHS first. Let (G,C)∩$_R$(H,R)=(M,C∩R), where for all א∈C∩R, M(א) = G(א) ∩ H(א). Let (F,Z)$\overset{*}{}_{*_\varepsilon}$ (M,C∩R)=(N,Z∪(C∩R)), where for all א∈Z∪(C∩R),

$$N(א)=\begin{cases} F'(א), & א\in Z-(C\cap R) \\ M'(א), & א\in (C\cap R)-Z \\ F'(א)\cup M'(א), & א\in Z\cap (C\cap R) \end{cases}$$

Thus,

$$N(א)=\begin{cases} F'(א), & א\in Z-(C\cap R)=Z-(C\cap R) \\ G'(א)\cup H'(א), & א\in (C\cap R)-Z=Z'\cap C\cap R \\ F'(א)\cup (G'(א)\cup H'(א)), & א\in Z\cap (C\cap R)=Z\cap C\cap R \end{cases}$$

Now let',s handle the RHS i.e. [(F,Z)$\overset{*}{}_{*_\varepsilon}$ (G,C)]∩$_R$[(F,Z)$\overset{*}{}_{*_\varepsilon}$ (H,R)]. Let (F,Z)$\overset{*}{}_{*_\varepsilon}$ (G,C)=(V,Z∪C), where for all א∈Z∪C,

$$V(א)=\begin{cases} F'(א), & א\in Z-C \\ G'(א), & א\in C-Z \\ F'(א)\cup G'(א), & א\in Z\cap C \end{cases}$$

Assume that (F,Z) $\overset{*}{}_{*_\varepsilon}$ (H,R)=(W,Z∪R), where for all א∈Z∪R,

$$W(א)=\begin{cases} F'(א), & א\in Z-R \\ H'(א), & א\in R-Z \\ F'(א)\cup H'(א), & א\in Z\cap R \end{cases}$$

Let $(V,Z\cup C)\cap_R(W,Z\cup R)=(T,(Z\cup C)\cap(Z\cup R)))$, where for all $\aleph\in Z\cup(C\cap R)$, $T(\aleph)=V(\aleph)\cap W(\aleph)$. Hence,

$$T(\aleph)=\begin{cases} F'(\aleph)\cap F'(\aleph), & \aleph\in(Z\text{-}C)\cap(Z\text{-}R)=Z\cap C'\cap R' \\ F'(\aleph)\cap H'(\aleph), & \aleph\in(Z\text{-}C)\cap(R\text{-}Z)=\emptyset \\ F'(\aleph)\cap(F'(\aleph)\cup H'(\aleph)) & \aleph\in(Z\text{-}C)\cap(Z\cap R)=Z\cap C'\cap R \\ G'(\aleph)\cap F'(\aleph), & \aleph\in(C\text{-}Z)\cap(Z\text{-}R)=\emptyset \\ G'(\aleph)\cap H'(\aleph), & \aleph\in(C\text{-}Z)\cap(R\text{-}Z)=Z'\cap C\cap R \\ G'(\aleph)\cap\left(F'(\aleph)\cup H'(\aleph)\right), & \aleph\in(C\text{-}Z)\cap(Z\cap R)=\emptyset \\ (F'(\aleph)\cup G'(\aleph))\cap F'(\aleph), & \aleph\in(Z\cap C)\cap(Z\text{-}R)=Z\cap C\cap R' \\ (F'(\aleph)\cup G'(\aleph))\cap H'(\aleph), & \aleph\in(Z\cap C)\cap(R\text{-}Z)=\emptyset \\ (F'(\aleph)\cup G'(\aleph))\cap(F'(\aleph)\cup H'(\aleph)), & \aleph\in(Z\cap C)\cap(Z\cap R)=Z\cap C\cap R \end{cases}$$

Thus,

$$T(\aleph)=\begin{cases} F'(\aleph), & \aleph\in(Z\text{-}C)\cap(Z\text{-}R)=Z\cap C'\cap R' \\ F'(\aleph) & \aleph\in(Z\text{-}C)\cap(Z\cap R)=Z\cap C'\cap R \\ G'(\aleph)\cap H'(\aleph), & \aleph\in(C\text{-}Z)\cap(R\text{-}Z)=Z'\cap C\cap R \\ F'(\aleph) & \aleph\in(Z\cap C)\cap(Z\text{-}R)=Z\cap C\cap R' \\ (F'(\aleph)\cup G'(\aleph))\cap(F'(\aleph)\cup H'(\aleph)), & \aleph\in(Z\cap C)\cap(Z\cap R)=Z\cap C\cap R \end{cases}$$

Here, when considering $Z\text{-}(C\cap R)$ in the function N, since $Z\text{-}(C\cap R)=Z\cap(C\cap R)'$, if an element is in the complement of $(C\cap R)$, it is either in C-R, in R-C, or in $(C\cup R)'$. Thus, if $\aleph\in Z\text{-}(C\cap R)$, then $\aleph\in Z\cap C\cap R'$ or $\aleph\in Z\cap C'\cap R$ or $\aleph\in Z\cap C'\cap R'$. Thus, N=T under the condition $Z'\cap C\cap R=\emptyset$.

2) $(F,Z)^*_{*_\varepsilon}[(G,C)\cup_R(H,R)]=[(F,Z)^*_{*_\varepsilon}(G,C)]\cap_R[(F,Z)^*_{*_\varepsilon}(H,R)]$.

3) If $Z'\cap C\cap R=Z\cap C\cap R=\emptyset$ then $(F,Z)^*_{*_\varepsilon}[(G,C)*_R(H,R)]=[(F,Z)^*_{+_\varepsilon}(G,C)]\cap_R[(F,Z)^*_{+_\varepsilon}(H,R)]$.

4) If $Z'\cap C\cap R=Z\cap C\cap R=\emptyset$ then $(F,Z)^*_{*_\varepsilon}[(G,C)\theta_R(H,R)]=[(F,Z)^*_{+_\varepsilon}(G,C)]\cap_R[(F,Z)^*_{+_\varepsilon}(H,R)]$.

ii) RHS Distribution of Complementary Extended Star Operation on Restricted Soft Set Operations

1) $[(F,Z)\cup_R(G,C)]^*_{*_\varepsilon}(H,R)=[(F,Z)^*_{*_\varepsilon}(H,R)]\cap_R[(G,C)^*_{*_\varepsilon}(H,R)]$.

Proof: Consider the LHS first. Let $(F,Z)\cup_R(G,C)=(M,Z\cap C)$, where for all $\aleph\in Z\cap C$, $M(\aleph)=F(\aleph)\cup G(\aleph)$. Let $(M,Z\cap C)^*_{*_\varepsilon}(H,R)=(N,(Z\cap C)UR))$, where $\aleph\in(Z\cap C)UR$,

$$N(\aleph)=\begin{cases} M'(\aleph), & \aleph\in(Z\cap C)\text{-}R \\ H'(\aleph), & \aleph\in R\text{-}(Z\cap C) \\ M'(\aleph)\cup H'(\aleph), & \aleph\in Z\cap(C\cap R) \end{cases}$$

Thus,

$$N(\aleph)=\begin{cases} F'(\aleph)\cap G'(\aleph), & \aleph\in(Z\cap C)\text{-}R=Z\cap C\cap R' \\ H'(\aleph), & \aleph\in R\text{-}(Z\cap C)=R\text{-}(Z\cap C) \\ (F'(\aleph)\cap G'(\aleph))\cup H'(\aleph), & \aleph\in Z\cap(C\cap R)=Z\cap C\cap R \end{cases}$$

Now consider the RHS. i.e. $[(F,Z)^*_{*_\varepsilon}(H,R)]\cap_R[(G,C)^*_{*_\varepsilon}(H,R)]$. Let $(F,Z)^*_{*_\varepsilon}(H,R)=(V,Z\cup R)$, where for all $\aleph\in Z\cup R$,

$$V(\aleph)=\begin{cases} F'(\aleph), & \aleph\in Z-R \\ H'(\aleph), & \aleph\in R-Z \\ F'(\aleph)\cup H'(\aleph), & \aleph\in Z\cap R \end{cases}$$

Now, let $(G,C)\overset{*}{}_{*_\varepsilon}(H,R)=(W, C\cup R)$, where for all $\aleph\in C\cup R$,

$$W(\aleph)=\begin{cases} G'(\aleph), & \aleph\in C-R \\ H'(\aleph), & \aleph\in R-C \\ G'(\aleph)\cup H'(\aleph), & \aleph\in C\cap R \end{cases}$$

Let $(V,Z\cup R)\cap_R(W,C\cup R)=(T,(Z\cup R)\cap (C\cup R))$. Here, for all $\aleph\in(Z\cap C)\cup R$, $T(\aleph)=V(\aleph)\cap W(\aleph)$.Thus,

$$T(\aleph)=\begin{cases} F'(\aleph)\cap G'(\aleph), & \aleph\in(Z-R)\cap(C-R)=Z\cap C\cap R' \\ F'(\aleph)\cap H'(\aleph), & \aleph\in(Z-R)\cap(R-C)=\emptyset \\ F'(\aleph)\cap\big(G'(\aleph)\cup H'(\aleph)\big), & \aleph\in(Z-R)\cap(C\cap R)=\emptyset \\ H'(\aleph)\cap G'(\aleph), & \aleph\in(R-Z)\cap(C-R)=\emptyset \\ H'(\aleph)\cap H'(\aleph), & \aleph\in(R-Z)\cap(R-C)=Z'\cap C'\cap R \\ H'(\aleph)\cap(G'(\aleph)\cup H'(\aleph)), & \aleph\in(R-Z)\cap(C\cap R)=Z'\cap C\cap R \\ \big(F'(\aleph)\cup H'(\aleph)\big)\cap G'(\aleph), & \aleph\in(Z\cap R)\cap(C-R)=\emptyset \\ \big(F'(\aleph)\cup H'(\aleph)\big)\cap H'(\aleph) & \aleph\in(Z\cap R)\cap(R-C)=Z\cap C'\cap R \\ (F'(\aleph)\cup H'(\aleph))\cap(G'(\aleph)\cup H'(\aleph)), & \aleph\in(Z\cap C)\cap(Z\cap R)=Z\cap C\cap R \end{cases}$$

Thus,

$$T(\aleph)=\begin{cases} F'(\aleph)\cap G'(\aleph), & \aleph\in(Z-R)\cap(C-R)=Z\cap C\cap R' \\ H'(\aleph) & \aleph\in(R-Z)\cap(R-C)=Z'\cap C'\cap R \\ H'(\aleph), & \aleph\in(R-Z)\cap(C\cap R)=Z'\cap C\cap R \\ H'(\aleph), & \aleph\in(Z\cap R)\cap(R-C)=Z\cap C'\cap R \\ (F'(\aleph)\cup H(\aleph))\cap(G'(\aleph)\cup H(\aleph)), & \aleph\in(Z\cap C)\cap(Z\cap R)=Z\cap C\cap R \end{cases}$$

Here, if we consider $R-(Z\cap C)$ in the function N, since $R-(Z\cap C)=R\cap(Z\cap C)'$, if an element is in the complement of $(Z\cap C)$, it is either in Z-C, in C-Z, or in $(Z\cup C)'$. Thus, if $\aleph\in R-(Z\cap C)$, $\aleph\in R\cap Z\cap C'$ or $\aleph\in R\cap Z'\cap C$ or $\aleph\in R\cap Z'\cap C'$. Hence, $N=T$ is satisfied under the condition $Z'\cap C\cap R=Z\cap C'\cap R=\emptyset$. It is obvious that the condition $Z'\cap C\cap R=Z\cap C'\cap R=\emptyset$ implies that $(Z\Delta C)\cap R=\emptyset$

2) If $Z\cap C\cap R'=Z\cap C\cap R=\emptyset$,then $[(F,Z)\cap_R(G,C)]\overset{*}{}_{*_\varepsilon}(H,R)=[(F,Z)\overset{*}{}_{*_\varepsilon}(H,R)]\cap_R[(G,C)\overset{*}{}_{*_\varepsilon}(H,R)]$.

3) If $Z\cap C\cap R'=\emptyset$, then $[(F,Z)*_R(G,C)]\overset{*}{}_{*_\varepsilon}(H,R)=[(F,Z)\overset{*}{}_{\lambda_\varepsilon}(H,R)]\cap_R[(G,C)\overset{*}{}_{\lambda_\varepsilon}(H,R)]$.

4) If $Z\cap C\cap R'=Z\cap C\cap R=\emptyset$, then $[(F,Z)\theta_R(G,C)]\overset{*}{}_{*_\varepsilon}(H,R)=[(F,Z)\overset{*}{}_{\lambda_\varepsilon}(H,R)]\cap_R[(G,C)\overset{*}{}_{\lambda_\varepsilon}(H,R)]$.

Theorem 3.4.2. The following distributions of the complementary extended star operation over extended soft set operations hold:

i)LHS Distributions of the Complementary Extended Star Operation on Extended Soft Set Operations

1)If $(Z\Delta C)\cap R=Z\cap C\cap R'=\emptyset$, then $(F,Z)\overset{*}{}_{*_\varepsilon}[(G,C)*_\varepsilon(H,R)]=[(F,Z)\overset{*}{}_{+_\varepsilon}(G,C)]\cap_\varepsilon[(F,ZR\overset{*}{}_{+_\varepsilon}(H,R)]$.

Proof: Consider first LHS. Let $(G,C)*_\varepsilon(H,R)=(M,C\cup R)$, where for all $\aleph\in C\cup R$,

$$M(\aleph)=\begin{cases} G(\aleph), & \aleph\in C-R \\ H(\aleph), & \aleph\in R-C \\ G'(\aleph)\cup H'(\aleph), & \aleph\in C\cap R \end{cases}$$

Let $(F,Z)\overset{*}{}_{*_\varepsilon}(M,C\cup R)=(N,Z\cup(C\cup R))$, where for all $\aleph\in Z\cup C\cup R$,

$$N(\aleph)=\begin{cases} F'(\aleph), & \aleph\in Z-(C\cup R) \\ M'(\aleph), & \aleph\in(C\cup R)-Z \\ F'(\aleph)\cup M'(\aleph), & \aleph\in Z\cap(C\cup R) \end{cases}$$

Thus,

$$N(\aleph)=\begin{cases} F'(\aleph), & \aleph\in Z-(C\cup R)=Z\cap C'\cap R' \\ G'(\aleph), & \aleph\in(C-R)-Z=Z'\cap C\cap R' \\ H'(\aleph), & \aleph\in(R-C)-Z=Z\cap C'\cap R \\ G(\aleph)\cap H(\aleph), & \aleph\in(C\cap R)-Z=Z'\cap C\cap R \\ F'(\aleph)\cup G'(\aleph), & \aleph\in Z\cap(C-R)=Z\cap C\cap R' \\ F'(\aleph)\cup H'(\aleph), & \aleph\in Z\cap(R-C)=Z\cap C'\cap R \\ F'(\aleph)\cup(G(\aleph)\cap H(\aleph)), & \aleph\in Z\cap(C\cap R)=Z\cap C\cap R \end{cases}$$

Now consider the RHS, i.e. $[(F,Z)\overset{*}{+}_{\varepsilon}(G,C)]\cap_{\varepsilon}[(F,Z)\overset{*}{+}_{\varepsilon}(H,R)]$. Let $(F,Z)\overset{*}{+}_{\varepsilon}(G,C)=(V,Z\cup C)$, where for all $\aleph\in Z\cup C$,

$$V(\aleph)=\begin{cases} F'(\aleph), & \aleph\in Z-C \\ G'(\aleph), & \aleph\in C-Z \\ F'(\aleph)\cup G(\aleph), & \aleph\in Z\cap C \end{cases}$$

Let $(F,Z)\overset{*}{+}_{\varepsilon}(H,R)=(W,Z\cup R)$, where for all $\aleph\in Z\cup R$,

$$W(\aleph)=\begin{cases} F'(\aleph), & \aleph\in Z-R \\ H'(\aleph), & \aleph\in R-Z \\ F'(\aleph)\cup H(\aleph), & \aleph\in Z\cap R \end{cases}$$

Let $(V,Z\cup C)\cap_{\varepsilon}(W,Z\cup R)=(T,(Z\cup C)\cup R)$, where for all $\aleph\in Z\cup C\cup R$,

$$T(\aleph)=\begin{cases} V(\aleph), & \aleph\in(Z\cup C)-(Z\cup R) \\ W(\aleph), & \aleph\in(Z\cup R)-(Z\cup C) \\ V(\aleph)\cap W(\aleph), & \aleph\in(Z\cup C)\cap(Z\cup R) \end{cases}$$

Thus,

$$T(\aleph)=\begin{cases} F'(\aleph), & \aleph\in(Z-C)-(Z\cup R)=\emptyset \\ G'(\aleph), & \aleph\in(C-Z)-(Z\cup R)=Z'\cap C\cap R' \\ F'(\aleph)\cup G(\aleph), & \aleph\in(Z\cap C)-(Z\cup R)=\emptyset \\ F'(\aleph), & \aleph\in(Z-R)-(Z\cup C)=\emptyset \\ H'(\aleph), & \aleph\in(R-Z)-(Z\cup C)=Z'\cap C\cap R \\ F'(\aleph)\cup H(\aleph), & \aleph\in(Z\cap R)-(Z\cup C)=\emptyset \\ F'(\aleph)\cap F'(\aleph), & \aleph\in(Z-C)\cap(Z-R)=Z\cap C'\cap R' \\ F'(\aleph)\cap H'(\aleph), & \aleph\in(Z-C)\cap(R-Z)=\emptyset \\ F'(\aleph)\cap(F'(\aleph)\cup H(\aleph)), & \aleph\in(Z-C)\cap(Z\cap R)=Z\cap C'\cap R \\ G'(\aleph)\cap F'(\aleph), & \aleph\in(C-Z)\cap(Z-R)=\emptyset \\ G'(\aleph)\cap H'(\aleph), & \aleph\in(C-Z)\cap(R-Z)=Z'\cap C\cap R \\ G'(\aleph)\cap(F'(\aleph)\cup H(\aleph)), & \aleph\in(C-Z)\cap(Z\cap R)=\emptyset \\ (F'(\aleph)\cup G(\aleph))\cap F'(\aleph), & \aleph\in(Z\cap C)\cap(Z-R)=Z\cap C\cap R' \\ (F'(\aleph)\cup G(\aleph))\cap H'(\aleph), & \aleph\in(Z\cap C)\cap(R-Z)=\emptyset \\ (F'(\aleph)\cup G(\aleph))\cap(F'(\aleph)\cup H(\aleph)), & \aleph\in(Z\cap C)\cap(Z\cap R)=Z\cap C\cap R \end{cases}$$

Hence,

$$T(\aleph)=\begin{cases} G'(\aleph), & \aleph\in(C-Z)-(Z\cup R)=Z'\cap C\cap R' \\ H'(\aleph), & \aleph\in(R-Z)-(Z\cup C)=Z'\cap C'\cap R \\ F'(\aleph), & \aleph\in(Z-C)\cap(Z-R)=Z\cap C'\cap R' \\ F'(\aleph)\cap H(\aleph) & \aleph\in(Z-C)\cap(Z\cap R)=Z\cap C'\cap R \\ G'(\aleph)\cap H'(\aleph), & \aleph\in(C-Z)\cap(R-Z)=Z'\cap C\cap R \\ F'(\aleph)\cap G(\aleph) & \aleph\in(Z\cap C)\cap(Z-R)=Z\cap C\cap R' \\ (F'(\aleph)\cup G(\aleph))\cap(F'(\aleph)\cup H(\aleph)), & \aleph\in(Z\cap C)\cap(Z\cap R)=Z\cap C\cap R \end{cases}$$

It is seen that N=T is satisfied under the condition Z'∩C∩R=Z∩C'∩R=Z∩C∩R'=∅. I is obvious that the condition Z'∩C∩R=Z∩C'∩R=∅ is equal to (ZΔC)∩R= ∅.

2) $(F,Z)\overset{*}{}_{*_\varepsilon}[(G,C)\cap_\varepsilon(H,R)]=[(F,Z)\overset{*}{}_{*_\varepsilon}(G,C)]\cup_\varepsilon[(F,Z)\overset{*}{}_{*_\varepsilon}(H,R)]$.

3) $Z\cap(C\Delta R)=\emptyset$, $(F,Z)\overset{*}{}_{*_\varepsilon}[(G,C)\cup_\varepsilon(H,R)]=[(F,Z)\overset{*}{}_{*_\varepsilon}(G,C)]\cap_\varepsilon[(F,Z)\overset{*}{}_{*_\varepsilon}(H,R)]$.

4) $(Z\Delta C)\cap R=Z\cap C\cap R'=\emptyset$, $(F,Z)\overset{*}{}_{*_\varepsilon}[(G,C)\theta_\varepsilon(H,R)]=[(F,Z)\overset{*}{}_{+_\varepsilon}(G,C)]\cup_\varepsilon[(F,Z)\overset{*}{}_{+_\varepsilon}(H,R)]$.

ii) RHS Distributions of Complementary Extended Star Operation over Extended Soft Set Operations

1)If $Z\cap C\cap R'=Z\cap C\cap R=\emptyset$, then $[(F,Z)\cup_\varepsilon(G,C)]\overset{*}{}_{*_\varepsilon}(H,R)=[(F,Z)\overset{*}{}_{*_\varepsilon}(H,R)]\cup_\varepsilon[(G,C)\overset{*}{}_{*_\varepsilon}(H,R)]$.

Proof: Consider first the LHS. Let $(F,Z)\cup_\varepsilon(G,C)=(M,Z\cup C)$, where for all $\aleph\in Z\cup C$,

$$M(\aleph)=\begin{cases} F(\aleph), & \aleph\in Z-C \\ G(\aleph), & \aleph\in C-Z \\ F(\aleph)\cup G(\aleph), & \aleph\in Z\cap C \end{cases}$$

Let $(M,Z\cup C)\overset{*}{}_{*_\varepsilon}(H,R)=(N,(Z\cup C)\cup R)$, where for all $\aleph\in Z\cup C\cup R$,

$$N(\aleph)=\begin{cases} M'(\aleph), & \aleph\in(Z\cup C)-R \\ H'(\aleph), & \aleph\in R-(Z\cup C) \\ M'(\aleph)\cup H'(\aleph), & \aleph\in(Z\cup C)\cap R \end{cases}$$

Thus,

$$N(\aleph)=\begin{cases} F'(\aleph), & \aleph\in(Z-C)-R=Z\cap C'\cap R' \\ G'(\aleph), & \aleph\in(C-Z)-R=Z'\cap C\cap R' \\ F'(\aleph)\cap G'(\aleph), & \aleph\in(Z\cap C)-R=Z\cap C\cap R' \\ H'(\aleph), & \aleph\in R-(Z\cup C)=Z'\cap C'\cap R \\ F'(\aleph)\cup H'(\aleph), & \aleph\in(Z-C)\cap R=Z\cap C'\cap R \\ G'(\aleph)\cup H'(\aleph), & \aleph\in(C-Z)\cap R=Z'\cap C\cap R \\ (F'(\aleph)\cap G'(\aleph))\cup H'(\aleph), & \aleph\in(Z\cap C)\cap R=Z\cap C\cap R \end{cases}$$

Now consider the RHS, i.e. $[(F,Z)\overset{*}{}_{*_\varepsilon}(H,R)]\cup_\varepsilon[(G,C)\overset{*}{}_{*_\varepsilon}(H,R)]$. Let $(F,Z)\overset{*}{}_{*_\varepsilon}(H,R)=(V,Z\cup R)$, where for all $\aleph\in Z\cup R$,

$$V(\aleph)=\begin{cases} F'(\aleph), & \aleph\in Z-R \\ H'(\aleph), & \aleph\in R-Z \\ F'(\aleph)\cup H'(\aleph) & \aleph\in Z\cap R \end{cases}$$

Let $(G,C)\overset{*}{}_{*_\varepsilon}(H,R)=(W,C\cup R)$, where for all $\aleph\in C\cup R$,

$$W(\aleph)=\begin{cases} G'(\aleph), & \aleph\in C\text{-}R \\ H'(\aleph), & \aleph\in R\text{-}C \\ G'(\aleph)\cup H'(\aleph), & \aleph\in C\cap R \end{cases}$$

Let $(V,Z\cup R)\ \cup_\varepsilon\ (W,C\cup R)=(T,Z\cup C\cup R)$, where for all $\aleph\in Z\cup C\cup R$,

$$T(\aleph)=\begin{cases} V(\aleph), & \aleph\in(Z\cup R)-(C\cup R) \\ W(\aleph), & \aleph\in(C\cup R)-(Z\cup R) \\ V(\aleph)\cup W(\aleph), & \aleph\in(Z\cup R)\cap(C\cup R) \end{cases}$$

Thus,

$$T(\aleph)=\begin{cases} F'(\aleph), & \aleph\in(Z\text{-}R)-(C\cup R)=Z\cap C'\cap R' \\ H'(\aleph), & \aleph\in(R\text{-}Z)-(C\cup R)=\emptyset \\ F'(\aleph)\cup H'(\aleph), & \aleph\in(Z\cap R)-(C\cup R)=\emptyset \\ G'(\aleph), & \aleph\in(C\text{-}R)-(Z\cup R)=Z'\cap C\cap R' \\ H'(\aleph), & \aleph\in(R\text{-}C)-(Z\cup R)=\emptyset \\ G'(\aleph)\cup H'(\aleph), & \aleph\in(C\cap R)-(Z\cup R)=\emptyset \\ F'(\aleph)\cup G'(\aleph), & \aleph\in(Z\text{-}R)\cap(C\text{-}R)=Z\cap C\cap R' \\ F'(\aleph)\cup H'(\aleph), & \aleph\in(Z\text{-}R)\cap(R\text{-}C)=\emptyset \\ F'(\aleph)\cup(G'(\aleph)\cup H'(\aleph)), & \aleph\in(Z\text{-}R)\cap(C\cap R)=\emptyset \\ H'(\aleph)\cup G'(\aleph), & \aleph\in(R\text{-}Z)\cap(C\text{-}R)=\emptyset \\ H'(\aleph)\cup H'(\aleph), & \aleph\in(R\text{-}Z)\cap(R\text{-}C)=Z'\cap C'\cap R \\ H'(\aleph)\cup\big(G'(\aleph)\cup H'(\aleph)\big) & \aleph\in(R\text{-}Z)\cap(C\cap R)=Z'\cap C\cap R \\ (F'(\aleph)\cup H'(\aleph))\cup G'(\aleph), & \aleph\in(Z\cap R)\cap(C\text{-}R)=\emptyset \\ (F'(\aleph)\cup H'(\aleph))\cup H'(\aleph) & \aleph\in(Z\cap R)\cap(R\text{-}C)=Z\cap C'\cap R \\ (F'(\aleph)\cup H'(\aleph))\cup(G'(\aleph)\cup H'(\aleph)) & \aleph\in(Z\cap R)\cap(C\cap R)=Z\cap C\cap R \end{cases}$$

Thus,

$$T(\aleph)=\begin{cases} F'(\aleph), & \aleph\in(Z\text{-}R)-(C\cup R)=Z\cap C'\cap R' \\ G'(\aleph), & \aleph\in(C\text{-}R)-(Z\cup R)=Z'\cap C\cap R' \\ F'(\aleph)\cup G'(\aleph), & \aleph\in(Z\text{-}R)\cap(C\text{-}R)=Z\cap C\cap R' \\ H'(\aleph), & \aleph\in(R\text{-}Z)\cap(R\text{-}C)=Z'\cap C'\cap R \\ G'(\aleph)\cup H'(\aleph) & \aleph\in(R\text{-}Z)\cap(C\cap R)=Z'\cap C\cap R \\ F'(\aleph)\cup H'(\aleph) & \aleph\in(Z\cap R)\cap(R\text{-}C)=Z\cap C'\cap R \\ (F'(\aleph)\cup H'(\aleph))\cup(G'(\aleph)\cup H'(\aleph)) & \aleph\in(Z\cap R)\cap(C\cap R)=Z\cap C\cap R \end{cases}$$

Hence, under the condition $Z'\cap C\cap R=Z\cap C'\cap R=\emptyset$, $N=T$

2) $[(F,Z)\cap_\varepsilon(G,C)]\overset{*}{}_{*_\varepsilon}(H,R)=[(F,Z)\overset{*}{}_{*_\varepsilon}(H,R)]\cap_\varepsilon[(G,C)\overset{*}{}_{*_\varepsilon}(H,R)]$.

3) If $(Z\Delta C)\cap R= Z\cap C\cap R'=\emptyset$, then $[(F,Z)\theta_\varepsilon(G,C)]\overset{*}{}_{*_\varepsilon}(H,R)=[(F,Z)\overset{*}{}_{\lambda_\varepsilon}(H,R)]\cup_\varepsilon[(G,C)\overset{*}{}_{\lambda_\varepsilon}(H,R)]$.

4) If $(Z\Delta C)\cap R=Z\cap C\cap R'=\emptyset$, then $[(F,Z)*_\varepsilon(G,C)]\overset{*}{}_{*_\varepsilon}(H,R)=[(F,Z)\overset{*}{}_{\lambda_\varepsilon}(H,R)]\cap_\varepsilon[(G,C)\overset{*}{}_{\lambda_\varepsilon}(H,R)]$.

Theorem 3.4.3. The following distributions of the complementary extended star operation over complementary extended operations hold:

i) LHS Distributions of Complementary Extended Star Operations over Complementary Extended Soft Set Operations

1) If $Z\cap(C\Delta R)=\emptyset$, then $(F,Z)\overset{*}{}_{*_\varepsilon}[(G,C)\overset{*}{}_{\cap_\varepsilon}(H,R)]=[(F,Z)\overset{*}{}_{*_\varepsilon}(G,C)]\overset{*}{}_{\cup_\varepsilon}[(F,Z)\overset{*}{}_{*_\varepsilon}(H,R)]$.

Proof: Consider first LHS. Let $(G,C)\overset{*}{}_{\cap_\varepsilon}((H,R)=(M,C\cup R)$, where for all $\aleph\in C\cup R$,

$$M(\aleph)=\begin{cases} G'(\aleph), & \aleph\in C-R \\ H'(\aleph), & \aleph\in R-C \\ G(\aleph)\cap H(\aleph), & \aleph\in C\cap R \end{cases}$$

Let $(F,Z)\overset{*}{}_{*_\varepsilon}(M,C\cup R)=(N,Z\cup(C\cup R))$, where for all $\aleph\in Z\cup C\cup R$,

$$N(\aleph)=\begin{cases} F'(\aleph), & \aleph\in Z-(C\cup R) \\ M'(\aleph), & \aleph\in(C\cup R)-Z \\ F'(\aleph)\cup M'(\aleph), & \aleph\in Z\cap(C\cup R) \end{cases}$$

Thus,

$$N(\aleph)=\begin{cases} F'(\aleph), & \aleph\in Z-(C\cup R)=Z\cap C'\cap R' \\ G(\aleph), & \aleph\in(C-R)-Z=Z'\cap C\cap R' \\ H(\aleph), & \aleph\in(R-C)-Z=Z'\cap C'\cap R \\ G'(\aleph)\cup H'(\aleph), & \aleph\in(C\cap R)-Z=Z'\cap C\cap R \\ F'(\aleph)\cup G(\aleph), & \aleph\in Z\cap(C-R)=Z\cap C\cap R' \\ F'(\aleph)\cup H(\aleph), & \aleph\in Z\cap(R-C)=Z\cap C'\cap R \\ F'(\aleph)\cup(G'(\aleph)\cup H'(\aleph)), & \aleph\in Z\cap(C\cap R)=Z\cap C\cap R \end{cases}$$

Now consider the RHS, i.e. $[(F,Z)\overset{*}{}_{*_\varepsilon}(G,C)]\overset{*}{}_{\cup_\varepsilon}[(F,Z)\overset{*}{}_{*_\varepsilon}(H,R)]$. Let $(F,Z)\overset{*}{}_{*_\varepsilon}(G,C)=(V,Z\cup C)$, where for all $\aleph\in Z\cup C$,

$$V(\aleph)=\begin{cases} F'(\aleph), & \aleph\in Z-C \\ G'(\aleph), & \aleph\in C-Z \\ F'(\aleph)\cup G'(\aleph), & \aleph\in Z\cap C \end{cases}$$

Let $(F,Z)\overset{*}{}_{*_\varepsilon}(H,R)=(W,Z\cup R)$, where for all $\aleph\in Z\cup R$,

$$W(\aleph)=\begin{cases} F'(\aleph), & \aleph\in Z-R \\ H'(\aleph), & \aleph\in R-Z \\ F'(\aleph)\cup H'(\aleph), & \aleph\in Z\cap R \end{cases}$$

Let $(V,Z\cup C)\overset{*}{}_{\cup_\varepsilon}(W,Z\cup R)=(T,(Z\cup C)\cup R)$, where for all $\aleph\in Z\cup C\cup R$,

$$T(\aleph)=\begin{cases} V'(\aleph), & \aleph\in(Z\cup C)-(Z\cup R) \\ W'(\aleph), & \aleph\in(Z\cup R)-(Z\cup C) \\ V(\aleph)\cup W(\aleph), & \aleph\in(Z\cup C)\cap(Z\cup R) \end{cases}$$

Thus,

$$T(\aleph)=\begin{cases} F(\aleph), & \aleph\in(Z-C)-(Z\cup R)=\emptyset \\ G(\aleph), & \aleph\in(C-Z)-(Z\cup R)=Z'\cap C\cap R' \\ F(\aleph)\cap G(\aleph), & \aleph\in(Z\cap C)-(Z\cup R)=\emptyset \\ F(\aleph), & \aleph\in(Z-R)-(Z\cup C)=\emptyset \\ H(\aleph), & \aleph\in(R-Z)-(Z\cup C)=Z'\cap C'\cap R \\ F(\aleph)\cap H(\aleph), & \aleph\in(Z\cap R)-(Z\cup C)=\emptyset \\ F'(\aleph)\cup F'(\aleph), & \aleph\in(Z-C)\cap(Z-R)=Z\cap C'\cap R' \\ F'(\aleph)\cup H'(\aleph), & \aleph\in(Z-C)\cap(R-Z)=\emptyset \\ F'(\aleph)\cup(F'(\aleph)\cup H'(\aleph)), & \aleph\in(Z-C)\cap(Z\cap R)=Z\cap C'\cap R \\ G'(\aleph)\cup F'(\aleph), & \aleph\in(C-Z)\cap(Z-R)=\emptyset \\ G'(\aleph)\cup H'(\aleph), & \aleph\in(C-Z)\cap(R-Z)=Z'\cap C\cap R \\ G'(\aleph)\cup(F'(\aleph)\cup H'(\aleph)), & \aleph\in(C-Z)\cap(Z\cap R)=\emptyset \\ (F'(\aleph)\cup G'(\aleph))\cup F'(\aleph), & \aleph\in(Z\cap C)\cap(Z-R)=Z\cap C\cap R' \\ (F'(\aleph)\cup G'(\aleph))\cup H'(\aleph), & \aleph\in(Z\cap C)\cap(R-Z)=\emptyset \\ (F'(\aleph)\cup G'(\aleph))\cup(F'(\aleph)\cup H'(\aleph)), & \aleph\in(Z\cap C)\cap(Z\cap R)=Z\cap C\cap R \end{cases}$$

Thus,

$$T(\aleph)=\begin{cases} G(\aleph), & \aleph\in(C-Z)-(Z\cup R)=Z'\cap C\cap R' \\ H(\aleph), & \aleph\in(R-Z)-(Z\cup C)=Z'\cap C'\cap R \\ F'(\aleph) & \aleph\in(Z-C)\cap(Z-R)=Z\cap C'\cap R' \\ F'(\aleph)\cup H'(\aleph) & \aleph\in(Z-C)\cap(Z\cap R)=Z\cap C\cap R \\ G'(\aleph)\cup H'(\aleph), & \aleph\in(C-Z)\cap(R-Z)=Z'\cap C\cap R \\ F'(\aleph)\cup G'(\aleph) & \aleph\in(Z\cap C)\cap(Z-R)=Z\cap C\cap R' \\ (F'(\aleph)\cup G'(\aleph))\cap(F'(\aleph)\cup H'(\aleph)), & \aleph\in(Z\cap C)\cap(Z\cap R)=Z\cap C\cap R \end{cases}$$

N=T is satisfied under the condition Z∩C'∩R=Z∩C∩R'=∅. It is obvious that the condition Z∩C∩R'=Z∩C'∩R=∅ is equivalent to (Z∩ C) ΔR=∅.

2) If Z'∩C∩R= Z∩C∩R=∅, then $(F,Z)\overset{*}{}_{*_\varepsilon}[(G,C)\overset{*}{}_{\cup_\varepsilon}(H,R)]=[(F,Z)\overset{*}{}_{*_\varepsilon}(G,C)]\overset{*}{}_{\cup_\varepsilon}[(F,Z)\overset{*}{}_{*_\varepsilon}(H,R)]$.

3) If Z'∩C∩R=∅, then $(F,Z)\overset{*}{}_{*_\varepsilon}[(G,C)\overset{*}{}_{*_\varepsilon}(H,R)]=[(F,Z)\overset{*}{}_{+_\varepsilon}(G,C)]\overset{*}{}_{\cap_\varepsilon}[(F,Z)\overset{*}{}_{+_\varepsilon}(H,R)]$.

4) If Z'∩C∩R=∅, then $(F,Z)\overset{*}{}_{*_\varepsilon}[(G,C)\overset{*}{}_{\theta_\varepsilon}(H,R)]=[(F,Z)\overset{*}{}_{+_\varepsilon}(G,C)]\overset{*}{}_{\cup_\varepsilon}[(F,Z)\overset{*}{}_{+_\varepsilon}(H,R)]$.

ii) RHS Distributions of Complementary Extended Star Operation over Complementary Extended Operations

1) If Z∩C∩R'=∅, then $[(F,Z)\overset{*}{}_{\theta_\varepsilon}(G,C)]\overset{*}{}_{*_\varepsilon}(H,R)=[(F,Z)\overset{*}{}_{\lambda_\varepsilon}(H,R)]\overset{*}{}_{\cup_\varepsilon}[(G,C)\overset{*}{}_{\lambda_\varepsilon}(H,R)]$.

Proof: Consider first LHS. Let $(F,Z)\overset{*}{}_{\theta_\varepsilon}(G,C)=(M,Z\cup C)$, where for all ℵ∈Z∪C,

$$M(\aleph)=\begin{cases} F'(\aleph), & \aleph\in Z-C \\ G'(\aleph), & \aleph\in C-Z \\ F'(\aleph)\cap G'(\aleph), & \aleph\in Z\cap C \end{cases}$$

Let $(M,Z\cup C)\overset{*}{}_{*_\varepsilon}(H,R)=(N,(Z\cup C)\cup R)$, where for all ℵ∈Z∪C∪R,

$$N(\aleph)=\begin{cases} M'(\aleph), & \aleph\in(Z\cup C)-R \\ H'(\aleph), & \aleph\in R-(Z\cup C) \\ M'(\aleph)\cup H'(\aleph), & \aleph\in(Z\cup C)\cap R \end{cases}$$

Hence,

$$N(\aleph)=\begin{cases} F(\aleph), & \aleph\in(Z-C)-R=Z\cap C'\cap R' \\ G(\aleph), & \aleph\in(C-Z)-R=Z'\cap C\cap R' \\ F(\aleph)\cup G(\aleph), & \aleph\in(Z\cap C)-R=Z\cap C\cap R' \\ H'(\aleph), & \aleph\in R-(Z\cup C)=Z'\cap C'\cap R \\ F(\aleph)\cup H'(\aleph), & \aleph\in(Z-C)\cap R=Z\cap C'\cap R \\ G(\aleph)\cup H'(\aleph), & \aleph\in(C-Z)\cap R=Z'\cap C\cap R \\ (F(\aleph)\cup G(\aleph))\cup H'(\aleph), & \aleph\in(Z\cap C)\cap R=Z\cap C\cap R \end{cases}$$

Now consider the RHS, i.e. $[(F,Z)\overset{*}{}_{\lambda_\varepsilon}(H,R)]\overset{*}{}_{\cup_\varepsilon}[(G,C)\overset{*}{}_{\lambda_\varepsilon}(H,R)]$. Let $(F,Z)\overset{*}{}_{\lambda_\varepsilon}(H,R)=(V,Z\cup R)$, where for all ℵ∈Z∪R ,

$$V(\aleph)=\begin{cases} F'(\aleph), & \aleph\in Z-R \\ H'(\aleph), & \aleph\in R-Z \\ F(\aleph)\cup H'(\aleph), & \aleph\in Z\cap R \end{cases}$$

Let $(G,C)\overset{*}{}_{\lambda_\varepsilon}(H,R)=(W,C\cup R)$, where for all ℵ∈C∪R,

$$W(\aleph)=\begin{cases} G'(\aleph), & \aleph\in C-R \\ H'(\aleph), & \aleph\in R-C \\ G(\aleph)\cup H'(\aleph), & \aleph\in C\cap R \end{cases}$$

Let $(V,Z\cup R)\ \overset{*}{\underset{\varepsilon}{\cup}}(W,C\cup R)=(T,Z\cup C\cup R)$, where for all $\aleph\in Z\cup C\cup R$,

$$T(\aleph)=\begin{cases} V'(\aleph), & \aleph\in(Z\cup R)-(C\cup R) \\ W'(\aleph), & \aleph\in(C\cup R)-(Z\cup R) \\ V(\aleph)\cup W(\aleph), & \aleph\in(Z\cup R)\cap(C\cup R) \end{cases}$$

Thus,

$$T(\aleph)=\begin{cases} F(\aleph), & \aleph\in(Z-R)-(C\cup R)=Z\cap C\cap R' \\ H(\aleph), & \aleph\in(R-Z)-(C\cup R)=\emptyset \\ F'(\aleph)\cap H(\aleph), & \aleph\in(Z\cap R)-(C\cup R)=\emptyset \\ G(\aleph), & \aleph\in(C-R)-(Z\cup R)=Z'\cap C\cap R' \\ H(\aleph), & \aleph\in(R-C)-(Z\cup R)=\emptyset \\ G'(\aleph)\cap H(\aleph), & \aleph\in(C\cap R)-(Z\cup R)=\emptyset \\ F'(\aleph)\cup G'(\aleph), & \aleph\in(Z-R)\cap(C-R)=Z\cap C\cap R' \\ F'(\aleph)\cup H'(\aleph), & \aleph\in(Z-R)\cap(R-C)=\emptyset \\ F'(\aleph)\cup(G(\aleph)\cup H'(\aleph)), & \aleph\in(Z-R)\cap(C\cap R)=\emptyset \\ H'(\aleph)\cup G'(\aleph), & \aleph\in(R-Z)\cap(C-R)=\emptyset \\ H'(\aleph)\cup H'(\aleph), & \aleph\in(R-Z)\cap(R-C)=Z'\cap C'\cap R \\ H'(\aleph)\cup\big(G(\aleph)\cup H'(\aleph)\big) & \aleph\in(R-Z)\cap(C\cap R)=Z'\cap C\cap R \\ (F(\aleph)\cup H'(\aleph))\cup G'(\aleph), & \aleph\in(Z\cap R)\cap(C-R)=\emptyset \\ \big(F(\aleph)\cup H'(\aleph)\big)\cup H'(\aleph) & \aleph\in(Z\cap R)\cap(R-C)=Z\cap C'\cap R \\ (F(\aleph)\cup H'(\aleph))\cup(G(\aleph)\cup H'(\aleph)) & \aleph\in(Z\cap R)\cap(C\cap R)=Z\cap C\cap R \end{cases}$$

Therefore,

$$T(\aleph)=\begin{cases} F(\aleph), & \aleph\in(Z-R)-(C\cup R)=Z\cap C'\cap R' \\ G(\aleph), & \aleph\in(C-R)-(Z\cup R)=Z'\cap C\cap R' \\ F'(\aleph)\cup G'(\aleph), & \aleph\in(Z-R)\cap(C-R)=Z\cap C\cap R' \\ H'(\aleph), & \aleph\in(R-Z)\cap(R-C)=Z'\cap C'\cap R \\ G(\aleph)\cup H'(\aleph), & \aleph\in(R-Z)\cap(C\cap R)=Z'\cap C\cap R \\ F(\aleph)\cup H'(\aleph), & \aleph\in(Z\cap R)\cap(R-C)=Z\cap C'\cap R \\ (F(\aleph)\cup H'(\aleph))\cup(G(\aleph)\cup H'(\aleph)) & \aleph\in(Z\cap R)\cap(C\cap R)=Z\cap C\cap R \end{cases}$$

It is seen that N=T under the condition $Z\cap C\cap R'=\emptyset$.

2) If $Z\cap(C\,\Delta R)=\emptyset$, then $[(F,Z)\ \overset{*}{\underset{\varepsilon}{\cup}}(G,C)]\ \overset{*}{\underset{\varepsilon}{*}}(H,R)=[(F,Z)\ \overset{*}{\underset{\varepsilon}{*}}(H,R)]\ \overset{*}{\underset{\varepsilon}{\cap}}[(G,C)\ \overset{*}{\underset{\varepsilon}{*}}(H,R)]$.

3) If $(Z\Delta C)\cap R=\emptyset$, then $[(F,Z)\ \overset{*}{\underset{\varepsilon}{\cap}}(G,C)]\ \overset{*}{\underset{\varepsilon}{*}}(H,R)=[(F,Z)\ \overset{*}{\underset{\varepsilon}{*}}(H,R)]\ \overset{*}{\underset{\varepsilon}{\cup}}[(G,C)\ \overset{*}{\underset{\varepsilon}{*}}(H,R)]$.

4) If $Z\cap C\cap R=Z\cap C\cap R'=\emptyset$, then $[(F,Z)\ \overset{*}{\underset{\varepsilon}{*}}(G,C)]\ \overset{*}{\underset{\varepsilon}{*}}(H,R)=[(F,Z)\ \overset{*}{\underset{\varepsilon}{\lambda}}(H,R)]\ \overset{*}{\underset{\varepsilon}{\cup}}[(G,C)\ \overset{*}{\underset{\varepsilon}{\lambda}}(H,R)]$.

Theorem 3.4.4. The following distributions of the complementary extended star operation over soft binary piecewise operations hold:

i) LHS Distributions of the Complementary Extended Star Operation on Soft Binary Pievewise Operations

1) If $Z\cap C'\cap R=\emptyset$, then $(F,Z)\ \overset{*}{\underset{\varepsilon}{*}}[(G,C)\ \overset{\sim}{\cap}(H,R)]=[(F,Z)\ \overset{*}{\underset{\varepsilon}{*}}(G,C)]\ \overset{\sim}{\cup}[(F,Z)\ \overset{*}{*}(H,R)]$.

Proof : Consider first the LHS. Let $(G,C)\overset{\sim}{\cap}(H,R)=(M,C)$. Hence for all $\aleph\in C$,

$$M(\aleph)=\begin{cases} G(\aleph), & \aleph\in C\text{-}R \\ G(\aleph)\cap H(\aleph), & \aleph\in C\cap R \end{cases}$$

Let $(F,Z)\overset{*}{}_{*_\varepsilon}(M,C)=(N,Z\cup C)$, where for all $\aleph\in Z\cup C$,

$$N(\aleph)=\begin{cases} F'(\aleph), & \aleph\in Z\text{-}C \\ M'(\aleph), & \aleph\in C\text{-}Z \\ F'(\aleph)\cup M'(\aleph), & \aleph\in Z\cap C \end{cases}$$

Thus,

$$N(\aleph)=\begin{cases} F'(\aleph), & \aleph\in Z\text{-}C \\ G'(\aleph), & \aleph\in (C\text{-}R)\text{-}Z=Z'\cap C\cap R' \\ G'(\aleph)\cup H'(\aleph), & \aleph\in (C\cap R)\text{-}Z=Z'\cap C\cap R \\ F'(\aleph)\cup G'(\aleph), & \aleph\in Z\cap (C\text{-}R)=Z\cap C\cap R' \\ F'(\aleph)\cup (G'(\aleph)\cup H'(\aleph)), & \aleph\in Z\cap (C\cap R)=Z\cap C\cap R \end{cases}$$

Now consider the rhs, i.e. $[(F,Z)\overset{*}{}_{*_\varepsilon}(G,C)]\tilde{\cup}[(F,Z)\overset{*}{}_{*_\varepsilon}(H,R)]$. Let $(F,Z)\overset{*}{}_{*_\varepsilon}(G,C)=(V,Z\cup C)$, where for all $\aleph\in Z\cup C$,

$$V(\aleph)=\begin{cases} F'(\aleph), & \aleph\in Z\text{-}C \\ G'(\aleph), & \aleph\in C\text{-}Z \\ F'(\aleph)\cup G'(\aleph), & \aleph\in Z\cap C \end{cases}$$

Let $(F,Z)\overset{*}{}_{*_\varepsilon}(H,R)=(W,Z\cup R)$, where for all $\aleph\in Z\cup R$,

$$W(\aleph)=\begin{cases} F'(\aleph), & \aleph\in Z\text{-}R \\ H'(\aleph), & \aleph\in R\text{-}Z \\ F'(\aleph)\cup H'(\aleph), & \aleph\in Z\cap R \end{cases}$$

Let $(V,Z\cup C)\tilde{\cup}(W,Z\cup R)=(T,(Z\cup C))$, where for all $\aleph\in Z\cup C$,

$$T(\aleph)=\begin{cases} V(\aleph), & \aleph\in (Z\cup C)\text{-}(Z\cup R) \\ V(\aleph)\cup W(\aleph), & \aleph\in (Z\cup C)\cap (Z\cup R) \end{cases}$$

Thus,

$$T(\aleph)=\begin{cases} F'(\aleph), & \aleph\in (Z\text{-}C)\text{-}(Z\cup R)=\emptyset \\ G'(\aleph), & \aleph\in (C\text{-}Z)\text{-}(Z\cup R)=Z'\cap C\cap R' \\ F(\aleph)\cap G(\aleph), & \aleph\in (Z\cap C)\text{-}(Z\cup R)=\emptyset \\ F'(\aleph)\cup F'(\aleph), & \aleph\in (Z\text{-}C)\cap (Z\text{-}R)=Z\cap C'\cap R' \\ F'(\aleph)\cup H'(\aleph), & \aleph\in (Z\text{-}C)\cap (R\text{-}Z)=\emptyset \\ F'(\aleph)\cup (F'(\aleph)\cup H'(\aleph)), & \aleph\in (Z\text{-}C)\cap (Z\cap R)=Z\cap C'\cap R \\ G'(\aleph)\cup F'(\aleph), & \aleph\in (C\text{-}Z)\cap (Z\text{-}R)=\emptyset \\ G'(\aleph)\cup H'(\aleph), & \aleph\in (C\text{-}Z)\cap (R\text{-}Z)=Z'\cap C\cap R \\ G'(\aleph)\cup (F'(\aleph)\cup H'(\aleph)), & \aleph\in (C\text{-}Z)\cap (Z\cap R)=\emptyset \\ (F'(\aleph)\cup G'(\aleph))\cup F'(\aleph), & \aleph\in (Z\cap C)\cap (Z\text{-}R)=Z\cap C\cap R' \\ (F'(\aleph)\cup G'(\aleph))\cup H'(\aleph), & \aleph\in (Z\cap C)\cap (R\text{-}Z)=\emptyset \\ (F'(\aleph)\cup G'(\aleph))\cup (F'(\aleph)\cup H'(\aleph)), & \aleph\in (Z\cap C)\cap (Z\cap R)=Z\cap C\cap R \end{cases}$$

Therefore,

$$T(\aleph)=\begin{cases} G'(\aleph), & \aleph\in(C-Z)-(Z\cup R)=Z'\cap C\cap R' \\ F'(\aleph), & \aleph\in(Z-C)\cap(Z-R)=Z\cap C'\cap R' \\ F'(\aleph)\cup H'(\aleph), & \aleph\in(Z-C)\cap(Z\cap R)=Z\cap C'\cap R \\ G'(\aleph)\cup H'(\aleph), & \aleph\in(C-Z)\cap(R-Z)=Z'\cap C\cap R \\ F'(\aleph)\cup G'(\aleph), & \aleph\in(Z\cap C)\cap(Z-R)=Z\cap C\cap R' \\ (F'(\aleph)\cup G'(\aleph))\cup(F'(\aleph)\cup H'(\aleph)), & \aleph\in(Z\cap C)\cap(Z\cap R)=Z\cap C\cap R \end{cases}$$

Here, if we consider Z-C in the function N, since Z-C=Z∩C', if an element is in the complement of C, it is either in R-C or (C ∪ R)' . Thus, if ℵ ∈ Z- C, ℵ ∈Z∩C'∩R or ℵ ∈Z∩C'∩R'. Thus, it is seen that N=T under the condition Z∩C'∩R=∅.

2) If Z∩C∩R'= ∅ , then $(F,Z)\overset{*}{}_{*_\varepsilon}[(G,C)\overset{\sim}{\cup}(H,R)]=[(F,Z)\overset{*}{}_{*_\varepsilon}(G,C)]\overset{\sim}{\cap}[(F,Z)\overset{*}{}_{*_\varepsilon}(H,R)]$.

3) If (ZΔR)∩C=∅ , then $(F,Z)\overset{*}{}_{*_\varepsilon}[(G,C)\overset{\sim}{*}(H,R)]=[(F,Z)\overset{*}{}_{+_\varepsilon}(G,C)]\overset{\sim}{\cap}[(F,Z)\overset{*}{}_{+_\varepsilon}(H,R)]$.

4) If (ZΔC)∩R=Z∩C'∩R=∅ , then $(F,Z)\overset{*}{}_{*_\varepsilon}[(G,C)\overset{\sim}{\theta}(H,R)]=[(F,Z)\overset{*}{}_{+}(G,C)]\overset{\sim}{\cup}[(F,Z)\overset{*}{}_{+_\varepsilon}(H,R)]$.

ii) RHS Distributions of the Complementary Extended Star Operation over Soft Binary Piecewise Operations

1) If (ZΔC)∩R=Z∩C∩R'=∅ , then $[(F,Z)\overset{\sim}{\theta}(G,C)]\overset{*}{}_{*_\varepsilon}(H,R)=[(F,Z)\overset{*}{}_{\lambda_\varepsilon}(H,R)]\overset{\sim}{\cup}[(G,C)\overset{*}{}_{\lambda_\varepsilon}(H,R)]$.

***Proof**:* Consider first LHS. Let $(F,Z)\overset{\sim}{\theta}(G,C)=(M,Z)$, where for all ℵ∈Z,

$$M(\aleph)=\begin{cases} F(\aleph), & \aleph\in Z-C \\ F'(\aleph)\cap G'(\aleph), & \aleph\in Z\cap C \end{cases}$$

Let $(M,Z)\overset{*}{}_{*_\varepsilon}(\ (H,R)=(N,Z\cup R)$, where for all ℵ∈Z∪R,

$$N(\aleph)=\begin{cases} M'(\aleph), & \aleph\in Z-R \\ H'(\aleph), & \aleph\in R-Z \\ M'(\aleph)\cup H'(\aleph), & \aleph\in Z\cap R \end{cases}$$

Thus,

$$N(\aleph)=\begin{cases} F'(\aleph), & \aleph\in(Z-C)-R=Z\cap C'\cap R' \\ F(\aleph)\cup G(\aleph), & \aleph\in(Z\cap C)-R=Z\cap C\cap R' \\ H'(\aleph), & \aleph\in R-Z \\ F'(\aleph)\cup H'(\aleph), & \aleph\in(Z-C)\cap R=Z\cap C'\cap R \\ (F(\aleph)\cup G(\aleph))\cup H'(\aleph), & \aleph\in(Z\cap C)\cap R=Z\cap C\cap R \end{cases}$$

Now consider the RHS, that is, $[(F,Z)\overset{*}{}_{\lambda_\varepsilon}(H,R)]\overset{\sim}{\cup}[(G,C)\overset{*}{}_{\lambda_\varepsilon}(H,R)]$. Let $(F,Z)\overset{*}{}_{\lambda_\varepsilon}(H,R)=(V,Z\cup R)$, where for all ℵ∈Z∪R,

$$V(\aleph)=\begin{cases} F'(\aleph), & \aleph\in Z-R \\ H'(\aleph), & \aleph\in R-Z \\ F(\aleph)\cup H'(\aleph), & \aleph\in Z\cap R \end{cases}$$

Now let $(G,C)\overset{*}{}_{\lambda_\varepsilon}(H,R)=(W,C\cup R)$, where for all ℵ∈CUR,

$$W(\aleph)=\begin{cases} G'(\aleph), & \aleph\in C-R \\ H'(\aleph), & \aleph\in R-C \\ G(\aleph)\cup H'(\aleph), & \aleph\in C\cap R \end{cases}$$

Let $(V,Z\cup R)\overset{\sim}{\cup}(W,C\cup R)=(T,(Z\cup R))$, where for all ℵ∈Z∪R,

$$T(\aleph)=\begin{cases} V(\aleph), & \aleph\in(Z\cup R)-(C\cup R) \\ V(\aleph)\cup W(\aleph), & \aleph\in(Z\cup R)\cap(C\cup R) \end{cases}$$

Thus,,

$$T(\aleph)=\begin{cases} F'(\aleph), & \aleph\in(Z-R)-(C\cup R)=Z\cap C'\cap R' \\ H'(\aleph), & \aleph\in(R-Z)-(C\cup R)=\emptyset \\ F(\aleph)\cup H'(\aleph), & \aleph\in(Z\cap R)-(C\cup R)=\emptyset \\ F'(\aleph)\cup G'(\aleph), & \aleph\in(Z-R)\cap(C-R)=Z\cap C\cap R' \\ F'(\aleph)\cup H'(\aleph), & \aleph\in(Z-R)\cap(R-C)=\emptyset \\ F'(\aleph)\cup\big(G(\aleph)\cup H'(\aleph)\big), & \aleph\in(Z-R)\cap(C\cap R)=\emptyset \\ H'(\aleph)\cup G'(\aleph), & \aleph\in(R-Z)\cap(C-R)=\emptyset \\ H'(\aleph)\cup H'(\aleph), & \aleph\in(R-Z)\cap(R-C)=Z'\cap C'\cap R \\ H'(\aleph)\cup\big(G(\aleph)\cup H'(\aleph)\big) & \aleph\in(R-Z)\cap(C\cap R)=Z'\cap C\cap R \\ \big(F(\aleph)\cup H'(\aleph)\big)\cup G'(\aleph), & \aleph\in(Z\cap R)\cap(C-R)=\emptyset \\ \big(F(\aleph)\cup H'(\aleph)\big)\cup H'(\aleph) & \aleph\in(Z\cap R)\cap(R-C)=Z\cap C'\cap R \\ \big(F'(\aleph)\cup H'(\aleph)\big)\cup\big(G(\aleph)\cup H'(\aleph)\big), & \aleph\in(Z\cap R)\cap(C\cap R)=Z\cap C\cap R \end{cases}$$

Hence

$$T(\aleph)=\begin{cases} F'(\aleph), & \aleph\in(Z-R)-(C\cup R)=Z\cap C'\cap R' \\ F'(\aleph)\cup G'(\aleph), & \aleph\in(Z-R)\cap(C-R)=Z\cap C\cap R' \\ H'(\aleph), & \aleph\in(R-Z)\cap(R-C)=Z'\cap C'\cap R \\ G(\aleph)\cup H'(\aleph), & \aleph\in(R-Z)\cap(C\cap R)=Z'\cap C\cap R \\ F(\aleph)\cup H'(\aleph), & \aleph\in(Z\cap R)\cap(R-C)=Z\cap C'\cap R \\ \big(F(\aleph)\cup H'(\aleph)\big)\cup\big(G(\aleph)\cup H'(\aleph)\big), & \aleph\in(Z\cap R)\cap(C\cap R)=Z\cap C\cap R \end{cases}$$

Under the condition $Z'\cap C\cap R=Z\cap C'\cap R=Z\cap C\cap R'=\emptyset$, it can be seen that N=T. It is obvious that the condition $Z'\cap C\cap R=Z\cap C'\cap R=\emptyset$ is equivalent to the condition $(Z\Delta C)\cap R=\emptyset$.

2) If $Z\cap C'\cap R=\emptyset$, then $[(F,Z)\underset{\cup}{\sim}(G,C)]\overset{*}{}_{*_\varepsilon}(H,R)=[(F,Z)\overset{*}{}_{*_\varepsilon}(H,R)]\underset{\cap}{\sim}[(G,C)\overset{*}{}_{*_\varepsilon}(H,R)]$.

3)If $Z'\cap C\cap R=\emptyset$, then $[(F,Z)\underset{\cap}{\sim}(G,C)]\overset{*}{}_{*_\varepsilon}(H,R)=[(F,Z)\overset{*}{}_{*_\varepsilon}(H,R)]\underset{\cup}{\sim}[(G,C)\overset{*}{}_{*_\varepsilon}(H,R)]$.

4) If $Z\cap(C\Delta R)=\emptyset$, then $[(F,Z)\underset{*}{\sim}(G,C)]\overset{*}{}_{*}(H,R)=[(F,Z)\overset{*}{}_{\lambda_\varepsilon}(H,R)]\underset{\cap}{\sim}[(G,C)\overset{*}{}_{\lambda_\varepsilon}(H,R)]$.

Theorem 3.4.5. The following distributions of the complementary extended star operation over the complementary soft binary piecewise operations exist:

i) LHS Distribution of the Complementary Extended Star Operation on Complementary Soft Binary Piecewise Operations

1)If $Z\cap(C\Delta R)=\emptyset$, then $(F,Z)\overset{*}{}_{*_\varepsilon}[(G,C)\overset{*}{\underset{*}{\sim}}(H,R)]=[(F,Z)\overset{*}{}_{*_\varepsilon}(G,C)]\overset{*}{\underset{\cup}{\sim}}[(F,Z)\overset{*}{}_{*_\varepsilon}(H,R)]$.

Proof: Consider first LHS. Let $(G,C)\underset{\cap}{\sim}(H,R)=(M,C)$, where for all $\aleph\in C$,

$$M(\aleph)=\begin{cases} G'(\aleph), & \aleph\in C-R \\ G(\aleph)\cap H(\aleph), & \aleph\in C\cap R \end{cases}$$

Let $(F,Z)\overset{*}{}_{*_\varepsilon}(M,C)=(N,Z\cup C)$, where for all $\aleph\in Z\cup C$,

$$N(\aleph)=\begin{cases} F'(\aleph), & \aleph\in Z-C \\ M'(\aleph), & \aleph\in C-Z \\ F'(\aleph)\cup M'(\aleph), & \aleph\in Z\cap C \end{cases}$$

Thus,

$$N(\aleph)=\begin{cases} F'(\aleph), & \aleph\in Z-C \\ G(\aleph), & \aleph\in(C-R)-Z=Z'\cap C\cap R' \\ G^{'}(\aleph)\cup H^{'}(\aleph), & \aleph\in(C\cap R)-Z=Z'\cap C\cap R \\ F^{'}(\aleph)\cup G(\aleph), & \aleph\in Z\cap(C-R)=Z\cap C\cap R' \\ F^{'}(\aleph)\cup(G'(\aleph)\cup H'(\aleph)), & \aleph\in Z\cap(C\cap R)=Z\cap C\cap R \end{cases}$$

Now consider RHS, i.e. $[(F,Z)\overset{*}{}_{*_\varepsilon}(G,C)]\overset{*}{\underset{\cup}{\sim}}[(F,Z)\overset{*}{}_{*_\varepsilon}(H,R)]$. Let $(F,Z)\overset{*}{}_{*_\varepsilon}(G,C)=(V,Z\cup C)$, where for all $\aleph\in Z\cup C$,

$$V(\aleph)=\begin{cases} F'(\aleph), & \aleph\in Z-C \\ G'(\aleph), & \aleph\in C-Z \\ F'(\aleph)\cup G'(\aleph), & \aleph\in Z\cap C \end{cases}$$

Let $(F,Z)\overset{*}{}_{*_\varepsilon}(H,R)=(W,Z\cup R)$, where for all $\aleph\in Z\cup R$,

$$W(\aleph)=\begin{cases} F'(\aleph), & \aleph\in Z-R \\ H'(\aleph), & \aleph\in R-Z \\ F'(\aleph)\cup H'(\aleph), & \aleph\in Z\cap R \end{cases}$$

Let $(V,Z\cup C)\overset{*}{\underset{\cup}{\sim}}(W,Z\cup R)=(T,(Z\cup C))$, where for all $\aleph\in Z\cup C$,

$$T(\aleph)=\begin{cases} V'(\aleph), & \aleph\in(Z\cup C)-(Z\cup R) \\ V(\aleph)\cap W(\aleph), & \aleph\in(Z\cup C)\cap(Z\cup R) \end{cases}$$

Thus,

$$T(\aleph)=\begin{cases} F(\aleph), & \aleph\in(Z-C)-(Z\cup R)=\emptyset \\ G(\aleph), & \aleph\in(C-Z)-(Z\cup R)=Z'\cap C\cap R' \\ F(\aleph)\cap G(\aleph), & \aleph\in(Z\cap C)-(Z\cup R)=\emptyset \\ F^{'}(\aleph)\cup F^{'}(\aleph), & \aleph\in(Z-C)\cap(Z-R)=Z\cap C'\cap R' \\ F^{'}(\aleph)\cup H^{'}(\aleph), & \aleph\in(Z-C)\cap(R-Z)=\emptyset \\ F^{'}(\aleph)\cup(F^{'}(\aleph)\cup H'(\aleph)), & \aleph\in(Z-C)\cap(Z\cap R)=Z\cap C'\cap R \\ G^{'}(\aleph)\cup F^{'}(\aleph), & \aleph\in(C-Z)\cap(Z-R)=\emptyset \\ G^{'}(\aleph)\cup H^{'}(\aleph), & \aleph\in(C-Z)\cap(R-Z)=Z'\cap C\cap R \\ G^{'}(\aleph)\cup(F^{'}(\aleph)\cup H'(\aleph)), & \aleph\in(C-Z)\cap(Z\cap R)=\emptyset \\ (F^{'}(\aleph)\cup G'(\aleph))\cup F^{'}(\aleph), & \aleph\in(Z\cap C)\cap(Z-R)=Z\cap C\cap R' \\ (F^{'}(\aleph)\cup G'(\aleph))\cup H^{'}(\aleph), & \aleph\in(Z\cap C)\cap(R-Z)=\emptyset \\ (F^{'}(\aleph)\cup G'(\aleph))\cup(F^{'}(\aleph)\cup H'(\aleph)), & \aleph\in(Z\cap C)\cap(Z\cap R)=Z\cap C\cap R \end{cases}$$

Hence,

$$T(\aleph)=\begin{cases} G(\aleph), & \aleph\in(C-Z)-(Z\cup R)=Z'\cap C\cap R' \\ F^{'}(\aleph), & \aleph\in(Z-C)\cap(Z-R)=Z\cap C'\cap R' \\ F^{'}(\aleph)\cup H'(\aleph) & \aleph\in(Z-C)\cap(Z\cap R)=Z\cap C'\cap R \\ G^{'}(\aleph)\cup H^{'}(\aleph), & \aleph\in(C-Z)\cap(R-Z)=Z'\cap C\cap R \\ F^{'}(\aleph)\cup G'(\aleph) & \aleph\in(Z\cap C)\cap(Z-R)=Z\cap C\cap R' \\ (F^{'}(\aleph)\cup G'(\aleph))\cup(F^{'}(\aleph)\cup H'(\aleph)), & \aleph\in(Z\cap C)\cap(Z\cap R)=Z\cap C\cap R \end{cases}$$

Here, if we consider Z-C in the function N, since Z-C=Z∩C', if an element is in the complement of C, it is either in R-C or $(C\cup R)'$. Thus, if $\aleph\in Z-C$, $\aleph\in Z\cap C'\cap R$ or $\aleph\in Z\cap C'\cap R'$. Hence, it is seen that N=T under the condition $Z\cap C'\cap R=Z\cap C\cap R'=\emptyset$. It is obvious that the condition $Z\cap C'\cap R=Z\cap C\cap R'=\emptyset$ is equivalent to the condition $Z\cap(C\Delta R)=\emptyset$.

2) If $Z\cap C\cap R'=\emptyset$, then $(F,Z)\overset{*}{}_{*_\varepsilon}[(G,C)\overset{*}{\underset{\cup}{\sim}}(H,R)]=[(F,Z)\overset{*}{}_{*_\varepsilon}(G,C)]\overset{*}{\underset{\cap}{\sim}}[(F,Z)\overset{*}{}_{*_\varepsilon}(H,R)]$.

3)If $(Z\Delta R)\cap C=\emptyset$, then $(F,Z)\overset{*}{*_\varepsilon}[(G,C)\overset{*}{\sim}(H,R)]=[(F,Z)\overset{*}{+_\varepsilon}(G,C)]\overset{*}{\underset{\cap}{\sim}}[(F,Z)\overset{*}{+_\varepsilon}(H,R)]$.

4)If $(Z\Delta C)\cap R=\emptyset$, then $(F,Z)\overset{*}{*_\varepsilon}[(G,C)\overset{*}{\underset{\theta}{\sim}}(H,C)]=[(F,Z)\overset{*}{+_\varepsilon}(G,C)]\overset{*}{\underset{\cup}{\sim}}[(F,Z)\overset{*}{+_\varepsilon}(H,R)]$.

ii) RHS Distributions of Complementary Extended Star Operation over Complementary Soft Binary Piecewise Operations

1) If $(Z\Delta R)\cap C=\emptyset$ then $[(F,Z)\overset{*}{\underset{\theta}{\sim}}(G,C)]\overset{*}{*_\varepsilon}(H,R)=[(F,Z)\overset{*}{\lambda_\varepsilon}(H,R)]\overset{*}{\underset{\cup}{\sim}}[(G,C)\overset{*}{\lambda_\varepsilon}(H,R)]$.

Proof: Consider first LHS. Let $(F,Z)\overset{*}{\underset{\theta}{\sim}}(G,C)=(M,Z)$, where for all $\aleph\in Z$,

$$M(\aleph)=\begin{cases}F'(\aleph), & \aleph\in Z-C\\ F'(\aleph)\cap G'(\aleph), & \aleph\in Z\cap C\end{cases}$$

Let $(M,Z)\overset{*}{*_\varepsilon}(H,R)=(N,Z\cup R)$, where for all $\aleph\in Z\cup R$,

$$N(\aleph)=\begin{cases}M'(\aleph), & \aleph\in Z-R\\ H'(\aleph), & \aleph\in R-Z\\ M'(\aleph)\cup H'(\aleph), & \aleph\in Z\cap R\end{cases}$$

Thus,

$$N(\aleph)=\begin{cases}F(\aleph), & \aleph\in(Z-C)-R=Z\cap C'\cap R'\\ F(\aleph)\cup G(\aleph), & \aleph\in(Z\cap C)-R=Z\cap C\cap R'\\ H'(\aleph), & \aleph\in R-Z\\ F(\aleph)\cup H'(\aleph), & \aleph\in(Z-C)\cap R=Z\cap C'\cap R\\ (F(\aleph)\cup G(\aleph))\cup H'(\aleph), & \aleph\in(Z\cap C)\cap R=Z\cap C\cap R\end{cases}$$

Now consider the RHS, that is, $[(F,Z)\overset{*}{\lambda_\varepsilon}(H,R)]\overset{*}{\underset{\cup}{\sim}}[(G,C)\overset{*}{\lambda_\varepsilon}(H,R)]$. Let $(F,Z)\overset{*}{\lambda_\varepsilon}(H,R)=(V,Z\cup R)$, where for all $\aleph\in Z\cup R$,

$$V(\aleph)=\begin{cases}F'(\aleph), & \aleph\in Z-R\\ H'(\aleph), & \aleph\in R-Z\\ F(\aleph)\cup H'(\aleph), & \aleph\in Z\cap R\end{cases}$$

Now let $(G,C)\overset{*}{\lambda_\varepsilon}(H,R)=(W,C\cup R)$, where for all $\aleph\in C\cup R$,

$$W(\aleph)=\begin{cases}G'(\aleph), & \aleph\in C-R\\ H'(\aleph), & \aleph\in R-C\\ G(\aleph)\cup H'(\aleph), & \aleph\in C\cap R\end{cases}$$

Let $(V,Z\cup R)\overset{*}{\underset{\cup}{\sim}}(W,C\cup R)=(T,(Z\cup R))$, where for all $\aleph\in Z\cup R$,

$$T(\aleph)=\begin{cases}V'(\aleph), & \aleph\in(Z\cup R)-(C\cup R)\\ V(\aleph)\cup W(\aleph), & \aleph\in(Z\cup R)\cap(C\cup R)\end{cases}$$

Thus,

$$T(\aleph)=\begin{cases} F(\aleph), & \aleph\in(Z-R)-(C\cup R)=Z\cap C'\cap R' \\ H(\aleph), & \aleph\in(R-Z)-(C\cup R)=\emptyset \\ F'(\aleph)\cap H(\aleph), & \aleph\in(Z\cap R)-(C\cup R)=\emptyset \\ F'(\aleph)\cup G'(\aleph), & \aleph\in(Z-R)\cap(C-R)=Z\cap C\cap R' \\ F'(\aleph)\cup H'(\aleph), & \aleph\in(Z-R)\cap(R-C)=\emptyset \\ F'(\aleph)\cup\big(G(\aleph)\cup H'(\aleph)\big), & \aleph\in(Z-R)\cap(C\cap R)=\emptyset \\ H'(\aleph)\cup G'(\aleph), & \aleph\in(R-Z)\cap(C-R)=\emptyset \\ H'(\aleph)\cup H'(\aleph), & \aleph\in(R-Z)\cap(R-C)=Z'\cap C'\cap R \\ H'(\aleph)\cup\big(G(\aleph)\cup H'(\aleph)\big) & \aleph\in(R-Z)\cap(C\cap R)=Z'\cap C\cap R \\ \big(F(\aleph)\cup H'(\aleph)\big)\cup G'(\aleph), & \aleph\in(Z\cap R)\cap(C-R)=\emptyset \\ \big(F(\aleph)\cup H'(\aleph)\big)\cup H'(\aleph) & \aleph\in(Z\cap R)\cap(R-C)=Z\cap C'\cap R \\ \big(F(\aleph)\cup H'(\aleph)\big)\cup\big(G(\aleph)\cup H'(\aleph)\big), & \aleph\in(Z\cap R)\cap(C\cap R)=Z\cap C\cap R \end{cases}$$

Therefore,

$$T(\aleph)=\begin{cases} F(\aleph), & \aleph\in(Z-R)-(C\cup R)=Z\cap C'\cap R' \\ F'(\aleph)\cup G'(\aleph), & \aleph\in(Z-R)\cap(C-R)=Z\cap C\cap R' \\ H'(\aleph), & \aleph\in(R-Z)\cap(R-C)=Z'\cap C'\cap R \\ G(\aleph)\cup H'(\aleph), & \aleph\in(R-Z)\cap(C\cap R)=Z'\cap C\cap R \\ F(\aleph)\cup H'(\aleph), & \aleph\in(Z\cap R)\cap(R-C)=Z\cap C'\cap R \\ \big(F(\aleph)\cup H(\aleph)\big)\cup\big(G(\aleph)\cup H(\aleph)\big), & \aleph\in(Z\cap R)\cap(C\cap R)=Z\cap C\cap R \end{cases}$$

Under the condition $Z'\cap C\cap R=\ Z\cap C\cap R'=\emptyset$, N=T is satisfied. It is obvious that the condition $Z'\cap C\cap R=\ Z\cap C\cap R'=\emptyset$ is equivalent to $(Z\Delta R)\cap C=\emptyset$

2) If $Z\cap C'\cap R=\emptyset$, then $[(F,Z)\underset{\cup}{\overset{*}{\sim}}(G,C)]\overset{*}{}_{*_\varepsilon}(H,R)=[(F,Z)\overset{*}{}_{*_\varepsilon}(H,R)]\underset{\cap}{\overset{*}{\sim}}[(G,C)\overset{*}{}_{*_\varepsilon}(H,R)]$.

3)If $(Z\Delta C)\cap R=\emptyset$, then $[(F,Z)\underset{\cap}{\overset{*}{\sim}}(G,C)]\overset{*}{}_{*_\varepsilon}(H,R)=[(F,Z)\overset{*}{}_{*_\varepsilon}(H,R)]\underset{\cup}{\overset{*}{\sim}}[(G,C)\overset{*}{}_{*_\varepsilon}(H,R)]$.

4) If $Z\cap(C\Delta R)=\emptyset$, then $[(F,Z)\underset{*}{\overset{*}{\sim}}(G,C)]\overset{*}{}_{*_\varepsilon}(H,R)=[(F,Z)\overset{*}{}_{\lambda_\varepsilon}(H,R)]\underset{\cap}{\overset{*}{\sim}}[(G,C)\overset{*}{}_{\lambda_\varepsilon}(H,R)]$.

4. CONCLUSION

Soft set operations are at the heart of soft set theory, providing a foundational structure for managing uncertainty in both data analysis and decision-making processes. This paper introduces a novel soft set operation named complementary extended star operation and explores its algebraic properties. Additionally, we examine how complementary extended star distributes over various other operations on soft sets. It is our aim that this study will serve as a guiding framework for future investigations into soft set operations. Further study may examine various kinds of complementary extended soft set operations and their distributions and characteristics to find out what algebraic structures arise in the collection of soft sets together with complementary extended star operation of soft sets.

SIMILARITY RATE: 19%

AUTHOR CONTRIBUTION

Aslıhan Sezgin: Conceptualization, methodology, data curation, editing, Murat Sarıalioğlu: Conceptualization, writing, editing.

CONFLICT of INTEREST

The authors declared that they have no known conflict of interest.

ACKNOWLEDGEMENT:

This article is a part of the second author's MSc. Disseration at Amasya University, Türkiye.

REFERENCES

[1] D. Molodtsov, "Soft set theory-first results", *Computers and Mathematics with Applications*, 37 (1), pp. 19-31, 1999.
[2] P.K. Maji, R. Bismas, A.R. Roy, "Soft set theory", *Computers and Mathematics with Applications,* 45 (1), pp. 555-562, 2003.
[3] D. Pei and D. Miao, "From Soft Sets to Information Systems", *In: Proceedings of Granular Computing IEEE*, 2, pp. 617-621, 2005.
[4] M. I. Ali, F. Feng, X. Liu, W. K. Min., M. Shabir, "On some new operations in soft set theory", *Computers and Mathematics with Applications*, 57(9), pp. 1547-1553, 2009.
[5] A. Sezgin, A. O. Atagün, "On operations of soft sets", *Computers and Mathematics with Applications*, 61(5), pp. 1457-1467, 2011.
[6] M.I. Ali, M. Shabir, M. Naz, "Algebraic structures of soft sets associated with new operations", *Computers and Mathematics with Applications*, 61, pp. 2647–2654, 2011.
[7] A. Sezgin, A. Shahzad, A. Mehmood, "New operation on soft sets: Extended difference of soft sets", *Journal of New Theory*, (27), pp. 33-42, 2019.
[8] N.S. Stojanovic, "A new operation on soft sets: extended symmetric difference of soft sets", *Military Technical Courier*, 69(4), pp.779-791, 2021.
[9] Ö. F. Eren, H. Çalışıcı, "On some operations of soft sets", *The Fourth International Conference on Computational Mathematics and Engineering Sciences,* Antalya, 2019.
[10] A. Sezgin, H. Çalışıcı, "A comprehensive study on soft binary piecewise difference operation", *Eskişehir Teknik Üniversitesi Bilim ve Teknoloji Dergisi B* -Teorik *Bilimler*, 12 (1), pp. 32-54, 2024.
[11] N. Çağman, "Conditional complements of sets and their application to group theory", *Journal of New Results in Science*, 10(3), pp. 67-74, 2021.
[12] A. Sezgin, N. Çağman, A.O. Atagün, F.N Aybek, "Complemental binary operations of sets and their application to group theory," *Matrix Science Mathematic*, 7(2), pp. 114-121, 2023.
[13] F. N. Aybek, *New restricted and extended soft set operations*, Master of Science Thesis, Amasya University, The Graduate School of Natural and Applied Sciences, Amasya, 214pp, 2024.
[14] A.Sezgin, A., A.O. Atagün, "New soft set operation: Complementary soft binary piecewise plus operation", *Matrix Science Mathematic,* 7 (2), pp. 125-142, 2023.
[15] A. Sezgin, F.N. Aybek, "New soft set operation: Complementary soft binary piecewise gamma operation", *Matrix Science Mathematic,* 7 (1), pp. 27-45, 2023.
[16] A. Sezgin, F.N. Aybek, A.O. Atagün, "New soft set operation: Complementary soft binary piecewise intersection operation", *Black Sea Journal of Engineering and Science*, 6 (4), pp.330-346, 2023.
[17] A. Sezgin, F.N. Aybek, N.B Güngör, "New soft set operation: Complementary soft binary piecewise union operation", *Acta Informatica Malaysia,* 7 (1), pp.38-53, 2023.
[18] A. Sezgin, A.M. Demirci, "New soft set operation: complementary soft binary piecewise star operation", *Ikonion Journal of Mathematics,* 5 (2), pp.24-52, 2023.
[19] A. Sezgin, E. Yavuz, "New soft set operation: Complementary soft binary piecewise lambda operation", *Sinop University Journal of Natural Sciences,* 8 (2), pp. 101-133, 2023.
[20] A. Sezgin, N. Çağman, "New soft set operation: Complementary soft binary piecewise difference operation", *Osmaniye Korkut Ata University Journal of the Institute of Science and Technology,* 7 (1), pp. 58-94, 2024.
[21] A. Sezgin, K. Dagtoros, "Complementary soft binary piecewise symmetric difference operation: A novel soft set operation," *Scientific Journal of Mehmet Akif Ersoy University*, 6 (2), pp. 31–45, 2023.
[22] A. Sezgin, M. Sarıalioğlu, "New soft set operation: Complementary soft binary piecewise theta operation", *Journal of Kadirli Faculty of Applied Sciences*, 4(2), pp. 1-33, 2023.
[23] E. Akbulut, *New type of extended operations of soft sets: Complementary extended difference and lamda operations*, Master of Science Thesis, Amasya University, The Graduate School of Natural and Applied Sciences, Amasya, 89pp, 2024
[24] A.M. Demirci, *New type of extended operations of soft sets: Complementary extended union, plus and theta operations*, Master of Science Thesis, Amasya University, The Graduate School of Natural and Applied Sciences, Amasya, 204pp, 2024.

[25] A. S. Sezer, "Certain Characterizations of LA-semigroups by soft sets", *Journal of Intelligent and Fuzzy Systems, 27* (2), pp. 1035-1046, 2014.
[26] A.S. Sezer, N. Çağman, A.O. Atagün, "Uni-soft substructures of groups", *Annals of Fuzzy Mathematics and Informatics,* 9 (2), pp. 235–246, 2015.
[27] A. Sezgin, "A new view on AG-groupoid theory via soft sets for uncertainty modeling", *Filomat, 32*(8), pp. 2995–3030, 2018.
[28] T. Mahmood, Z.U. Rehman, A. Sezgin, "Lattice ordered soft near rings", *Korean Journal of Mathematics, 26* (3), pp. 503-517, 2018.
[29] E. Muştuoğlu, A. Sezgin, Z.K. Türk, "Some characterizations on soft uni-groups and normal soft uni-groups", *International Journal of Computer Applications, 155* (10), pp. 1-8, 2016.
[30] A. Sezgin, A.O. Atagün, N. Çağman, H. Demir, "On near-rings with soft union ideals and applications", *New Mathematics and Natural Computation,* 18(2), pp. 495-511, 2022.
[31] Ş. Özlü, A. Sezgin, "Soft covered ideals in semigroups", *Acta Universitatis Sapientiae Mathematica,* 12 (2), pp. 317-346,2020.
[32] C.Jana, M. Pal, F. Karaaslan, A. Sezgin, (2019), "(α, β)-soft intersectional rings and ideals with their applications" *New Mathematics and Natural Computation,* 15 (2), pp. 333–350.
[33] A. Sezgin, E. Yavuz, "A new soft set operation: Soft binary piecewise symmetric difference operation", *Necmettin Erbakan University Journal of Science and Engineering,* 5 (2), pp. 189-208, 2023.
[34] E. Yavuz, *Soft binary piecewise operations and their properties*, Master of Science Thesis, Amasya University, The Graduate School of Natural and Applied Sciences, Amasya, 244pp, 2024.
[35] S. Pant, K. Dagtoros, M.I. Kholil, A. Vivas, "Matrices: Peculiar determinant property", *Optimum Science Journal*, 1, pp. 1–7, 2024.

.

Eurasian Journal of Science Engineering and Technology

Technical Brief Article

INTEGRATION OF GRID SCALE BATTERY ENERGY STORAGE SYSTEMS AND APPLICATION SCENARIOS

Obed Nelson ONSOMU[1,*], Alper ÇETİN[2], Erman TERCİYANLI[3], Bülent YEŞİLATA[4]

[2] *Partner EGS, Ankara, Türkiye*
[1,3] *INAVITAS, Ankara, Türkiye*
[1,4] *Ankara Yildirim Beyazıt University, Energy Systems Engineering, Ankara, Türkiye*

ABSTRACT

Integration of renewable energy sources (RESs) into the grid has profoundly gained a lot of attention in the energy domain, coupled with an ever-changing generation profile and dependency on weather conditions, RESs are commonly known to pose security of supply challenges and in case they are not monitored they can cause techno-economic losses and even lead to catastrophic failure of the electrical grids. However, their availability and negligible generation cost make them environmentally friendly when compared to conventional energy sources. For seamless connection of renewables to the grid network, battery energy storage system (BESS) has been suggested in literature, the technology has come to the fore recently, and has found application cases in the utility grid with enhanced functions to participate in both reserve and wholesale electricity markets such as day-ahead and intra-day markets. This technical brief presents various energy storage systems (ESSs) potentially used in large-scale grid networks, which are investigated, and their individual properties are compared, where necessary application areas with examples enabled by constituting material properties are outlined, in the same context their general advantages and disadvantages are given in reference to the specific application cases. In addition, the application of large-scale BESS is explained together with the integration solutions such as use of Virtual Power Plant (VPP) and microgrid.

Keywords: Renewable Energy, Battery Energy Storage Systems, Large-scale Storage, Energy Arbitrage, Virtual Power Plant

1. INTRODUCTION

Advancement in technology and high population increase has significantly facilitated increased electricity demand globally. According to the information from Turkish Electricity Transmission Corporation (TEİAŞ), Turkey's total energy production between 2019 and 2022 increased by approximately 10% which is about 331 TWh [1]. In 2022, approximately 57.5% of electricity generation was gotten from fossil resources (coal and natural gas) as shown in Figure-1 [2]. Normally, greenhouse gas emissions are associated with fossil fuels which have so far led to increase in global temperature, which has led to serious discussions on how the impact of climate change can be mitigated, starting with Paris climate agreement or accord that entered into effect in 2016, the agreement requires participating countries to limit their emissions to generally contribute to the limitation of the global temperature increase [3], so as to achieve the accord's target of having a carbon neutral economy. Similarly, the European Commission aims to generate 45% of electricity from RESs by 2030 [4]. The challenge of having RESs as generation sources, is that their generation profile is dependent on the weather or meteorological conditions, in any case they stand as the most efficient solution that can be used to curb climate change due to their ease of availability and negligible operational costs. Also, it is important to note that RESs are preferred when they operate in off-grid mode, largely due to control technicalities and inaccurate forecasts subject to low fidelity forecasting tools that might not capture the actual generated power, i.e., when the predicted power in relation to the power delivered do not match then operation of the national transmission grid will be jeopardized. The other aspect is provision of grid inertia, whereby renewables fail to provide grid inertia compared to fossil-based sources which are known for their steady supply over a long period. So, to counter voltage and frequency stability problems in the electrical transmission network [5], researchers have proposed ESS to help mitigate some of the shortcomings associated with RESs into the grid network such as stochasticity or intermittency, this phenomenon can potentially damage electronic equipment when huge power imbalances occur.

* Corresponding author, e-mail: obedonsomu@gmail,com (O. N. Onsomu)
Recieved: 25.12.2023 Accepted: 02.04.2024
doi: 10.55696/ejset.1409774

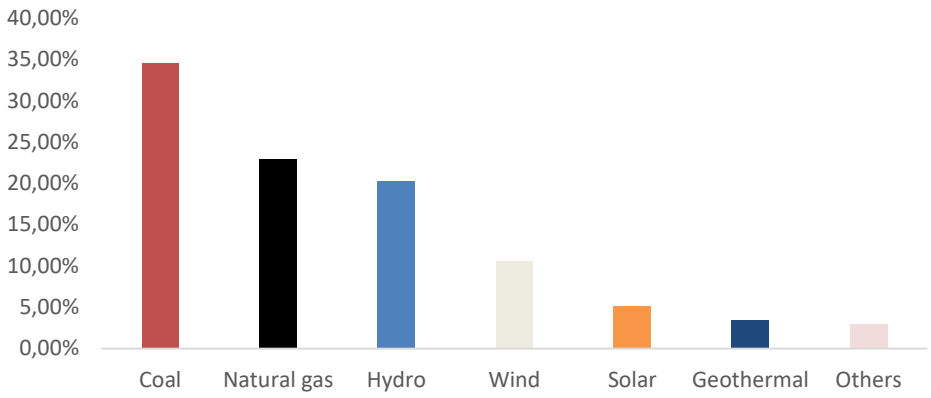

Figure 1. Production of electricity in Turkey by source (2022).

According to the grid transformation agenda, the inclusion of renewables has been a key research area, and in part has necessitated concrete multi-disciplinary approach in terms of renewables management and formulation of effective curtailment plans, also the inclusion of distributed generation (DG) into the grid networks has facilitated the primary purpose of having greener grid networks[6]. Other important aspects include large-scale integration of renewables through precise scaling up of energy generated from renewables, whereby various studies have been carried out, and it has been found that grid-level energy storage can come in handy when excess power is generated from renewables. In [7], ESSs have seen a significant decline as the projected cost is preempted to decline through 2030. Additionally, studies show that cost effective ESSs have gained growth rate of 42% yearly in the period between 2020 and 2030. Also, ESSs have found application use cases in grid networks, due to their rapid spontaneous response, modularization and easy installation process [8]. Authors in [9], discuss efficient ways of using ESSs and their long-term economic viability, a detailed description of diverse technologies with varying features are outlined. Furthermore, a case study of an ESS participating in an energy market is discussed [10], the study provides an assessment on storage with comprehensive electricity market guidelines at the national level. Similarly [11], three main electricity market recommendations are given, they are wholesale, ancillary and capacity markets, subsequently market rules have been clearly outlined with precedence given to the type of generating technology, compensation procedures and demand response programs. While in [12], a grid-scale application with a cost model for production is presented, the model details monopoly power markets whereby ESS offers energy and participates in ancillary market.

In brief, ESSs are divided into 5 main categories which are primarily connected to the nature of the electrolyte and material composition, as shown in Figure-2 [13], their classification influences application cases which depend on the level of technology, recently BESS have been widely used for functions such as frequency and voltage regulation, load balancing, peak demand reduction, power quality improvement and RES integration into the grid [14].

This review paper is structured as follows, classification of ESSs, application of large-scale BESS with the main functions, discussion and finally conclusion.

2. BATTERY ENERGY STORAGE SYSTEMS (BESSs)

A. Lead Acid Battery

Lead-acid battery is one of the oldest rechargeable electrochemical storage technologies and its invention goes back to 1859, the charging and discharge process are a bit slow for lead acid batteries and the technology they use is not as complicated as other storage batteries. The fact that they have low production cost makes them affordable and easily available, even though they are limited by the number of discharge/charge cycles because of having low energy when compared to their weight and volume ratio, respectively [15]. In terms of grid storage applications, they can easily be altered, or their electrochemical composition can be modified to provide grid-scale services. There are also advanced lead-acid batteries, which are obtained through addition of carbon to the electrodes, they are known to have longer life and capacity which makes them more expensive when compared to traditional lead acid batteries [16].

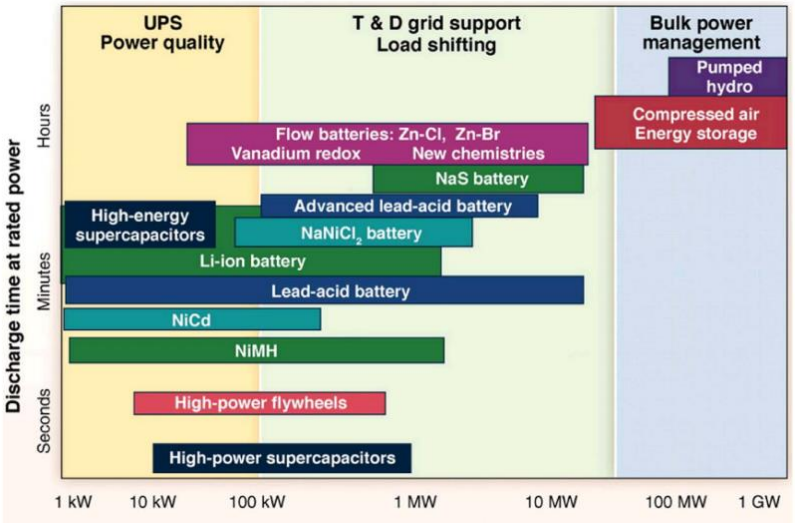

Figure 2. Classification of ESSs based on power output [17]

B. Nickel Cadmium BS

Nickel cadmium (NiCd) batteries are devices with well-developed technology. Their commercial application goes back to 1915, they have low maintenance costs with high energy density and an average lifespan. NiCd batteries can operate well at low temperatures compared to other BESSs even though they have relatively low lifespan [18]. They are also ideal in ensuring voltage stability [19] an essential parameter in power systems. Furthermore, their popularity in solar power plants application is partly due to their ability to withstand high temperatures. NiCd are usually not preferred for peak shaving functions which limits their usage in energy management systems applications [20].

C. Nickel Metal Hydride

Nickel-metal hydride (NiMH) batteries are similar to nickel-cadmium batteries, but NiMH electrodes have a hydrogen-absorbing alloy unlike NiCd which has cadmium material for the electrodes [21]. It commercially appeared for the first time in 1995 and replace nickel cadmium batteries. They have high energy density and low energy efficiency. They are environmentally friendly and compared to NiCd they are not affected by the memory effect and can dissipate high voltage regardless of the nature of charge-discharge circles [22].

D. Sodium Sulfide

Sodium-sulfur batteries are rechargeable high-temperature battery technologies, and they offer attractive solutions for large-scale ESSs. Their applications include load balancing, power quality, and peak shaving, as well as integration and management of renewable energy. These batteries have high energy density, long life span, high charge and discharge efficiency, and are manufactured from readily available materials [23]. They can operate over a wide range of temperatures between 300-350 °C, they are suitable for large-scale grid energy storage [24].

E. Lithium Ion BS

Lithium-ion got commercialized by Sony in 1991. Lithium battery technology is popular mostly in portable electronics, especially laptop and mobile systems [25], [26]. The technology finds application in hybrid electric vehicles and utility-scale storage systems [27]. They have advantages such as high energy density and low energy efficiency, low maintenance cost, and lower self-discharge rate when compared to lead-acid and nickel-cadmium. Additionally, they have quick response to dispatch signal, high power density, and can operate well under high temperatures.

However, their lifespan depends on temperature, another disadvantage is the safety issue caused by metal oxide, which are thermally vulnerable to high temperatures and become more unstable as temperatures significantly increase, this causes them to release oxygen and heat. Therefore, it is always recommended to avoid over-charging and deep discharge to avoid potential fire breakout or even first-degree burns , some of these safety issues have been managed by equipping lithium-ion batteries with a monitoring unit[28].

F. Flow Battery

Flow batteries have been newly introduced into the market and their rate of adoption is impressive , when relatively compared to other BESSs, flow batteries have been found suitable for large-scale grid network application. Their working principle involves converting electrical energy into chemical potential energy, the liquid electrolyte is charged and after enough charge is obtained, stored energy gets released and the process starts all over again. Electrolytes are stored externally in tanks and pumped directly into the electrochemical cell, which converts chemical energy into electricity and vice versa. Capacities can be easily adjusted by changing the number of electrodes [29], [30]. There are various types of flow batteries, for instance, vanadium redox flow batteries (VRB), polysulfide bromide batteries (PSB), and zinc-bromine batteries (ZBR). Table 1 shows some of the important features of BESSs.

Table 1 . Features for different BESSs [13], [31]

Type	Energy Density (Wh/kg)	Life (Cycle)	Cost ($/kWh)	Efficiency (%)	Applications
Lead Acid	25–45	200–1800	150–500	65–80	Peak shaving, Spinning reserve, Regulating frequency
Nickel Cadmium	50–75	2000–2500	800–1500	60-70	Regulating frequency,
Nikel Metal Hidride	170–420 Wh/L	----------	----------	65-70	Peak shaving,
Sodium Sulfide	150–240	2500–4500	300-500	75-90	Peak shaving, RES integration, Power quality,
Lithium Ion	80–200	1000–10,000	600–2500	90-97	Arbitration Peak shaving, Regulating frequency, Power quality,
Vanadium Redox Flow	10–50	12,000–14,000	150-1000	75-85	Peak shaving, Arbitrage, Regulating frequency, Power quality

The advantages of Redox flow technology are, a low rate of self-discharge, no distortion in case of deep discharge, Redox maintenance costs are low. Finally, the storage technology can operate for years before replacement. The shortcomings are, the technology has high costs when it comes to investment, and it is technically challenging to develop and operate. Redox flow battery can be an attractive investment option for ESS owners and as for large-scale ESS applications, however thorough techno-economic aspects have to be evaluated [32], [33].

3 LARGE-SCALE APPLICATION OF BESS

BESS has gained prominence in recent years as a promising technology to eliminate the problems caused by intermittent renewable energy systems in the grid network. The different functions that ESSs can perform can be divided into three categories: transmission, distribution and consumption level according to the general supply points to the grid. At the transmission level, it provides the grid integration and ancillary services functions of renewable energy systems, while at the distribution level, it performs functions such as power quality and deferral of capacity investments in distribution systems [34-36]. In addition, energy storage can be installed at the consumer site to cut-down electricity bills, improve power quality and reliability, similarly ESSs can easily facilitate participation of RESs into the wholesale markets, the size and installation of ESSs depends on the energy needs of the power system to be powered, consumer level usually their power needs are low and unlike large scale ESSs which are designed to have higher storage capacity and specifically meet power demand of the wider grid network [37], [38]. The applications of large-scale BESS are summarized in Figure-3. Some examples of BESSs with real field applications are specified in Table-2.

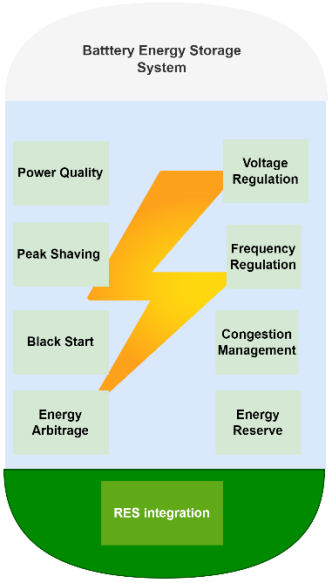

Figure 2. Applications cases of large-scale BESS.

Table 2. BESS Projects [40], [41]

Project Name	Country in operation	Power (MW)	Function & Services	Type of Battery
Dailan VFB	China	200	Arbitrage, Black start, Peak Shaving	Flow
Hornsdale Power Reserve	Australia	150	Arbitrage, Frequency regulation,	Lithium Ion
Notress Battery storage	USA	36	Arbitration, Frequency regulation,	Lithium Ion
Magdeberg-SK Innovation	Germany	30	RES integration	Lithium-ion
Puerto Rico Electric Power Authority Battery System	Puerto Rico	20	Frequency regulation, Revolving reserve	Lead acid
Amplex Group	United Arab Emirates	35	Frequency regulation, Voltage regulation, Power quality, Arbitrage	Sodium sulfide

A. Energy Arbitrage

Energy arbitrage plays a significant role in the economic operation of the power grid network. BESSs can be used to make profit by selling or buying energy at the most suitable time. The main objective is to sell energy at a high price and buy energy when the price is low [29], arbitrage process is susceptible to extreme environmental conditions in that the over-generation by RESs can led to price negativity, in the sense that energy prices become more volatile and unpredictable, negative electricity prices adversely affect energy trading or energy markets dynamics . With proper management of RESs, i.e., using storage for energy arbitrage can act as management platform for demand and supply of energy [39]. Figure 3 shows technical schematic for energy arbitrage and how power conversion system (PCS) is interconnected to the external grid.

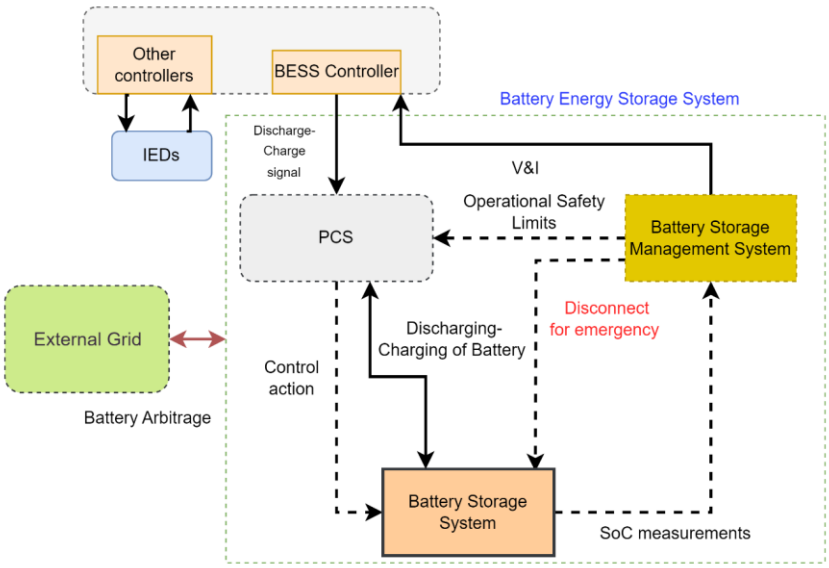

Figure 3. Energy Arbitrage technical schematic.

Furthermore, Figure 3 indicates essential components such as, battery storage management system (BSMS) also known as BMS, which strictly ensures the operational conditions of the BESS in regard to discharge and charging cycles are not violated, while the BESS controller ensures the PCS is input with setpoints that facilitate the arbitrage process. Other componets such as intelligent electronic devices (IEDs) can as well be added.

B. Peak Shaving

High energy demand is directly connected to high population, industry and trade growth, given the demand and supply forces these factors can lead to sharp peaks on consumption profile, for example during peak hours that is early morning and late evening hours energy demand is on the peak. Due to these dynamics, consumption peaks can be absorbed by BESS and deferred for later consumption ,i.e., when there is inadequate energy supply (valleys) this will help stabilize the grid. Therefore, there is growing interest in peak shaving to meet this extra energy demand with the help of BESS. The main difference between peak shaving and energy arbitrage is the economic interest of the latter which focuses on the trading prices, when the prices are low, the BESS buys and when they are high the BESS sells to make profits . During high power demand, the BESS can be committed to supply the grid [42].

C. Reserves

Reserve refers to the backup power generation capacity kept for emergencies or when there is sudden outage. Operators have to ensure the grid is always stable even in the event of a malfunction. However, the use of fast-reacting technologies such as BESS provides an alternative solution. Primary reserve, secondary reserve, and tertiary reserve can be used to maintain grid stability [43], and optimally keep some generators in the grid to operate with a small percentage of reserve capacity, the benefits accrued are reduced extra costs and minimal system inefficiencies.

D. Frequency Regulation

Frequency is an important factor used to maintain the balance between production and load. Network operators have to operate the electricity network at a certain frequency value by balancing production and consumption. BESSs perform frequency control by adjusting the amount of energy they import from the grid, or they export to the grid. This is important in power systems and especially when more renewables need to be integrated. Therefore, BESSs are flexible and crucial energy technological invention targeted to maintain stability of the grid network through up-regulation and down-regulation network resources to ensure balanced supply and demand of energy [38], [44].

E. Voltage Regulation

Also, voltage variation is another sensitive factor affecting general stability of the grid network, it must be kept within specific limits to maintain the stability of the system. Voltage and reactive power are interdependent; therefore, BESSs supports mains voltage by providing reactive power [45].

F. Power Quality

Fluctuations in frequency and voltage occur in networks with high-RES penetration. Modern voltage and frequency control methods are necessary to solve these deviations. BESS can eliminate power quality problems such as voltage sag and swell, voltage harmonics and flickers that RES can cause [38].

G. Black Start

Black start refers to restoration of the grid or re-energizing the grid network without relying on an external source during a complete or partial collapse. This requires repairing of transmission lines and power plants, and a quick response of high-capacity BESS. In this case, BESSs are envisioned to have a discharge time ranging from minutes to an hour while waiting for the network to be restored again. Lithium-ion-based BESSs are widely used technologies for black start [46].

H. RES Integration

Storage systems can act as support systems for grid network system, they can balance power especially when RESs are connected to the grid. It is known that RES poses extreme challenges to system operators, based on their generation profile, which is highly unreliable, RESs can be managed using storage as the best option. Given the unpredictability of wind speed, solar radiation and temperature, the generation profile becomes highly unreliable and can result in both frequency and voltage imbalances which can lead to unprecedented shutdown of the grid network. Through addition of storage, some of these challenges can be mitigated effectively. Studies show application level of BESS with RES in eliminating power imbalances in the production profile [47].

I. Congestion Management in Transmission and Distribution Network Levels

As the integration of RES into the grid increases, so as the risk of congestion. The simplest and most applied solution to eliminate grid congestion is building a new transmission line or upgrading an existing one, building or upgrading transmission infrastructure may not always be the best solution [36], as the process is costly and takes time without forgetting negative environmental effects. That is why BESSs could be the best option in terms having relatively low social and environmental impacts and also significantly saves time on engineering procurement and construction, BESSs can help overcome many setbacks caused by renewables integration to the transmission and distribution systems [48] and can defer upgrades of both transmission and distribution systems [38].

J. Significance of Integrating BESS with Microgrid and VPP

As put forward BESS has found application cases on large-scale grid network, however they can also be applied for microgrid and VPP as well. The two concepts are broadly different, and a lot of studies have used BESS to provide power for microgrid when conventional sources are shutdown or when RES are deployed. It is well known microgrids connect areas that are far away from the main grid, they can either be on-grid or off-grid [33] and largely aim to facilitate self-consumption of power, unlike virtual power plants microgrid generally work under the principle of only import when there is deficit to continuously cut-down operational costs. On the other hand, VPP aims at maximizing social welfare of its participants and links DERs to the wholesale electricity market [49], they are developed with the idea of optimizing network resources and dispatching at the right hour, and as mentioned previously, BESS with arbitrage characteristics can come in handy in terms of associating real-time control of network resources and maximizing revenue for VPP users. Additionally, the benefits of having ESSs in VPP set-up cannot be overlooked, given the comprehensive modules the VPP possess from AI to advanced data and predictive analytics, etc., ESSs can carefully be dispatched, and instances of overcharging or underutilization of the generic network resources can be avoided.

Study such as [50], has covered virtual energy storage systems (VESS), that applies VPP concept to geographically coordinate demand response originating from refrigerators in the city using an incoming regulation signal and the response of flywheel energy storage system (FESS); the authors point out, one of the economic importance of the approach is reduced system costs of FESS, uncertainties management and reduced carbon emissions . The VESS in this specific arrangement can also be used to provide frequency regulation services to the grid network. Figure 4, shows a simple diagram integrating BESS into the VPP, it forms part of the generation profile with other distributed generation systems which are scheduled for dispatch based on the

nature of the electricity market, as per the published bids and offers the network resources can participate in the wholesale market or ancillary service market monitored by the independent system operator (ISO)

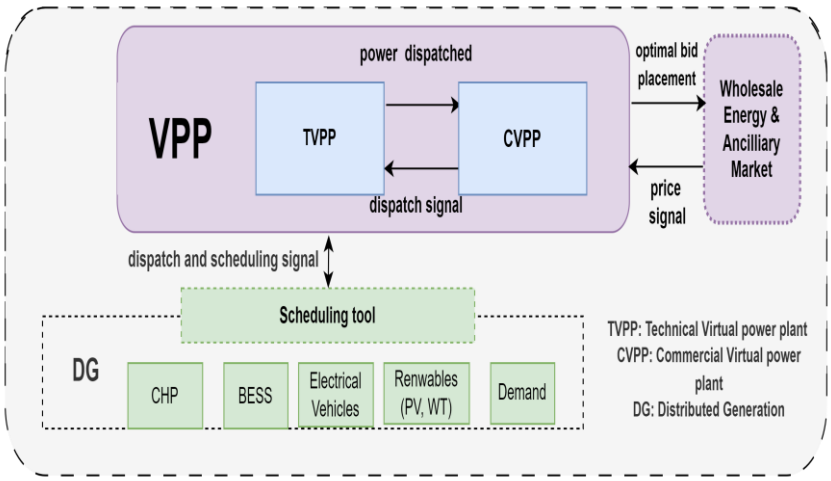

Figure 4. BESS VPP integration diagram

3. CONCLUSION

In this article, an overview of grid integration and applications of large-scale BESSs has been given, the available storage technologies and their scale of application have been clearly outlined. It is imperative to understand the nature of storage technology available and the value to be derived from the technology, various BESSs have material composition that make their performance higher while some of the BESSs operate well under high temperatures. This work has identified, the advantages and disadvantages of different battery types and application cases, through feature comparison study, some of the basic features include power density, the cost associated with the technology, lifespan and the function or services the technology provides. Lithium-ion and flow BESSs are found to have high capacity and long lifespan; but their cost is high. On the other hand, sodium sulfide and lead acid BESSs have low cost, but short lifespan. Their short lifespan limits them from being used for long-term energy arbitrage applications. Also, large-scale BESSs for network applications was examined, and the study shows they can come in handy to improve stability of the grid, they can also facilitate energy arbitrage, network integration of RESs, power quality, black start, peak shaving, spinning reserve, congestion management and can efficiently support voltage and frequency regulation processes. In addition, VPP and microgrid platforms have been identified to support BESS, the capabilities of the two platforms in terms of asset management can facilitate the functions provided by BESS, for instance energy arbitrage applicable for profit-making for investors or energy hub owners, who can use the VPP platform for decision-making regarding optimal discharge or charge of their storage resources.

Finally, BESS for grid-scale integration is a recent development and given the proliferation of RESs into the market, the technology can be put into use to manage RESs and offer ancillary services to the grid network.

SIMILARITY RATE: 15%

AUTHOR CONTRIBUTION

First Author: conceptualization, methodology, writing, and editing. Second Author: conceptualization, methodology, writing, editing. Third Author: editing. Fourth Author, conceptualization, editing and supervision.

CONFLICT of INTEREST

The authors declared that they have no known conflict of interest.

ACKNOWLEDGEMENT

The first author is supported by TUBITAK under project number 119C128. grants.

REFERENCES

[1] TEİAŞ, "Aylık Elektrik Üretim-Tüketim Raporları." Accessed: Sep. 26, 2023. [Online]. Available: https://www.teias.gov.tr/aylik-elektrik-uretim-tuketim-raporlari

[2] Enerji ve Tabii Kaynaklar Bakanlığı, "Elektrik - T.C. Enerji ve Tabii Kaynaklar Bakanlığı." Accessed: Sep. 26, 2023. [Online]. Available: https://enerji.gov.tr/bilgi-merkezi-enerji-elektrik

[3] Dışişleri Bakanlığı, "Paris Anlaşması / T.C. Dışişleri Bakanlığı." Accessed: Sep. 26, 2023. [Online]. Available: https://www.mfa.gov.tr/paris-anlasmasi.tr.mfa

[4] PVMagazine, "EU raises renewables target to 45% by 2030," PVMagazine. Accessed: Sep. 26, 2023. [Online]. Available: https://www.pv-magazine.com/2023/06/20/eu-raises-renewables-target-to-45-by-2030/?utm_source=dlvr.it&utm_medium=linkedin

[5] Z. Wang, "Electronic and Electrical Engineering . A grid-tied large-scale battery energy storage system : modelling from the pack level to the cell level," no. May, 2022.

[6] A. Nieto, V. Vita, and T. I. Maris, "Power Quality Improvement in Power Grids with the Integration of Energy Storage Systems," Int. J. Eng. Res. Technol., vol. 5, no. 7, Jul. 2016, doi: 10.17577/IJERTV5IS070361.

[7] I. Chernyakhovskiy, M. Joshi, D. Palchak, and A. Rose, "Energy Storage in South Asia: Understanding the Role of Grid-Connected Energy Storage in South Asia's Power Sector Transformation," NREL/TP--5C00-79915, 1811299, MainId:39133, Jul. 2021. doi: 10.2172/1811299.

[8] T. Chen et al., "Applications of Lithium-Ion Batteries in Grid-Scale Energy Storage Systems," Trans. Tianjin Univ., vol. 26, no. 3, pp. 208–217, Jun. 2020, doi: 10.1007/s12209-020-00236-w.

[9] A. Castillo and D. F. Gayme, "Grid-scale energy storage applications in renewable energy integration: A survey," Energy Convers. Manag., vol. 87, pp. 885–894, Nov. 2014, doi: 10.1016/j.enconman.2014.07.063.

[10] M. Haji Bashi, L. De Tommasi, and P. Lyons, "Electricity market integration of utility-scale battery energy storage units in Ireland, the status and future regulatory frameworks," J. Energy Storage, vol. 55, p. 105442, Nov. 2022, doi: 10.1016/j.est.2022.105442.

[11] O. H. Anuta, P. Taylor, D. Jones, T. McEntee, and N. Wade, "An international review of the implications of regulatory and electricity market structures on the emergence of grid scale electricity storage," Renew. Sustain. Energy Rev., vol. 38, pp. 489–508, Oct. 2014, doi: 10.1016/j.rser.2014.06.006.

[12] J. Ding, Y. Xu, H. Chen, W. Sun, S. Hu, and S. Sun, "Value and economic estimation model for grid-scale energy storage in monopoly power markets," Appl. Energy, vol. 240, pp. 986–1002, Apr. 2019, doi: 10.1016/j.apenergy.2019.02.063.

[13] M. M. Rana et al., "Applications of energy storage systems in power grids with and without renewable energy integration — A comprehensive review," J. Energy Storage, vol. 68, no. May, p. 107811, 2023, doi: 10.1016/j.est.2023.107811.

[14] A. Özan, "Batarya Enerji Depolama Sistemlerinin Elektrik Dağıtım Sistemine Etkisi ve Sezgisel Algoritmalar ile Faz Dengesizliğinin Giderilmesi," 2020.

[15] C. D. Parker, "Lead–acid battery energy-storage systems for electricity supply networks," J. Power Sources, vol. 100, no. 1–2, pp. 18–28, Nov. 2001, doi: 10.1016/S0378-7753(01)00880-1.

[16] D. Akinyele, J. Belikov, and Y. Levron, "Battery storage technologies for electrical applications: Impact in stand-alone photovoltaic systems," Energies, vol. 10, no. 11, pp. 1–39, 2017, doi: 10.3390/en10111760.

[17] M. S. Guney and Y. Tepe, "Classification and assessment of energy storage systems," Renew. Sustain. Energy Rev., vol. 75, pp. 1187–1197, Aug. 2017, doi: 10.1016/j.rser.2016.11.102.

[18] N. K. C. Nair and N. Garimella, "Battery energy storage systems: Assessment for small-scale renewable energy integration," Energy Build., vol. 42, no. 11, pp. 2124–2130, 2010, doi: 10.1016/j.enbuild.2010.07.002.

[19] V. G. Lacerda, A. B. Mageste, I. J. B. Santos, L. H. M. da Silva, and M. do C. H. da Silva, "Separation of Cd and Ni from Ni–Cd batteries by an environmentally safe methodology employing aqueous two-phase systems," J. Power Sources, vol. 193, no. 2, pp. 908–913, Sep. 2009, doi: 10.1016/J.JPOWSOUR.2009.05.004.

[20] D. Connolly, H. Lund, B. V. Mathiesen, and M. Leahy, "The first step towards a 100% renewable energy-system for Ireland," Appl. Energy, vol. 88, no. 2, pp. 502–507, Feb. 2011, doi: 10.1016/J.APENERGY.2010.03.006.

[21] A. B. Gallo, J. R. Simões-Moreira, H. K. M. Costa, M. M. Santos, and E. Moutinho dos Santos, "Energy storage in the energy transition context: A technology review," Renew. Sustain. Energy Rev., vol. 65, pp. 800–822, Nov. 2016, doi: 10.1016/J.RSER.2016.07.028.

[22] M. C. Argyrou, P. Christodoulides, and S. A. Kalogirou, "Energy storage for electricity generation and related processes: Technologies appraisal and grid scale applications," Renew. Sustain. Energy Rev., vol. 94, no. May, pp. 804–821, 2018, doi: 10.1016/j.rser.2018.06.044.

[23] N. Kawakami et al., "Development and field experiences of stabilization system using 34MW NAS batteries for a 51MW wind farm," in 2010 IEEE International Symposium on Industrial Electronics, 2010, pp. 2371–2376. doi: 10.1109/ISIE.2010.5637487.

[24] Y. Yuan, X. Zhang, P. Ju, K. Qian, and Z. Fu, "Applications of battery energy storage system for wind power dispatchability purpose," Electr. Power Syst. Res., vol. 93, pp. 54–60, Dec. 2012, doi: 10.1016/J.EPSR.2012.07.008.

[25] B. Diouf and R. Pode, "Potential of lithium-ion batteries in renewable energy," Renew. Energy, vol. 76, pp. 375–380, Apr. 2015, doi: 10.1016/J.RENENE.2014.11.058.

[26] L. Lu, X. Han, J. Li, J. Hua, and M. Ouyang, "A review on the key issues for lithium-ion battery management in electric vehicles," J. Power Sources, vol. 226, pp. 272–288, Mar. 2013, doi: 10.1016/J.JPOWSOUR.2012.10.060.

[27] D. Choi et al., "Li-ion battery technology for grid application," J. Power Sources, vol. 511, no. September, p. 230419, 2021, doi: 10.1016/j.jpowsour.2021.230419.

[28] M. C. Argyrou, P. Christodoulides, and S. A. Kalogirou, "Energy storage for electricity generation and related processes: Technologies appraisal and grid scale applications," Renew. Sustain. Energy Rev., vol. 94, pp. 804–821, Oct. 2018, doi: 10.1016/J.RSER.2018.06.044.

[29] S. Koohi-Kamali, V. V. Tyagi, N. A. Rahim, N. L. Panwar, and H. Mokhlis, "Emergence of energy storage technologies as the solution for reliable operation of smart power systems: A review," Renew. Sustain. Energy Rev., vol. 25, pp. 135–165, Sep. 2013, doi: 10.1016/J.RSER.2013.03.056.

[30] W. Wang, Q. Luo, B. Li, X. Wei, L. Li, and Z. Yang, "Recent Progress in Redox Flow Battery Research and Development," Adv. Funct. Mater., vol. 23, no. 8, pp. 970–986, 2013, doi: https://doi.org/10.1002/adfm.201200694.

[31] M. C. Argyrou, P. Christodoulides, and S. A. Kalogirou, "Energy storage for electricity generation and related processes: Technologies appraisal and grid scale applications," Renew. Sustain. Energy Rev., vol. 94, pp. 804–821, Oct. 2018, doi: 10.1016/J.RSER.2018.06.044.

[32] H. Chen, T. N. Cong, W. Yang, C. Tan, Y. Li, and Y. Ding, "Progress in electrical energy storage system: A critical review," Prog. Nat. Sci., vol. 19, no. 3, pp. 291–312, Mar. 2009, doi: 10.1016/J.PNSC.2008.07.014.

[33] F. Díaz-González, A. Sumper, O. Gomis-Bellmunt, and R. Villafáfila-Robles, "A review of energy storage technologies for wind power applications," Renew. Sustain. Energy Rev., vol. 16, no. 4, pp. 2154–2171, May 2012, doi: 10.1016/J.RSER.2012.01.029.

[34] K. K. Zame, C. A. Brehm, A. T. Nitica, C. L. Richard, and G. D. Schweitzer, "Smart grid and energy storage: Policy recommendations," Renew. Sustain. Energy Rev., vol. 82, pp. 1646–1654, Feb. 2018, doi: 10.1016/J.RSER.2017.07.011.

[35] G. Rancilio et al., "Modeling a Large-Scale Battery Energy Storage System for Power Grid Application Analysis," Energ. 2019 Vol 12 Page 3312, vol. 12, no. 17, p. 3312, Aug. 2019, doi: 10.3390/EN12173312.

[36] IRENA, "Electricity Storage Valuation Framework 2020," 2020.

[37] M. Bragard, N. Soltau, S. Thomas, and R. W. De Doncker, "The balance of renewable sources and user demands in grids: Power electronics for modular battery energy storage systems," IEEE Trans. Power Electron., vol. 25, no. 12, pp. 3049–3056, 2010, doi: 10.1109/TPEL.2010.2085455.

[38] L. Deguenon, D. Yamegueu, S. Moussa kadri, and A. Gomna, "Overcoming the challenges of integrating variable renewable energy to the grid: A comprehensive review of electrochemical battery storage systems," J. Power Sources, vol. 580, no. May, p. 233343, 2023, doi: 10.1016/j.jpowsour.2023.233343.

[39] G. G. Farivar et al., "Grid-Connected Energy Storage Systems: State-of-the-Art and Emerging Technologies," Proc. IEEE, vol. 111, no. 4, pp. 397–420, 2023, doi: 10.1109/JPROC.2022.3183289.

[40] A. Poullikkas, "A comparative overview of large-scale battery systems for electricity storage," Renew. Sustain. Energy Rev., vol. 27, pp. 778–788, 2013, doi: 10.1016/j.rser.2013.07.017.

[41] K. M. Tan, T. S. Babu, V. K. Ramachandaramurthy, P. Kasinathan, S. G. Solanki, and S. K. Raveendran, "Empowering smart grid: A comprehensive review of energy storage technology and application with renewable energy integration," J. Energy Storage, vol. 39, no. February, p. 102591, 2021, doi: 10.1016/j.est.2021.102591.

[42] A. Oudalov, R. Cherkaoui, and A. Beguin, "Sizing and optimal operation of battery energy storage system for peak shaving application," 2007 IEEE Lausanne POWERTECH Proc., pp. 621–625, 2007, doi: 10.1109/PCT.2007.4538388.

[43] Z. Yang, "Electrochemical energy storage for green grid: Status and Challenges," Chem. Rev., vol. 111, no. 5, pp. 3577–3613, 2011, doi: 10.1021/cr100290v.

[44] A. Pokhriyal, J. L. Domínguez-García, and P. Gómez-Romero, "Impact of Battery Energy System Integration in Frequency Control of an Electrical Grid with Wind Power," Clean Technol. 2022 Vol 4 Pages 972-986, vol. 4, no. 4, pp. 972–986, Oct. 2022, doi: 10.3390/CLEANTECHNOL4040060.

[45] A. Mohd, E. Ortjohann, A. Schmelter, N. Hamsic, and D. Morton, "Challenges in integrating distributed energy storage systems into future smart grid," IEEE Int. Symp. Ind. Electron., pp. 1627–1632, 2008, doi: 10.1109/ISIE.2008.4676896.

[46] Z. Šimić, G. Knežević, D. Topić, and D. Pelin, "Battery energy storage technologies overview," Int. J. Electr. Comput. Eng. Syst., vol. 12, no. 1, pp. 53–65, 2021, doi: 10.32985/IJECES.12.1.6.
[47] T. Chen et al., "Applications of Lithium-Ion Batteries in Grid-Scale Energy Storage Systems," Trans. Tianjin Univ., vol. 26, no. 3, pp. 208–217, 2020, doi: 10.1007/s12209-020-00236-w.
[48] K. Mongird et al., "Energy Storage Technology and Cost Characterization Report 2019," Report, no. July, pp. 1–120, 2019.
[49] H. Saboori, M. Mohammadi, and R. Taghe, "Virtual Power Plant (VPP), Definition, Concept, Components and Types," in 2011 Asia-Pacific Power and Energy Engineering Conference, Wuhan, China: IEEE, Mar. 2011, pp. 1–4. doi: 10.1109/APPEEC.2011.5749026.
[50] M. Cheng, S. S. Sami, and J. Wu, "Benefits of using virtual energy storage system for power system frequency response," Appl. Energy, vol. 194, pp. 376–385, May 2017, doi: 10.1016/j.apenergy.2016.06.113.